Title of Kinetic and Spectroscopic Characterization of Acetyl-CoA Synthase, a Key Enzyme in Anaerobic Carbon Fixation

by

Claire Griffith

A dissertation submitted in partial fulfillment
of the requirements for the degree of
Doctor of Philosophy
(Biological Chemistry)
in the University of Michigan
2025

Doctoral Committee:

Professor Stephen W. Ragsdale, Chair
Professor Nicolai Lehnert
Professor Bruce Palfey
Professor Janet Smith

Claire L. Griffith

clairelg@umich.edu

ORCID iD: 0000-0003-2627-0810

© Claire L. Griffith 2025

Acknowledgements

The past six years have had an immeasurable impact on my life and future and I would like to acknowledge and thank all those who made this adventure possible. First, I'd like to thank my whole family and especially my parents, Tauna and Paul, and my brother Benjamin, for their constant support and encouragement throughout my entire life and especially through last several years as I pursued my degree. I could not have done it without you. I want to acknowledge my committee, Janet Smith, Bruce Palfey, Nicolai Lehnert and former member Kevin Kubarych for their time, feedback, and comments that helped focus and strengthen my project. Thank you to the members of my lab, both past and present for their wonderful conversation, encouragement, feedback, and support: Dr. Seth Wiley, Dr. Angela Fleishhacker, Dr. Anjali Patwardhan, Dr. Chris Ohmer, Dr. Anindita Sarkar, Dr. Liu, Dan Esckilsen, Dr. Kaiyuan Zheng, Dr. Ingrid Kilde, Dr. Reyaz Gonzalez, Dr. Johnny Mendoza, Kareem Aboulhosn, Kiera Pendil, Juan Blume La Torre, Sobhan Zahiri Nogoorani, Rosie Dougherty, and Mary Lang.

I want to thank Dr. Steve Ragsdale, my PI and mentor, for taking me on during a pandemic and giving me a home in his lab, for his encouragement and support through this difficult project, and for his mentorship helping me develop my skills as a scientist.

As science is by its nature highly collaborative, I'd also like to acknowledge and thank my many wonderful collaborators for their deep insight and expertise that significantly informed this work. I thank my off-campus collaborators Dr. Ritimukta Sarangi, Dr. Macon Abernathy, Dr. Kewei Zhao at Stanford Synchrotron Radiation Lightsource (SSRL) of the Stanford Linear Accelerator Center (SLAC) National Accelerator Laboratory (Menlo Park, CA) who ran and analyzed my many XAS samples, Dr. Jin Xiong and Prof. Yisong "Alex" Guo at Carnegie Mellon University (Pittsburgh, PA) who worked on the Mössbauer spectroscopy, Simone Raugei and Bojana Ginovska at Pacific Northwest National Laboratory (Richland, WA) who worked on computational modeling, and Alexander Mueller, Dr. Steve Brown, and Dr. Michael Köpke at Lanzatech (Skokie, IL) who worked on the *C. autoethanogenum* experiments. I also thank Violet Wang and Anthony Goering with whom I worked during my internship at Lanzatech who made

it such a wonderful experience. In addition I want to thank and acknowledge Rob McCarrick who runs the EPR facility at Miami of Ohio University for making time for me to run EPR this last year while ours was down.

I also want to express my gratitude to the Biological Chemistry department as a whole and especially Beth Goodwin and Anne Vojtek for all they do to help us students through this process. And last but not least, I want to thank my PIBS cohort and the biological chemistry cohort of 2019 and especially Cassandra Dutcher and Cara Loomis for their friendship and support as we shared this adventure.

Table of Contents

Acknowledgements ii

List of Tables viii

List of Figures ii

List of Abbreviations viii

Abstract xi

Chapter 1 Introduction to Acetyl CoA Synthase and the Wood-Ljungdahl Pathway 1

1.1 The Wood-Ljungdahl Pathway 1

1.2 Structure of CODH/ACS 3

1.3 Paramagnetic vs Diamagnetic Mechanism 6

1.4 References for Chapter 1 9

Chapter 2 An Alcove at the Acetyl-CoA Synthase Nickel Active Site is Required for Productive Substrate CO Binding and Anaerobic Carbon Fixation 16

2.1 Abstract 16

2.2 Introduction 16

2.3 Results 20

2.3.1 An intact alcove is required for productive carbonylation of ACS 20

2.3.2 An intact alcove is required for autotrophic growth by the WLP 26

2.3.3 The alcove is not required for methylation of ACS 27

2.4 Discussion 28

2.5 Experimental procedures 33

2.5.1 Generation of monofunctional ACS alcove variants 33

2.5.2 Growth of C. autoethanogenum 33

2.5.3 Genetic modification of C. autoethanogenum 34

2.5.4 Expression and purification of monofunctional ACS variants in competent E. coli cells 34

2.5.5 EPR analysis of natural abundance and isotopically labeled ACS-CO variants 35

2.5.6 CO titration of ACS WT and variants monitored by EPR 36

2.5.7 XAS measurements 38

2.5.8 FTIR sample preparation 40

2.5.9 Methylation of WT and variant ACS 40

2.5.10 Preparation of MeCbi and TI(III) citrate reductant 41

2.6 Attributions 42

2.7 Author Contributions 42

2.8 Acknowledgements 42

2.10 References for Chapter 2 43

Chapter 3 Characterization of the Methyl- and Acetyl-Ni Intermediates in Acetyl CoA Synthase Formed During Anaerobic CO2 and CO fixation 49

3.1 Abstract 49

3.2 Introduction 49

3.3 Results 52

3.3.1 The Methylated Intermediate 52

3.3.2 The Acetyl Intermediate 62

3.4 Discussion 64

3.4.1 A Delocalized [4Fe-4S]-Ni_p-Ni_d Active Site 64

3.4.2 Role of Second-Sphere Ligands 66

3.4.3 Comparison to the Ni-Azurin Model 67

3.4.4 The EC mechanism 68

3.5 Conclusions 70
3.6 Materials and Methods 71
3.7 Author contributions 72
3.8 Attributions 72
3.9 References for Chapter 3 73
Chapter 4 Characterization of the Post-Thiolysis State of the A-cluster of Acetyl CoA Synthase 81
4.1 Abstract 81
4.2 Introduction 81
4.3 Materials and Methods 83
4.3.1 Use of anaerobic techniques in ACS characterization 83
4.3.2 Metal Free Work 84
4.3.3 Media and Antibiotics 84
4.3.4 10L expression of wild type acsB with pRKISC 84
4.3.5 Methyl cobinamide synthesis 85
4.3.6 Methyl and Acetyl ACS 85
4.3.7 Single turnover acetyl-CoA samples 86
4.3.8 Acetyl-CoA coupled colorimetric assay 86
4.3.9 Methyl viologen titrations 86
4.3.10 XAS 87
4.3.11 Mössbauer 88
4.3.12 EPR 88
4.4 Results 89
4.4.1 Acetyl-ACS stability 89
4.4.2 Methyl viologen titrations 89
4.4.3 Ni XAS Results 92

4.4.4 Fe XAS Results 95
4.4.5 Mössbauer of A*, A_{ox} and A_{ac} 97
4.4.6 EPR 99
4.5 Discussion 100
4.6 Conclusion 102
4.7 Author Contributions 102
4.8 References for Chapter 4 103
Chapter 5 Conclusions 109
5.1 References 112

List of Tables

Table 2-1 Monitoring methylation activity of ACS variants by single-turnover stopped-flow kinetics 20

Table 4-1 Summary of MV titrations from prep 1. The initial concentration of A* is calculated based on the amount of active protein (i.e. protein capable of single turnover Ac-CoA synthesis). Initial and final concentrations of MV_{red} were determined based on absorbance at 600nm (after correction for dilution and protein concentration). The initial and final MV_{ox} concentrations are determined from $MV_{red} + MV_{ox} = 100\mu M$. The final A* was calculated as A* initial minus half of the change in MV_{red}. K_{eq} was calculated from the ratio of final concentrations, $K_{eq} = (A_{ox}/A^*) \times (MV_{red}/MV_{ox})^2$. The apparent reduction potential $E_{A^*/Aox}$ was calculated by inserting the K_{eq} into the Nernst equation and using the standard reduction potential for MV of -450mV[30]. 92

Table 4-2 Ni EXAFS fitting parameters. The estimated standard deviations for the distances are in order of ± 0.02 Å. 95

Table 4-3 Fe EXAFS fitting parameters. The estimated standard deviations for the distances are in order of ± 0.02 Å. 96

Table 4-4 Estimates of the iron-sulfur cluster charge obtained from peak deconvolution of the pre-edge feature, calibrated against the Grunwald et al. biomimetic cubane series[30]. 96

Table 4-5 Pseudo-Voigt peak deconvolution parameters for the Fe K-pre-edge features. 97

List of Figures

Figure 1-1. The WLP reduces two CO_2 molecules, one to a methyl on the corrinoid iron sulfur protein (CFeSP) and the other to CO by CODH. Both the methyl and CO are passed to ACS which condenses them and CoA thiolyzes the acetyl group to make acetyl-CoA. This autotrophic pathway is couples to heterotrophic metabolism. Figure is adapted from Figure 2 in Ragsdale, Comprehensive Coordination Chemistry, 2021[18] 2

Figure 1-2 High pressure xenon structure of CODH/ACS from Moorella thermoacetica, PDB 1OAO. The green rectangle in the lower left highlights the structure of the C-cluster with a 1Ni3Fe4S cluster with a pendant Fe. The blue rectangle in the upper right highlights the structure of the A-cluster with its 4Fe4S cluster and two nickels bridged by cysteines. The proximal nickel (Ni_p) is in green and is the location of substrate binding. In the center is the structure of the CODH/ACS complex with a CODH dimer (green) in the center and one ACS (blue) bound to the dimer interface on either side. The C-cluster is the site of CO_2 reduction to CO, which then travels through the 70Å tunnel marked by the red spheres (xenon) to the A-cluster where CO, methyl, and CoA combine to form acetyl-CoA. Figure is adapted from Doukov, et. al *Biochemistry* (2008) [17] Ragsdale S., *Ann N Y Acad Sci.* (2008)[5], Ragsdale and Pierce, *BBA* (2008)[15]. 3

Figure 1-3 Close view of secondary sphere ligands surrounding the A-cluster. a) Viewer is in the CO tunnel looking toward the proximal nickel which is substituted with zinc (grey) in this structure. The A-cluster is inaccessible to solvent ("closed") and the CO tunnel is open allowing CO to bind. b) As the conformation of ACS becomes more open and solvent accessible, the secondary sphere residues rearrange with F229 swinging in to block off the CO tunnel..... 4

Figure 1-4 Domain Motions of CODH/ACS Crystal structures are shown in cartoon representation with transparent van der Waals (VDW) surfaces. Flexible fitting models are shown in cartoon representation with corresponding EM maps. These low resolution structures highlight the extreme movement of the ACS subunit. The A-cluster is circlesd in red and black arrows show direction of movement as the enzyme opens. Figure adapted from Figure 4. From Cohen et. al, 2020[33]..... 5

Figure 1-5 Proposed paramagnetic mechanism of ACS with previously characterized intermediates highlighted with blue boxes[23,28,40]. Modified from Fig 6 of Ragsdale, S.W. Comprehensive Coordination Chemistry III, Volume 8[18] 6

Figure 1-6 Proposed diamagnetic mechanism of ACS with previously characterized intermediates highlighted with blue boxes[28]. Modified from Fig 6 of Ragsdale, S.W. Comprehensive Coordination Chemistry III, Volume 8[18] 7

Figure 2-1 **An alcove in the Wood-Ljungdahl pathway (WLP) of anaerobic CO_2 fixation.** *A*, focus on CODH, ACS, and the organometallic nature of the pathway. One CO_2 enters the WLP at the Eastern (Methyl) branch (*red*), where it undergoes 2-electron reduction to formate by FDH), followed by 4-electron reduction to a methyl group methyltetrahydrofolate (CH_3-THF), and transferred to the B_{12} center of the CFeSP (Co-CH_3). In the Western (carbonyl) branch (*blue*), the other CO_2 undergoes enzymatic 2-electron reduction by CODH to CO, which migrates to the Ni_p site in the A-cluster of ACS through a tunnel, which is tightly interfaced to the A-cluster. The A-cluster reacts with CH_3-[Co] to generate CH_3-Ni, binds CO, and undergoes C-C bond formation to form acetyl-Ni, and then reacts with CoA to generate acetyl-CoA, which serves as a metabolic building block for all carbon-containing molecules in the organism and as a source of ATP, through the enzymatic reactions of phosphotransacetylase and acetate kinase. *B*, catalytic mechanism of ACS and introduction of the alcove in the WLP. The Ni_p site of the A-cluster of ACS react first with either CO or methyl-Co, generated as described above, then the other substrate, and finally with CoA. The A-cluster and the residues of the Alcove are depicted in the inset. See the text for further details. ACS, acetyl-CoA synthase; CODH, carbon monoxide dehydrogenase; CFeSP, the corrinoid iron-sulfur protein; FDH, formate dehydrogenase; WLP, Wood-Ljungdahl pathway..... 18

Figure 2-2 **Crystal structure of Xe-bound CODH-ACS, with focus on the alcove in ACS.** Crystal structure of (*A*) the CODH/ACS complex obtained under high-pressures of Xenon (*teal spheres*) to reveal the gas channel and show the 7 clusters in CODH (B–D) and ACS (A) involved in electron transfer and catalysis (C and A). *B*, expanded view of the A-cluster of ACS, highlighting the CO tunnel spanning from the CODH C-cluster (not shown) to the ACS A-cluster, with nearby residues as *spheres*. The residues that form the Alcove (Fig. 1*B*) are shown surrounding one of the Xe atoms. *C*, side-on perspective of the A-cluster, showing the alcove's role in maintaining CO near Ni_p, with F229 shown in *magenta*. (*left*) Down-tunnel perspective, 90˚ CW toward viewer (relative to (*right*)), showing how F229 and nearby residues form an opening for CO to reach the A-cluster. Stereoscopic versions of these images are found in the supplemental materials (Figs. S4 and S5). PDB 2Z8Y. ACS, acetyl-CoA synthase; CODH, carbon monoxide dehydrogenase; CW, clockwise; PDB, Protein Data Bank. 19

Figure 2-3 **FTIR and EPR spectra of ACS variants.** *A*, FTIR: highlight of the characteristic Ni-CO IR stretch at 1995 cm^{-1} between the region 1970 to 2020 cm^{-1}. The Ni-CO stretch is noticeably absent in F229A, while the WT and F229W have strong Ni-CO signals. The integrated area of the F229W Ni-CO peak is 83% of the WT area. The protein concentrations were as follows: WT, 580 ± 12 μM; F229W, 590 ± 26 μM, and F229A, 580 ± 16 μM. *B*, the full spectra of the ACS variants showing global folding similarity. Bands belonging to ACS include the various amide bands over the 1250 to 1750 cm^{-1}, the C-H bonds from 2800 to 3000 cm^{-1}, and the N-H and O-H stretches from 3200 to 3750 cm^{-1}. The region between 2200 to 2750 cm^{-1} was omitted due to strong D_2O signals obscuring the spectra. *C*, EPR spectra of the ACS variants exposed to naturally abundant ^{12}CO (—) compared with isotopically labeled ^{13}CO (---). Quantified spin percentages are listed on the right as NA%/^{13}CO%. The ^{13}C splitting is most prominent at $g = 2.028$. Less intense broadening can be seen at 2.08 for WT and F229W, and at 2.062, 2.057, and 2.024 for the F229A variant. The protein concentrations for the EPR were 236 μM (WT), 280 μM (F229A), 276 μM (F229W) and the spin

concentrations are shown. ACS, acetyl-CoA synthase; EPR, electron paramagnetic resonance; IR, infrared; NA, natural abundance..... 21

Figure 2-4 Comparison of the CO binding affinity of the alcove variants. *A*, direct CO titration showing individual data points at varying CO concentrations for the ACS variants fit to a quadratic tight-binding equation (see Experimental procedures). EPR samples of ACS were exposed to increased concentration of CO (concentration measured by binding at 424 nm to equine Mb), frozen in liquid N_2, and placed in an EPR cryostat maintained at 100 K for EPR spectroscopy. The spectrum was doubly integrated and spin quantified by comparison to a Cu(II) perchlorate standard. The measured K_D values (and the 95% confidence intervals) were 12.8 μM (7.3–20.2 μM, 95% CI), 0.16 μM (<1 pM-8 μM, 95% CI), and 340 μM (140–940 μM at 95% CI), respectively, for WT, F229W, and F229A. *B* and *C*, anaerobic equilibrium CO competition experiment between F229W and dithionite-reduced (Fe^{2+}) equine myoglobin (Mb). In (*B*), UV-visible spectra of triplicate Mb-CO control samples were determined from a solution of 4 μM Fe^{2+}-Mb reacted with 4.0 μM CO in 50 mM Tris–HCl, pH 7.6 in a 1 cm cuvette at 25 °C. For the quintuplicate competition experiments, 4.0 μM CO was added to 4 μM active F229W, sealed with a rubber septum, equilibrated for 5 min, and an initial spectrum was recorded. Then, 4 μM Fe^{2+}-Mb was added, incubated for 30 min, and the equilibrium spectrum was recorded. The difference spectra (Fe^{2+}-Mb-CO minus Fe^{2+}-Mb) are shown. Based on the five UV-visible experiments, the K_D(CO) for F229W was 160 ± 30 nM (95% confidence interval, CI). In (*C*), triplicate EPR experiments were performed in which 200 μl samples were transferred from the UV-visible cuvette to a quartz capillary, quickly frozen in liquid N2, and EPR spectra were run to determine the amount of F229W-CO. Based on the EPR measurements, the average K_D value was 160 ± 90 nM (95% CI). Thus, the three K_D(CO) measurements (from the direct CO binding and CO competition experiments) reveal a K_D(CO) for the F229W-CO complex between 150 to 190 nM at a 95% confidence level. ACS, acetyl-CoA synthase; CI, confidence interval; EPR, electron paramagnetic resonance..... 23

Figure 2-5 **Ni K-edge XAS data showing pre-edge changes on the left and related EXAFS on the right.** *Insets* show shifts in the pre-edge for CO-exposed (*red*) ACS relative to unexposed (*blue*), where the first derivative shows distinct shifts for one of the two A-cluster Ni. Ni K-edge data for F229A does not show a change seen in the WT and F229W. Consistent with these pre-edge data are the EXAFS, which show little to no changes for CO-exposed F229A relative to unexposed. WT data adapted with permission from ref (11). Copyright 2017 American Chemical Society. ACS, Acetyl-CoA synthase; EXAFS, extended X-ray absorption fine structure; XAS, X-ray absorption spectroscopy. 25

Figure 2-6 **(*Top*) Alignment of AcsB showing highly conserved region around AA position 229 in Moorella thermoacetica and corresponding position 209 in Clostridium *autoethanogenum* (*bottom*) Complementation of *C. autoethanogenum* *ΔacsB*.** Only wild-type *acsB* but not *acsB*(F209A) is able to restore growth under $CO/H_2/CO_2$ autotrophic conditions. ACS, Acetyl-CoA synthase; AcsB, bacterial ACS. 27

Figure 2-7 **Transient kinetics of methylation of ACS with MeCbi.** Stopped-flow traces of 10 μM ACS reduced with 3x Ti(III) citrate and methylated with 10 μM MeCbi measured by monitoring the time-dependent decrease in absorbance at 470 nm of MeCbi and the increase at

390 nm of Co(I)-Cbi. Data were fit with the equation for a stretched exponential. ACS, acetyl-CoA synthase; MeCbi, methyl-Cbi; Ti(III) citrate, titanium(III) citrate. 28

Figure 2-8 **Alcove requirement for ACS catalysis.** (*Top*), the alcove integrated on one side with Ni_p and the A-cluster metallocofactor as the ACS active site and on the other with the tunnel, serving as an extension of the active site. The alcove significantly lowers the K_s for CO. The directing actions of the tunnel combined with the concentrating and protective effects of the alcove near Ni_p, prevents CO loss and inhibition, ensuring ACS can randomly bind either substrate (CO or methyl) at the low CO concentrations required for autotrophic growth. See the text for details. (*Bottom*), conserved sequences containing the five alcove residues. A blast search and multiple sequence alignments were performed of 5000 prokaryotic genomes (excluding archaea) against the *Moorella thermoacetica* ACS (AcsB) sequence (mta_Moth_1202, (55). Sixty amino acids were then loaded into the Weblogo program (56) to visualize the 27 to 28 amino acids with the highest conservation in each of the three Alcove sequence motifs. ACS, acetyl-CoA synthase; AcsB, bacterial ACS..... 30

Figure 3-1 Simplified scheme of the ACS intermediates involved in the WLP highlighting the nickel–carbon bonds formed in the catalytic cycle..... 50

Figure 3-2 Proposed ACS mechanism including electrochemical coupling (EC mechanism). (a) WLP catalytical cycle with proposed intermediates and formal oxidation states in ACS. The WLP includes two branches, which converge at the ACS A-cluster active site. Methyl branch (red): CO_2 undergoes reduction to a methyl group (methyl-tetrahydrofolate, methyl-H_4folate) shown in the dashed circles, which experiences stepwise transfer to cobalt in a B_{12} cofactor bound to the corrinoid iron–sulfur protein (CFeSP) and then to ACS. Carbonyl branch (blue): CODH catalyzes CO2 reduction to CO, which enters a 75 Å tunnel (12,13) to the ACS active site. The proximal Ni (Ni_p) in the A-cluster (1) randomly binds either CO or CH_3 to form Ni_p–CO (2, ANiFeC) or Nip–CH3 (4) (or vice versa). (5) C–C bond condensation generates acetyl-Nip (3, Nip–Ac), followed by CoA binding and thiolysis to form acetyl-CoA, which is then incorporated into biomass or converted to acetate and ATP. (b) The A cluster structure with oxidation states corresponding to its resting A_{Ox} state. (c) Calculated electrochemical potentials associated with the different states of the A-cluster, including the hypothesized diamagnetic Nip(0) state. (14) (d) The diamagnetic mechanism involving conversion of Ni_p("0") to Ni_p(II)–CH3 and Ni_p(II)–Ac as intermediates. The highlighted box includes the option of CO binding first, then methyl, consistent with pulse-chase experiments (see text for details). 51

Figure 3-3 Methylation of ACS observed by Co K-edge XAS. (a) Normalized Co K-edge XAS of methyl-cob(III)alamin (black lines) and cob(I)alamin (red lines) as reference compounds. (b) Co K-edge XAS of the reaction of methyl-cob(III)inamide with no ACS present (black lines) and cob(I)alamin (red lines) as reference compounds. (b) Co K-edge XAS of the reaction of methyl-cob(III)inamide with no ACS present (black lines) and with Ti(III) citrate-treated AOx to generate cob(I)inamide (red lines). The insets show the expanded pre-edge regions. 54

Figure 3-4 Structure of A_{Ox} and A_{Me} obtained from XAS and DFT. (a) Ni K-edge XAS and (b) Fe K-edge XAS showing changes to the near and rising edge regions upon methylation of A_{Ox} (blue lines) to A_{Me} (red lines). The insets show the expanded pre-edge region and corresponding TD-DFT calculations (dotted lines). (c) Ni K-edge EXAFS (inset) and (d) Fe K-

edge EXAFS (inset) with corresponding Fourier transforms. (e–g) Calculated structural parameters of the [4Fe–4S]–Ni_p(Me)–Ni_d active site of A_{Me} obtained from DFT. 55

Figure 3-5 Characterization of the AMe State of ACS. (a) Absorption-display, dispersion-detected Q-band CW-EPR (2 K) of AMe with the following isotopes: CD3-, 13CH3-, 13CD3-, 57Fe/13CH3. (b) 4.2 K Mössbauer spectra (black lines) and simulations (red lines) of Aox (top), AMe (middle) and AAc (bottom), with arrows indicating regions not included in the simulations. (c) 13C ENDOR spectra of ANiFeC (2) with two (13) COs covalently bound to the Nip(I) center in the A-cluster of ACS. (51) (d) ENDOR spectra of 13C- and 2H-labeled AMe to test whether the EPR spectrum of Figure 4A is from a Nip(III)–Me complex. The absence of a 13C signal from the presence of 13CH3 and of a 2H signal from the presence of CD3 shows that this EPR signal is not from a Nip(III)–Me complex. The 13C and 2H Larmor frequencies are shown on the spectra..... 57

Figure 3-6 Structure of A_{Ac} obtained from XAS and DFT in comparison to A_{Me}. (a) Ni K-edge XAS and (b) Fe K-edge XAS showing changes to the near and rising edge regions upon acetylation of A_{Me} (red lines) to A_{Ac} (blue lines). The insets show the expanded pre-edge region and corresponding TD-DFT calculations (dotted lines). (c) Ni K-edge EXAFS (inset) and (d) Fe K-edge EXAFS (inset) with corresponding Fourier-transforms. (e–g) Calculated structural parameters of the [4Fe–4S]–Ni_p(Ac)–Ni_d active sites of A_{Ac}..... 64

Figure 4-1 Stability of A_{ac} over time. Over the course of nine days, 24uL aliquots of acetyl-ACS were reacted with 6X CoA to forma acetyl-CoA. After 30 seconds, the reaction was quenched by precipitating the protein with 50mM potassium hydrogen phthalate and then freezing the samples for later analysis by a coupled colorimetric assay. Acetyl-ACS stocks are reasonably stable for 4-6 hours before degradation becomes measureable. Data was fit to a first order rate law. 89

Figure 4-2 Methyl viologen titrations varying order of addition of A_{ac} and CoA, and starting MV red/ox ratios. 90

Figure 4-3 Methyl viologen titrations starting with A_{ac} and CoA and varying the waiting time, 30s (MV12), 1min 20sec (MV13), and 5 minutes (MV14), before adding methyl viologen to probe stability of A* state. A* can still reduce methyl viologen after 5 minutes so it is sufficiently stable to make spectroscopy samples. 91

Figure 4-4 Feff-best fits to the Ni and Fe EXAFS. Best fits to the Fe EXAFS of Aox (a) and A" (b). Best fits to the Ni EXAFS of Aox (c) and A" (d), as well as A" with the Ni-S shell split (e). Fitting parameters are available in Table 4-2 and 4-3. 93

Figure 4-5 Ni and Fe K-edge XAS. a) Ni K-edge XAS of Aox and A" *inset*: magnification of the pre-edge region and its second derivative. b) Ni EXAFS showing changes in the first shell between Aox and A". c) Fe K-edge XAS of Aox and A" *inset*: magnification of the pre-edge region. d) Fe EXAFS of Aox and A" illustrating the substantial change in the Fe-Fe interaction. 93

Figure 4-6 Pseudo-Voigt peak deconvolution of the pre-edge features of the Fe XAS of Aox and A" (a-b), as well as the biomimetic cubane redox series from Grunwald et al. 2024 (c-g).

The [Fe4S4] Cubans in the +0 through +2 state were used to make a calibration curve of pre-edge amplitude vs cluster charge to estimate the charge difference between Aox and A" (h)..... 95

Figure 4-7 ^{57}Fe Mb spectra for A-ox, A-ac and A" under indicated conditions. Black bars represent experimental values (center positions) and associated uncertainties (bar lengths). Red lines represent overall simulations, colored dashed lines show individual components: Site I for A-ox in blue, Site II for A-ox in olive, Site I for A" in green, Site II for A" in orange, A_{red}-CO in grey. 98

Figure 4-8 EPR of A_{ox}+ CO + dithionite, A* + CO, A_{ox} + CO, and A*. CW EPR collection parameters were 10mW, 110K, 0.4G modulation amplitude, gain 10, frequency 9.189 GHz. a) A_{ox} + CO + dithionite and A* + CO both exhibit the characteristic NiFeC signal with 22%, and 23% spin respectively b) all spectra, zoom in of EPR spectra clearly show that A* exhibits no signal and A_{ox} + CO, no dithionite has a very small, <2% spin NiFeC signal due to slight contamination of reductant in the sample. 99

List of Abbreviations

- A* - reduced state of ACS after thiolysis of acetyl-CoA
- A-cluster – ACS metalloenzymatic active site
- Ac – acetyl
- Ac-ACS – acetyl-ACS
- ACS – acetyl-coenzyme A synthase
- Ala – alanine
- Amp – ampicillin
- Aox – oxidized A-cluster
- Ared – reduced A-cluster
- A.U. – arbitrary units
- C – carbon
- Cbi – cobinamide
- Cbl – cobalamin
- Co – cobalt
- CO – carbon monoxide
- CO_2 – carbon dioxide
- CODH – carbon monoxide dehydrogenase
- CODH/ACS – carbon monoxide dehydrogenase/acetyl-coenzyme A synthase tetrameric complex
- CoA – coenzyme A
- CFeSP – corrinoid iron-sulfur protein
- Cryo-EM – cryo-electron microscopy
- Cu – copper
- Cys – cysteine
- DTH – dithionite

- DTT – dithiothreitol
- e^- – single electron; one reducing equivalent
- E" – two electron reduced state of ACS after thiolysis of acetyl-CoA
- ENDOR – electron nuclear double resonance
- EPR – electron paramagnetic resonance
- EXAFS – extended X-ray absorption Fine Structure
- F229 – phenylalanine 229
- F229A – alanine substitution at F229
- F229W – tryptophan substitution at F229
- F512 – phenylalanine 512
- Fd-II – ferredoxin
- FDH – formate dehydrogenase
- Fe – iron
- $[Fe_4S_4]$ – four-iron, four-sulfur cluster
- FTIR – fourier transform infrared spectroscopy
- G – gauss
- G145 – glycine 145
- H_2 – hydrogen gas
- I146 – isoleucine 146
- ICP-OES – inductively coupled plasma optical emission spectroscopy
- ICP-MS – inductively coupled plasma mass spectrometry
- IR – infrared
- K – kelvin
- Kan - kanamycin
- kDa – kilodalton
- LUCA – last universal common ancestor
- LUMO – lowest unoccupied molecular orbital
- Me – methyl
- Me-ACS – methylated ACS
- MeCbi – methyl-cobinamide

- MeCbl – methyl-cobalamin
- Me-CFeSP – methylated corrinoid iron-sulfur protein
- MeI – methyl iodide
- MeTr – methyl transferase
- MS – mass spectrometry
- mV – millivolt
- mW – milliwatts
- NA – natural abundance
- Ni – nickel
- Ni-C – nickel-carbon bond
- Ni-CO – nickel-carbonyl
- Ni_d – distal nickel
- NiFeC – nickel-iron-carbonyl signal observed by EPR
- Ni_p – proximal nickel
- Phe – phenylalanine
- SDS-PAGE – sodium dodecyl sulfate polyacrylamide gel electrophoresis
- TEV – tobacco etch virus
- THF – tetrahydrofolate; H4-folate
- Ti – titanium
- Trp – tryptophan
- V – volt
- V149 – valine 149
- WLP – Wood-Ljundahl pathway
- WT – wildtype
- XANES – X-ray absorption near edge structure
- XAS – x-ray absorption spectroscopy
- Xe – xenon
- Zn – zinc

Abstract

The Wood-Ljungdahl pathway (WLP) of carbon fixation is an ancient anaerobic metabolic pathway, found in both archaea and bacteria that accomplishes the reversible conversion of CO_2 into bioavailable carbon. The key enzyme complex of this pathway is carbon monoxide dehydrogenase (CODH) and acetyl coenzyme-A synthase (ACS), two nickel containing iron sulfur cluster proteins that together catalyze the reversible reduction of CO_2 to acetyl CoA, an important and versatile metabolic intermediate. The Ni[Fe_3S_4] C-cluster of CODH reduces carbon dioxide to carbon monoxide which travels through a 70Å internal protein tunnel to the dinickel iron-sulfur cluster active site of ACS (A-cluster). The proximal nickel (Ni_p, closest to the iron sulfur cluster) changes redox state and binds substrates while the distal nickel (Ni_d) remains Ni^{2+} and plays a mainly structural role. ACS binds CO and a cobalamin-donated methyl randomly, condenses them to form an acetyl, then coenzyme A thiolyzes to make acetyl-CoA. The A-cluster is also surrounded by several hydrophobic residues, which have been observed to rearrange in crystal structures between an open and closed state forming an alcove. This dissertation was aimed at characterizing the role of the hydrophobic alcove near the A-cluster, as wells as nickel intermediates of its catalytic cycle. Chapter **2** of this dissertation describes characterization of two mutations to one of these alcove residues, F229A and F229W, and their profound impact on CO binding. Characterization methods include Fourier transform infrared spectroscopy (FTIR), x-ray absorption spectroscopy (XAS), Mössbauer, electron paramagnetic resonance (EPR) and titration and kinetic characterization of substrate binding. While the catalytically relevant intermediates of ACS have long been a subject of debate in the field, paramagnetic vs. diamagnetic, one aspect long proposed but unproved is that all of the substrates are nickel-bound. Chapter **3** describes the characterization of the methyl and acetyl intermediates by XAS directly demonstrating for the first time that these are nickel-organometallic intermediates and confirming this long-held hypothesis. The redox state of the proximal nickel and iron-sulfur cluster of the catalytically active intermediates continue to be debated. The CO bound state has clearly been shown by EPR and XAS to be a paramagnetic

$[Fe_4S_4]^{2+}$CO-N_p^{1+}. ACS must be reductively activated to enter its catalytic cycle and the paramagnetic mechanism proposes the other intermediates states (activated, methyl-, acetyl-) are paramagnetic Ni^{1+} or Ni^{3+} with an $[Fe_4S_4]^{2+}$ while the diamagnetic mechanism proposes these intermediates are Ni^{1+} $[Fe_4S_4]^{1+}$ (reductively activated) and $Ni^{2+}[Fe_4S_4]^{2+}$ for the methyl- and acetyl-bound states. Recent work by Gencic et. al. described a proposed two-electron reduced state of the A-cluster generated after the thiolysis of acetyl-CoA. Chapter **4** describes further spectroscopic characterization of this post-thiolysis intermediate by XAS, Mössbauer, and EPR and found that it is one electron reduced relative to the resting state of the enzyme. The studies described in this work highlights the importance of secondary sphere residues on CO-binding at the A-cluster, and spectroscopically characterizes the nickel-bound nature and redox state of these intermediates. These conclusions significantly improve our understanding of the alcove and intermediates of the A-cluster and provide critical insight into this ancient mechanism of anaerobic carbon fixation. Improved understanding of the complex bioinorganic chemistry of ACS provides key offers enticing applications in production of renewable carbon-based biofuels by improving the efficiency of the WLP.

Chapter 1 Introduction to Acetyl CoA Synthase and the Wood-Ljungdahl Pathway

One of the biggest global threats facing our population today is increasing concentrations of carbon dioxide (CO2) in the atmosphere. Rising CO2 levels can have indirect effects on human health including an increase in health-related deaths as the frequency and severity of heat-waves grows, poorer air quality, and ocean acidification which impacts food chains and sources[1,2]. We need to understand the mechanisms of carbon fixation before they can be applied to the development new methods to increase CO_2 uptake and produce environmentally friendly fuels and chemicals.

1.1 The Wood-Ljungdahl Pathway

There are seven known carbon fixation cycles, the most energy efficient of which is the reductive acetyl-CoA pathway, also known as the Wood Ljungdahl Pathway (WLP). Unlike other carbon fixation pathways, the WLP is capable of simultaneous carbon reduction and energy conservation, producing up to 1.5mol of ATP per mol of acetate produced making organisms using it strong candidates for biocatalysis and biofuel production [3,4]. This pathway is responsible for approximately 10% of worldwide acetate production annually[5]. The study of acetogenic metabolism is highly relevant to the environment and human health. Acetogens and anaerobes containing the WLP influence ongoing research to develop industrial catalysts for CO_2 reduction[6] as well as improvement and modification of acetogens to produce biofuels and other small carbon molecules of industrial use[7,8]. Acetogenic bacteria utilizing the Wood-Ljungdahl pathway are currently employed in the production of biofuels and other carbon-based products, efficiently converting carbon dioxide, carbon monoxide, and hydrogen to biomass while repurposing carbon emissions[9–11].

The WLP is an ancient pathway found only in strict anaerobes and played an important role in the evolutionary history of life. This pathway is traceable back to the last universal common ancestor (LUCA) and may even have been the first autotrophic process on Earth[12–14]. It

is unique among biochemical pathways due to its reliance on a series of nickel organometallic intermediates and its use of the highly toxic CO as an intermediate[15].

This pathway is made up of two branches, the methyl branch which in a stepwise manner reduces one CO_2 to methyl-B_{12} on the corrinoid iron sulfur protein (CFeSP), and carbonyl branch, in which carbon monoxide dehydrogenase (CODH) reduces CO_2 to CO **(Figure 1-1).** These branches meet at acetyl-CoA synthase (ACS), which forms a tight complex with CODH. The final step of carbon-fixation in M. thermoacetica is carried out by the bifunctional carbon monoxide dehydrogenase/acetyl-coenzyme A synthase (CODH/ACS) complex. CODH/ACS forms a 310 kDa α2β2 heterotetramer, with a CODH dimer in the center and one ACS tightly bound to the dimer interface on either end. CODH catalyzes the reversible reduction of CO_2 to CO. ACS catalyzes the formation of the acetyl-CoA by generating the carbon-carbon bond between CO and a methyl group, then transferring the acetyl to coenzyme-A (CoA) forming a carbon-sulfur bond[16]. The active sites of CODH (C-cluster) and ACS (A-cluster) are connected by an approximately 70 Å hydrophobic channel visualized by high pressure xenon x-ray crystallography[17] **(Figure 1-2)**.

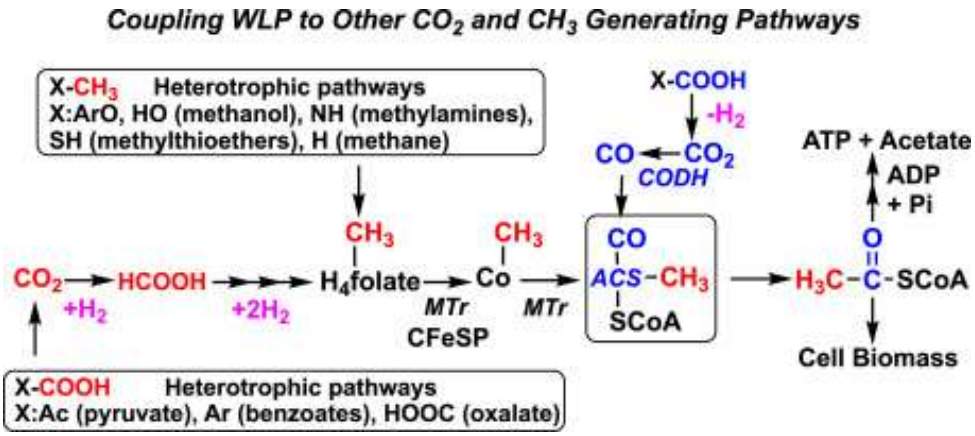

Figure 1-1. The WLP reduces two CO_2 molecules, one to a methyl on the corrinoid iron sulfur protein (CFeSP) and the other to CO by CODH. Both the methyl and CO are passed to ACS which condenses them and CoA thiolyzes the acetyl group to make acetyl-CoA. This autotrophic pathway is couples to heterotrophic metabolism. Figure is adapted from Figure 2 in Ragsdale, Comprehensive Coordination Chemistry, 2021[18]

1.2 Structure of CODH/ACS

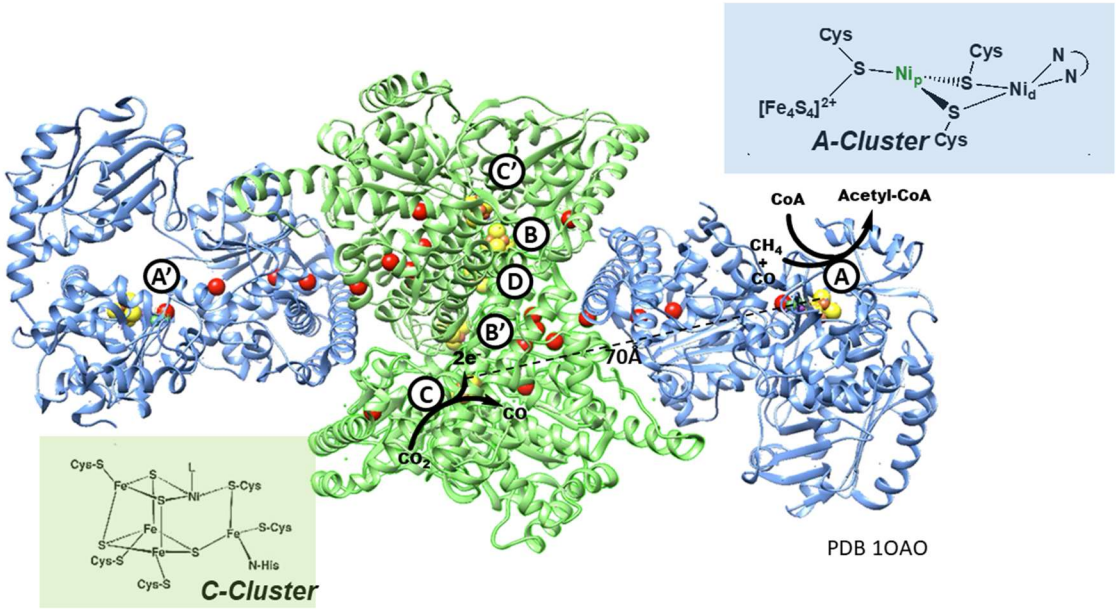

Figure 1-2 High pressure xenon structure of CODH/ACS from Moorella thermoacetica, PDB 1OAO. The green rectangle in the lower left highlights the structure of the C-cluster with a 1Ni3Fe4S cluster with a pendant Fe. The blue rectangle in the upper right highlights the structure of the A-cluster with its 4Fe4S cluster and two nickels bridged by cysteines. The proximal nickel (Ni_p) is in green and is the location of substrate binding. In the center is the structure of the CODH/ACS complex with a CODH dimer (green) in the center and one ACS (blue) bound to the dimer interface on either side. The C-cluster is the site of CO_2 reduction to CO, which then travels through the 70Å tunnel marked by the red spheres (xenon) to the A-cluster where CO, methyl, and CoA combine to form acetyl-CoA. Figure is adapted from Doukov, et. al *Biochemistry* (2008) [17] Ragsdale S., *Ann N Y Acad Sci.* (2008)[5], Ragsdale and Pierce, *BBA* (2008)[15].

The canonical organism for studying the CODH/ACS complex has long been *Moorella thermoacetica* (originally named *Clostridium thermoaceticum*), an organism first identified in 1942 by Fontaine and colleagues to produce acetate during glucose fermentation indicating a novel fermentative pathway[19,20]. Carbon-14 experiments by Barker and Kamen established its growth on glucose involved incorporation of two carbon dioxide molecules directly into acetic acid[21]. And soon after the CO oxidation activity of CODH[22] was discovered along with the now ubiquitous nickel-iron-carbonyl (NiFeC) EPR signal generated by CO binding to ACS[23]. Over many decades, work by Wood and Ljungdahl along with many others was instrumental in identifying the enzymes and biochemical mechanisms responsible for this reductive acetyl-CoA pathway[22,24–26].

Both CODH and ACS are nickel iron-sulfur-cluster enzymes. The active site of CODH is the C-cluster, made up of a 3Fe4S1Ni cluster with a pendant Fe; this is where CO_2 reduction occurs (Figure 1-2). The CODH dimer contains two C-clusters, as well as two 4Fe4S B-clusters

and a 4Fe4S D-cluster at the dimer interface involved in electron transfer[27]. The active site of ACS is the A-cluster which is a dinickel 4Fe4S cluster with the nickels bridged by cysteines. The proximal nickel (Ni_p) is closest to the 4Fe4S cluster and binds the substrates while the distal nickel (Ni_d) plays a structural role[16,28].

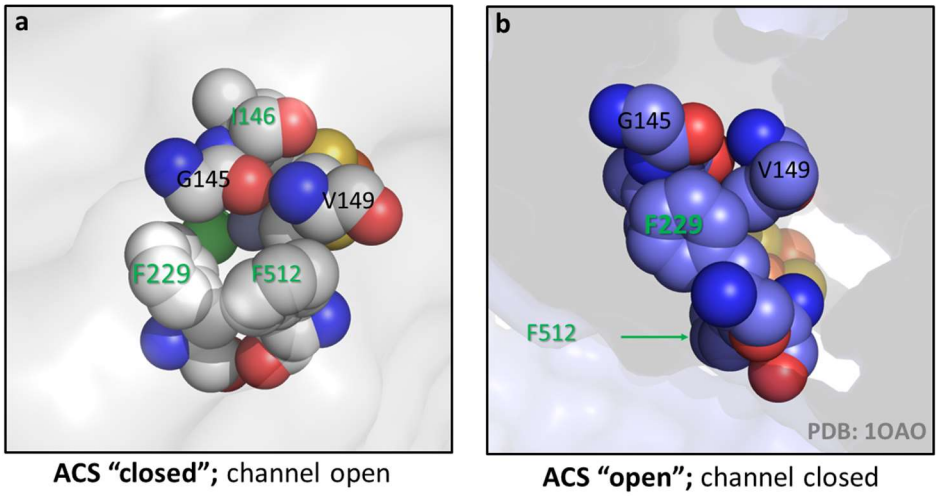

Figure 1-3 Close view of secondary sphere ligands surrounding the A-cluster. a) Viewer is in the CO tunnel looking toward the proximal nickel which is substituted with zinc (grey) in this structure. The A-cluster is inaccessible to solvent ("closed") and the CO tunnel is open allowing CO to bind. b) As the conformation of ACS becomes more open and solvent accessible, the secondary sphere residues rearrange with F229 swinging in to block off the CO tunnel.

Multiple conformations of ACS have been captured with x-ray crystallography and cryo-EM[17,29–31]. In crystal structures of the *Moorella thermoacetica* CODH/ACS complex, two states – designated open and closed – have been observed. In the open state, the A-cluster is slightly solvent accessible while the closed state is accessible to the internal CO tunnel (Figure 1-3). A set of five hydrophobic residues – G145, I146, V149, F229, F512 – were observed forming an alcove around the proximal nickel whose residues rearrange significantly between the two conformations [17,30]. In the open state, F229A is positioned to block off the exit of the CO tunnel preventing escape of this precious and toxic intermediate. In the closed state, F229A swings out of the way, allowing CO to be funneled directly to the Ni_p. More recent electron microscopy studies have identified additional extended conformations with domain 3 (containing the A-cluster) stretching away from domain 1 (bound to CODH). The extended structures are proposed to correspond to methylation while the closed structure allows CO to bind without being lost. The highly varied sizes of ACS's substrates (CO (0.028kDa), CoA (0.8kDA), CFeSP (88kDa))

requires these dramatic structural rearrangements for ACS to bind reactants and to catalyze its reaction [32–34].

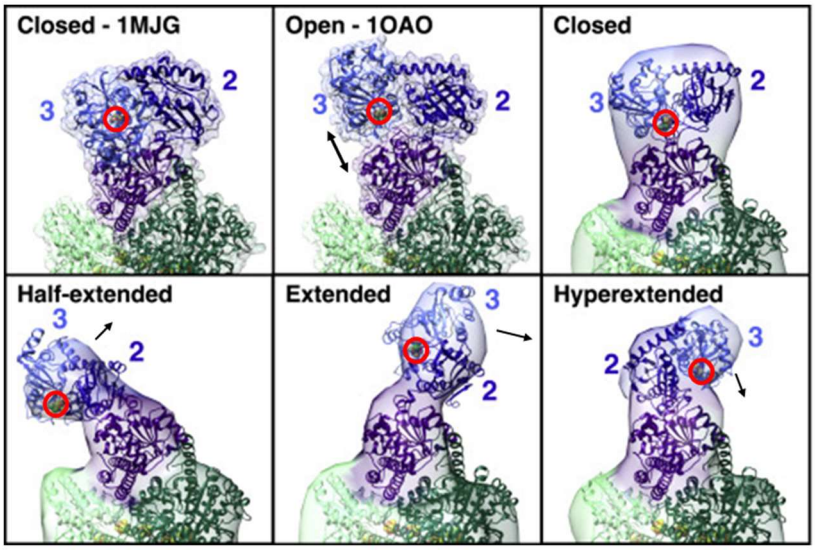

Figure 1-4 Domain Motions of CODH/ACS Crystal structures are shown in cartoon representation with transparent van der Waals (VDW) surfaces. Flexible fitting models are shown in cartoon representation with corresponding EM maps. These low resolution structures highlight the extreme movement of the ACS subunit. The A-cluster is circlesd in red and black arrows show direction of movement as the enzyme opens. Figure adapted from Figure 4. From Cohen et. al, 2020[33].

In 2021, the first structures of the *Clostridium autoethanogenum* (*Ca*) COHD/ACS complex were solved showing a rerouting of the internal gas tunnel to accommodate a different binding interface between the ACS and CODH subunits. In the *Ca* structure the ACS binds on a single monomer of CODH, rather than at the dimeric interface, by an extended C-terminal loop and helix not present in the *Moorella* sequence. The larger surface area of the *Mt* CODH/ACS interface likely leads to a stronger interaction and explains its greater stability in thermophilic conditions[31]. *Clostridium autoethanogenum* is a species discovered in rabbit feces and grows at a lower temperature (37˚C) than the thermophilic *Moorella thermoacetica* (55°C) [33]. Further characterization of this complex by cryoEM methods allowed greater resolution of the ACS domains and even visualization of coenzyme A bound in a pocket made of highly conserved

Chapter 2 of this dissertation will describe the effects of a point mutation to the alcove residue, F229. We investigated what the role of the alcove is in binding substrates at the A-cluster of ACS and how loss of the alcove impacts this ability. To examine this, we made two mutations; one to alanine (F229A) to look at the loss of this residue and one to tryptophan (F229W) should function similarly to the wild type. Characterization and comparison of these

mutants was done through XAS, EPR, IR, and UV-vis based kinetic assays and their differences are reported[36].

1.3 Paramagnetic vs Diamagnetic Mechanism

While the structure of CODH/ACS is well established, the mechanism of ACS is still contested. The general mechanism of ACS involved the binding of CO and the methyl group in a random order[18,37,38] although the case has been made that methylation must come before CO binding for productive acetyl formation [39,40]. After CO and methyl are both bound, they condense to form an acetyl group which undergoes a nucleophilic attack by coenzyme A (CoA) (thiolysis) to produce acetyl-CoA and regenerate the active site. While the hypothesis that each of these intermediates is bound directly to nickel has been generally accepted for a long time, it was only experimentally demonstrated recently with the characterization of the methyl and acetyl-nickel intermediates[28]. The nickel-bound CO has been observed by EPR[23] for a long time and in XAS as well[36,41].

.

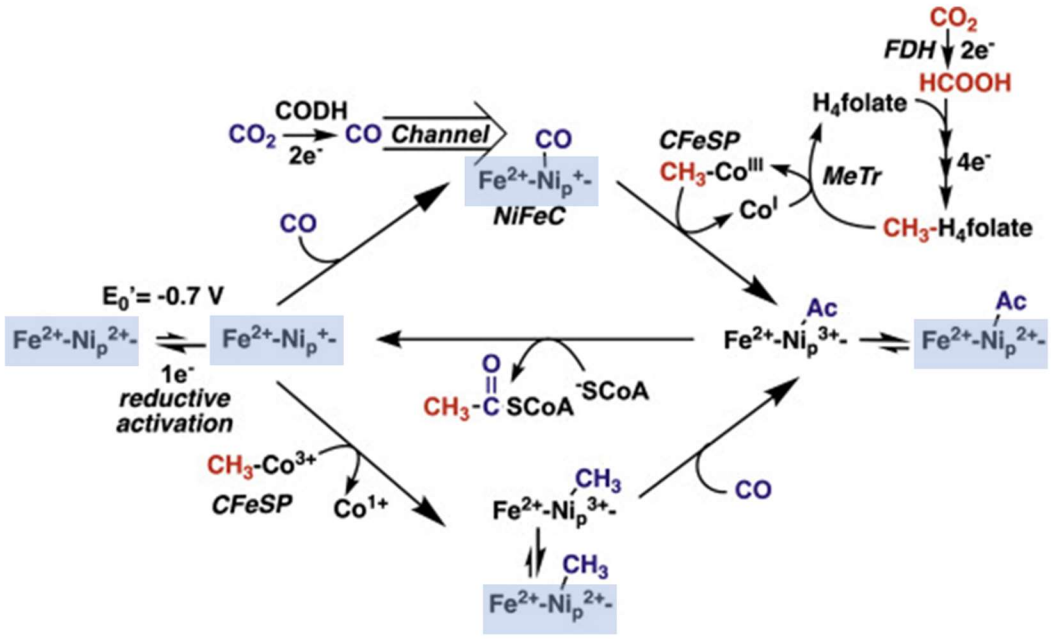

Figure 1-5 Proposed paramagnetic mechanism of ACS with previously characterized intermediates highlighted with blue boxes[23,28,40]. Modified from Fig 6 of Ragsdale, S.W. Comprehensive Coordination Chemistry III, Volume 8[18]

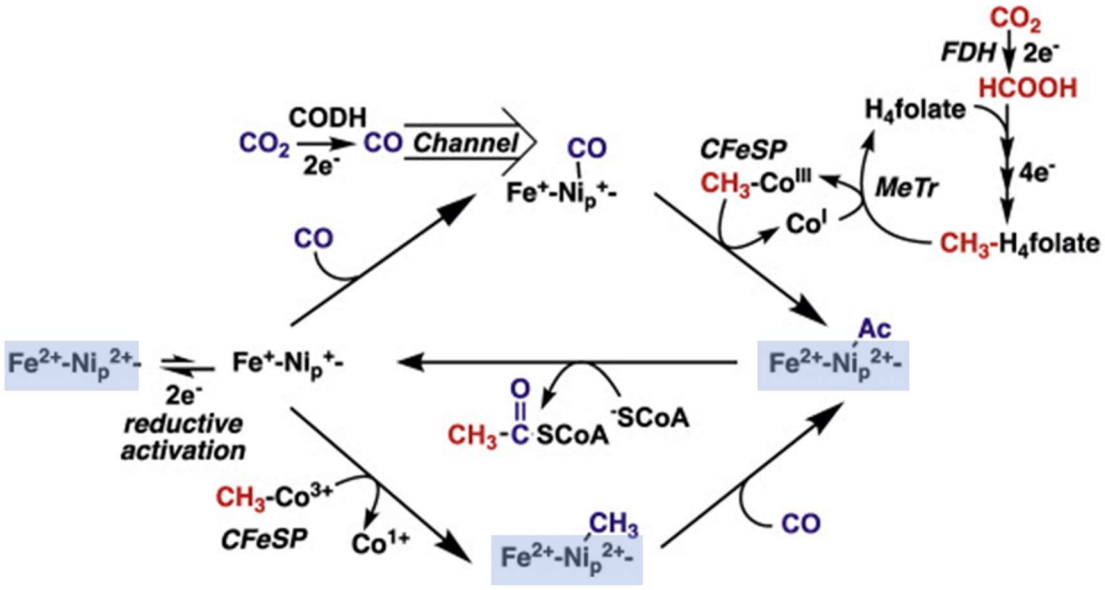

Figure 1-6 Proposed diamagnetic mechanism of ACS with previously characterized intermediates highlighted with blue boxes[28]. Modified from Fig 6 of Ragsdale, S.W. Comprehensive Coordination Chemistry III, Volume 8[18]

Many computational models[43–45] and small complex models[46–49] have tried to replicate the intermediates of ACS to gain insight into its complex mechanism but have yet to truly resolve the nature of ACS. The Mirica lab recently reported a new model of the A-cluster using nickel complexes supported by a tridentate macrocyclic ligand 1,4,7-triisopropyl-1,4,7-triazacyclononane (iPr3tacn) that modeled the CO, methyl, and acetyl bound involving both paramagnetic and diamagnetic intermediates. They found the binding of a second CO molecule promoted migratory insertion to form the acetyl intermediate and that one-electron oxidation of the nickel(II)-acetyl drove reductive elimination with an 1800 fold rate increase and a random binding order for CO and methyl was feasible[48]. Another model system that has provided great insight into the mechanism of ACS is the Shafaat lab's nickel azurin system. This modified azurin protein can coordinate a single nickel in its active site and replicate the binding of CO, methyl, acetyl, and thiolyze to form an acetyl-thiol, though it does not turnover to do multiple catalytic cycles. This system requires ordered binding of the methyl first followed by CO binding to form an acetyl-nickel. Their methyl intermediate displays an unusual inverted ligand field where the lowest unoccupied molecular orbital (LUMO) is centered on the ligands rather than the electropositive metal[39,46,47,50]. While these models and computational analyses provide insights into the mechanism of ACS and can even trap intermediates that have thus far been inaccessible in the protein itself, no model system can perfectly replicate all of the features of the

A-cluster, alcove, and flexible protein structure. The only way to confirm the hypotheses raised by these models is to study the enzyme itself.

The main mechanism debate concerns whether ACS proceeds through a series of paramagnetic (Figure 1-5) or diamagnetic (Figure 1-6) intermediates. This starts with what is the reductively activated species that enters the catalytic cycle; is it one or two electron reduced compared to the resting A_{ox} state? In the paramagnetic mechanism Ni^{1+}- $[4Fe4S]^{2+}$ and CO-Ni^{1+}- $[4Fe4S]^{2+}$ have both been trapped by EPR[23,42] while the nickel (II) methyl- and acetyl-intermediates[28] suggested by the diamagnetic mechanism have also been characterized. The reductively activate species for the paramagnetic mechanism is a Ni^{1+}- $[4Fe4S]^{2+}$ one-electron reduced species, while the diamagnetic mechanism calls for a two-electron reduced species, Ni^{1+}- $[4Fe4S]^{1+}$.

Chapters 3 and 4 of this dissertation will characterize more intermediates of this mechanism to try to provide new evidence for an electrochemically coupled paramagnetic mechanism that incorporates equilibria between the diamagnetic and paramagnetic states (Figure 1-5). Chapter 3 of this dissertation will describe characterization of the Ni(II)-methyl and Ni(II)-acetyl species by XAS, the first direct measurement of their nickel-bound state. Chapter 4 will examine a reduced form of the A-cluster after thiolysis of acetyl-CoA through XAS, Mössbauer, EPR, and redox titrations to identify its redox state.

1.4 References for Chapter 1

(1) Calvin, K.; Dasgupta, D.; Krinner, G.; Mukherji, A.; Thorne, P. W.; Trisos, C.; Romero, J.; Aldunce, P.; Barrett, K.; Blanco, G.; Cheung, W. W. L.; Connors, S.; Denton, F.; Diongue-Niang, A.; Dodman, D.; Garschagen, M.; Geden, O.; Hayward, B.; Jones, C.; Jotzo, F.; Krug, T.; Lasco, R.; Lee, Y.-Y.; Masson-Delmotte, V.; Meinshausen, M.; Mintenbeck, K.; Mokssit, A.; Otto, F. E. L.; Pathak, M.; Pirani, A.; Poloczanska, E.; Pörtner, H.-O.; Revi, A.; Roberts, D. C.; Roy, J.; Ruane, A. C.; Skea, J.; Shukla, P. R.; Slade, R.; Slangen, A.; Sokona, Y.; Sörensson, A. A.; Tignor, M.; Van Vuuren, D.; Wei, Y.-M.; Winkler, H.; Zhai, P.; Zommers, Z.; Hourcade, J.-C.; Johnson, F. X.; Pachauri, S.; Simpson, N. P.; Singh, C.; Thomas, A.; Totin, E.; Arias, P.; Bustamante, M.; Elgizouli, I.; Flato, G.; Howden, M.; Méndez-Vallejo, C.; Pereira, J. J.; Pichs-Madruga, R.; Rose, S. K.; Saheb, Y.; Sánchez Rodríguez, R.; Ürge-Vorsatz, D.; Xiao, C.; Yassaa, N.; Alegría, A.; Armour, K.; Bednar-Friedl, B.; Blok, K.; Cissé, G.; Dentener, F.; Eriksen, S.; Fischer, E.; Garner, G.; Guivarch, C.; Haasnoot, M.; Hansen, G.; Hauser, M.; Hawkins, E.; Hermans, T.; Kopp, R.; Leprince-Ringuet, N.; Lewis, J.; Ley, D.; Ludden, C.; Niamir, L.; Nicholls, Z.; Some, S.; Szopa, S.; Trewin, B.; Van Der Wijst, K.-I.; Winter, G.; Witting, M.; Birt, A.; Ha, M.; Romero, J.; Kim, J.; Haites, E. F.; Jung, Y.; Stavins, R.; Birt, A.; Ha, M.; Orendain, D. J. A.; Ignon, L.; Park, S.; Park, Y.; Reisinger, A.; Cammaramo, D.; Fischlin, A.; Fuglestvedt, J. S.; Hansen, G.; Ludden, C.; Masson-Delmotte, V.; Matthews, J. B. R.; Mintenbeck, K.; Pirani, A.; Poloczanska, E.; Leprince-Ringuet, N.; Péan, C. *IPCC, 2023: Climate Change 2023: Synthesis Report. Contribution of Working Groups I, II and III to the Sixth Assessment Report of the Intergovernmental Panel on Climate Change [Core Writing Team, H. Lee and J. Romero (Eds.)]. IPCC, Geneva, Switzerland.*, First.; Intergovernmental Panel on Climate Change (IPCC), 2023. https://doi.org/10.59327/IPCC/AR6-9789291691647.

(2) US EPA, O. *Climate Change Indicators: Heat-Related Deaths*. https://www.epa.gov/climate-indicators/climate-change-indicators-heat-related-deaths (accessed 2025-08-27).

(3) Poehlein, A.; Zeldes, B.; Flaiz, M.; Böer, T.; Lüschen, A.; Höfele, F.; Baur, K. S.; Molitor, B.; Kröly, C.; Wang, M.; Zhang, Q.; Fan, Y.; Chao, W.; Daniel, R.; Li, F.; Basen, M.; Müller, V.; Angenent, L. T.; Sousa, D. Z.; Bengelsdorf, F. R. Advanced

Aspects of Acetogens. *Bioresour. Technol.* **2025**, *427*, 131913. https://doi.org/10.1016/j.biortech.2024.131913.

(4) Rudolf K. Thauer,; Kurt Jungermann; Karl Decker. Energy Conservation in Chemotrophic Anaerobic Bacteria. *Bacteriol. Rev.* **1977**, *41* (1), 100–180. https://doi.org/10.1128/br.41.1.100-180.1977.

(5) Ragsdale, S. W. Enzymology of the Wood–Ljungdahl Pathway of Acetogenesis. *Ann. N. Y. Acad. Sci.* **2008**, *1125* (1), 129–136. https://doi.org/10.1196/annals.1419.015.

(6) Parkin, A.; Seravalli, J.; Vincent, K. A.; Ragsdale, S. W.; Armstrong, F. A. Rapid and Efficient Electrocatalytic CO_2 /CO Interconversions by *Carboxydothermus Hydrogenoformans* CO Dehydrogenase I on an Electrode. *J. Am. Chem. Soc.* **2007**, *129* (34), 10328–10329. https://doi.org/10.1021/ja073643o.

(7) Michael Köpke; Christophe Mihalcea; FungMin Liew; Joseph H. Tizard; Mohammed S. Ali; Joshua J. Conolly; Bakir Al-Sinawi; Séan D. Simpson. 2,3-Butanediol Production by Acetogenic Bacteria, an Alternative Route to Chemical Synthesis, Using Industrial Waste Gas. *Appl. Environ. Microbiol.* **2011**, *77* (15), 5467–5475. https://doi.org/10.1128/AEM.00355-11.

(8) Valgepea, K.; Loi, K. Q.; Behrendorff, J. B.; Lemgruber, R. de S. P.; Plan, M.; Hodson, M. P.; Köpke, M.; Nielsen, L. K.; Marcellin, E. Arginine Deiminase Pathway Provides ATP and Boosts Growth of the Gas-Fermenting Acetogen *Clostridium Autoethanogenum*. *Metab. Eng.* **2017**, *41*, 202–211. https://doi.org/10.1016/j.ymben.2017.04.007.

(9) Alissandratos, A.; Kim, H.-K.; Easton, C. J. Formate Production through Biocatalysis. *Bioengineered* **2013**, *4* (5), 348–350. https://doi.org/10.4161/bioe.25360.

(10) Fast, A. G.; Schmidt, E. D.; Jones, S. W.; Tracy, B. P. Acetogenic Mixotrophy: Novel Options for Yield Improvement in Biofuels and Biochemicals Production. *Curr. Opin. Biotechnol.* **2015**, *33*, 60–72. https://doi.org/10.1016/j.copbio.2014.11.014.

(11) Fackler, N.; Heijstra, B. D.; Rasor, B. J.; Brown, H.; Martin, J.; Ni, Z.; Shebek, K. M.; Rosin, R. R.; Simpson, S. D.; Tyo, K. E.; Giannone, R. J.; Hettich, R. L.; Tschaplinski, T. J.; Leang, C.; Brown, S. D.; Jewett, M. C.; Köpke, M. Stepping on the Gas to a Circular Economy: Accelerating Development of Carbon-Negative Chemical Production from

Gas Fermentation. *Annu. Rev. Chem. Biomol. Eng.* **2021**, *12* (1), 439–470. https://doi.org/10.1146/annurev-chembioeng-120120-021122.

(12) Weiss, M. C.; Preiner, M.; Xavier, J. C.; Zimorski, V.; Martin, W. F. The Last Universal Common Ancestor between Ancient Earth Chemistry and the Onset of Genetics. *PLOS Genet.* **2018**, *14* (8), e1007518. https://doi.org/10.1371/journal.pgen.1007518.

(13) Fuchs, G. Alternative Pathways of Carbon Dioxide Fixation: Insights into the Early Evolution of Life? *Annu. Rev. Microbiol.* **2011**, *65* (1), 631–658. https://doi.org/10.1146/annurev-micro-090110-102801.

(14) Weiss, M. C.; Sousa, F. L.; Mrnjavac, N.; Neukirchen, S.; Roettger, M.; Nelson-Sathi, S.; Martin, W. F. The Physiology and Habitat of the Last Universal Common Ancestor. *Nat. Microbiol.* **2016**, *1* (9), 16116. https://doi.org/10.1038/nmicrobiol.2016.116.

(15) Ragsdale, S. W.; Pierce, E. Acetogenesis and the Wood-Ljungdahl Pathway of CO(2) Fixation. *Biochim. Biophys. Acta* **2008**, *1784* (12), 1873–1898. https://doi.org/10.1016/j.bbapap.2008.08.012.

(16) Burton, R.; Can, M.; Esckilsen, D.; Wiley, S.; Ragsdale, S. W. Chapter Twelve - Production and Properties of Enzymes That Activate and Produce Carbon Monoxide. In *Methods in Enzymology*; Armstrong, F., Ed.; Enzymes of Energy Technology; Academic Press, 2018; Vol. 613, pp 297–324. https://doi.org/10.1016/bs.mie.2018.10.005.

(17) Doukov, T. I.; Blasiak, L. C.; Seravalli, J.; Ragsdale, S. W.; Drennan, C. L. Xenon in and at the End of the Tunnel of Bifunctional Carbon Monoxide Dehydrogenase/Acetyl-CoA Synthase,. *Biochemistry* **2008**, *47* (11), 3474–3483. https://doi.org/10.1021/bi702386t.

(18) Ragsdale, S. W. 8.24 - Biological Carbon Fixation by an Organometallic Pathway: Evidence Supporting the Paramagnetic Mechanism of the Nickel-Iron-Sulfur Acetyl-CoA Synthase. In *Comprehensive Coordination Chemistry III*; Constable, E. C., Parkin, G., Que Jr, L., Eds.; Elsevier: Oxford, 2021; pp 611–633. https://doi.org/10.1016/B978-0-08-102688-5.00082-9.

(19) F. E. Fontaine; W. H. Peterson; Elizabeth McCoy; Marvin J. Johnson; George J. Ritter. A New Type of Glucose Fermentation by Clostridium Thermoaceticum. *J. Bacteriol.* **1942**, *43* (6), 701–715. https://doi.org/10.1128/jb.43.6.701-715.1942.

(20) Elizabeth Pierce; Gary Xie; Ravi D. Barabote; Elizabeth Saunders; Cliff S. Han; John C. Detter; Paul Richardson; Thomas S. Brettin; Amaresh Das; Lars G. Ljungdahl; Stephen

W. Ragsdale. The Complete Genome Sequence of Moorella Thermoacetica (f. Clostridium Thermoaceticum) - Pierce - 2008 - Environmental Microbiology - Wiley Online Library. *Environ. Microbiol.* **2008**, *10* (10). https://doi.org/10.1111/j.1462-2920.2008.01679.x.

(21) Barker, H. A. On the Rôle of Carbon Dioxide in the Metabolism of Clostridium Thermoaceticum. *Proc. Natl. Acad. Sci.* **1944**, *30* (4), 88–90. https://doi.org/10.1073/pnas.30.4.88.

(22) Diekert, G. B.; Thauer, R. K. Carbon Monoxide Oxidation by Clostridium Thermoaceticum and Clostridium Formicoaceticum. *J. Bacteriol.* **1978**, *136* (2), 597–606. https://doi.org/10.1128/jb.136.2.597-606.1978.

(23) Ragsdale, S. W.; Wood, H. G.; Antholine, W. E. Evidence That an Iron-Nickel-Carbon Complex Is Formed by Reaction of CO with the CO Dehydrogenase from Clostridium Thermoaceticum. *Proc. Natl. Acad. Sci.* **1985**, *82* (20), 6811–6814. https://doi.org/10.1073/pnas.82.20.6811.

(24) Ragsdale, S. W.; Ljungdahl, L. G.; DerVartanian, D. V. EPR Evidence for Nickel-Substrate Interaction in Carbon Monoxide Dehydrogenase from Clostridium Thermoaceticum. *Biochem. Biophys. Res. Commun.* **1982**, *108* (2), 658–663. https://doi.org/10.1016/0006-291X(82)90880-4.

(25) Ljungdahl, L.; Wood, H. G. Incorporation of C14 from Carbon Dioxide into Sugar Phosphates, Carboxylic Acids, and Amino Acids by Clostridium Thermoaceticum. *J. Bacteriol.* **1965**, *89* (4), 1055–1064. https://doi.org/10.1128/jb.89.4.1055-1064.1965.

(26) Ljungdhal, L. G. The Autotrophic Pathway of Acetate Synthesis in Acetogenic Bacteria. *Annu. Rev. Microbiol.* **1986**, *40* (Volume 40,), 415–450. https://doi.org/10.1146/annurev.mi.40.100186.002215.

(27) Aboulhosn, K.; Ragsdale, S. W. Expression, Purification, and Activation of One Key Enzyme in Anaerobic CO2 Fixation: Carbon Monoxide Dehydrogenase II from *Carboxydothermus Hydrogenoformans*. In *Methods in Enzymology*; Maurice, M. St., Ed.; Carboxylases; Academic Press, 2024; Vol. 708, pp 237–256. https://doi.org/10.1016/bs.mie.2024.10.016.

(28) Can, M.; Abernathy, M. J.; Wiley, S.; Griffith, C.; James, C. D.; Xiong, J.; Guo, Y.; Hoffman, B. M.; Ragsdale, S. W.; Sarangi, R. Characterization of Methyl- and Acetyl-Ni

Intermediates in Acetyl CoA Synthase Formed during Anaerobic CO_2 and CO Fixation. *J. Am. Chem. Soc.* **2023**, *145* (25), 13696–13708. https://doi.org/10.1021/jacs.3c01772.

(29) Max Dongsheng Yin; Olivier N. Lemaire; José Guadalupe Rosas Jiménez; Mélissa Belhamri; Anna Shevchenko; Gerhard Hummer; Tristan Wagner; Bonnie J. Murphy. Conformational Dynamics of a Multienzyme Complex in Anaerobic Carbon Fixation | Science. *Science* **2025**, *387*, 494–504. https://doi.org/10.1126/science.adr9672.

(30) Darnault, C.; Volbeda, A.; Kim, E. J.; Legrand, P.; Vernède, X.; Lindahl, P. A.; Fontecilla-Camps, J. C. Ni-Zn-[Fe4-S4] and Ni-Ni-[Fe4-S4] Clusters in Closed and Open α Subunits of Acetyl-CoA Synthase/Carbon Monoxide Dehydrogenase. *Nat. Struct. Mol. Biol.* **2003**, *10* (4), 271–279. https://doi.org/10.1038/nsb912.

(31) Lemaire, O. N.; Wagner, T. Gas Channel Rerouting in a Primordial Enzyme: Structural Insights of the Carbon-Monoxide Dehydrogenase/Acetyl-CoA Synthase Complex from the Acetogen Clostridium Autoethanogenum. *Biochim. Biophys. Acta BBA - Bioenerg.* **2021**, *1862* (1), 148330. https://doi.org/10.1016/j.bbabio.2020.148330.

(32) Ruickoldt, J.; Kreibich, J.; Bick, T.; Jeoung, J.-H.; Duffus, B. R.; Leimkühler, S.; Dobbek, H.; Wendler, P. Ligand Binding to a Ni–Fe Cluster Orchestrates Conformational Changes of the CO-Dehydrogenase–Acetyl-CoA Synthase Complex. *Nat. Catal.* **2025**, *8* (7), 657–667. https://doi.org/10.1038/s41929-025-01365-y.

(33) Yin, M. D.; Lemaire, O. N.; Rosas Jiménez, J. G.; Belhamri, M.; Shevchenko, A.; Hummer, G.; Wagner, T.; Murphy, B. J. Conformational Dynamics of a Multienzyme Complex in Anaerobic Carbon Fixation. *Science* **2025**, *387* (6733), 498–504. https://doi.org/10.1126/science.adr9672.

(34) Cohen, S. E.; Brignole, E. J.; Wittenborn, E. C.; Can, M.; Thompson, S.; Ragsdale, S. W.; Drennan, C. L. Negative-Stain Electron Microscopy Reveals Dramatic Structural Rearrangements in Ni-Fe-S-Dependent Carbon Monoxide Dehydrogenase/Acetyl-CoA Synthase. *Struct. Lond. Engl. 1993* **2021**, *29* (1), 43-49.e3. https://doi.org/10.1016/j.str.2020.08.011.

(35) Abrini, J.; Naveau, H.; Nyns, E.-J. Clostridium Autoethanogenum, Sp. Nov., an Anaerobic Bacterium That Produces Ethanol from Carbon Monoxide. *Arch. Microbiol.* **1994**, *161* (4), 345–351. https://doi.org/10.1007/BF00303591.

(36) Wiley, S.; Griffith, C.; Eckert, P.; Mueller, A. P.; Nogle, R.; Simpson, S. D.; Köpke, M.; Can, M.; Sarangi, R.; Kubarych, K.; Ragsdale, S. W. An Alcove at the Acetyl-CoA Synthase Nickel Active Site Is Required for Productive Substrate CO Binding and Anaerobic Carbon Fixation. *J. Biol. Chem.* **2024**, *300* (8), 107503. https://doi.org/10.1016/j.jbc.2024.107503.

(37) Seravalli, J.; Ragsdale, S. W. Pulse-Chase Studies of the Synthesis of Acetyl-CoA by Carbon Monoxide Dehydrogenase/Acetyl-CoA Synthase: EVIDENCE FOR A RANDOM MECHANISM OF METHYL AND CARBONYL ADDITION*. *J. Biol. Chem.* **2008**, *283* (13), 8384–8394. https://doi.org/10.1074/jbc.M709470200.

(38) Seravalli, J.; Kumar, M.; Ragsdale, S. W. Rapid Kinetic Studies of Acetyl-CoA Synthesis: Evidence Supporting the Catalytic Intermediacy of a Paramagnetic NiFeC Species in the Autotrophic Wood−Ljungdahl Pathway. *Biochemistry* **2002**, *41* (6), 1807–1819. https://doi.org/10.1021/bi011687i.

(39) Kisgeropoulos, E. C.; Manesis, A. C.; Shafaat, H. S. Ligand Field Inversion as a Mechanism to Gate Bioorganometallic Reactivity: Investigating a Biochemical Model of Acetyl CoA Synthase Using Spectroscopy and Computation. *J. Am. Chem. Soc.* **2021**, *143* (2), 849–867. https://doi.org/10.1021/jacs.0c10135.

(40) Gencic, S.; Duin, E. C.; Grahame, D. A. The Two-Electron Reduced A Cluster in Acetyl-CoA Synthase: Preparation, Characteristics and Mechanistic Implications. *J. Inorg. Biochem.* **2023**, *240*, 112098. https://doi.org/10.1016/j.jinorgbio.2022.112098.

(41) Can, M.; Giles, L. J.; Ragsdale, S. W.; Sarangi, R. X-Ray Absorption Spectroscopy Reveals an Organometallic Ni–C Bond in the CO-Treated Form of Acetyl-CoA Synthase. *Biochemistry* **2017**, *56* (9), 1248–1260. https://doi.org/10.1021/acs.biochem.6b00983.

(42) Bender, G.; Stich, T. A.; Yan, L.; Britt, R. D.; Cramer, S. P.; Ragsdale, S. W. Infrared and EPR Spectroscopic Characterization of a Ni(I) Species Formed by Photolysis of a Catalytically Competent Ni(I)-CO Intermediate in the Acetyl-CoA Synthase Reaction. *Biochemistry* **2010**, *49* (35), 7516–7523. https://doi.org/10.1021/bi1010128.

(43) Harrop, T. C.; Mascharak, P. K. Structural and Spectroscopic Models of the A-Cluster of Acetyl Coenzyme a Synthase/Carbon Monoxide Dehydrogenase: Nature's Monsanto Acetic Acid Catalyst. *Coord. Chem. Rev.* **2005**, *249* (24), 3007–3024. https://doi.org/10.1016/j.ccr.2005.04.019.

(44) Matsumoto, T.; Ito, M.; Kotera, M.; Tatsumi, K. A Dinuclear Nickel Complex Modeling of the Nid(II)-Nip(I) State of the Active Site of Acetyl CoA Synthase. *Dalton Trans.* **2010**, *39* (12), 2995–2997. https://doi.org/10.1039/B924915J.

(45) Chmielowska, A.; Lodowski, P.; Jaworska, M. Redox Potentials and Protonation of the A-Cluster from Acetyl-CoA Synthase. A Density Functional Theory Study. *J. Phys. Chem. A* **2013**, *117* (47), 12484–12496. https://doi.org/10.1021/jp402616e.

(46) Manesis, A. C.; Yerbulekova, A.; Shearer, J.; Shafaat, H. S. Thioester Synthesis by a Designed Nickel Enzyme Models Prebiotic Energy Conversion. *Proc. Natl. Acad. Sci.* **2022**, *119* (30), e2123022119. https://doi.org/10.1073/pnas.2123022119.

(47) Manesis, A. C.; O'Connor, M. J.; Schneider, C. R.; Shafaat, H. S. Multielectron Chemistry within a Model Nickel Metalloprotein: Mechanistic Implications for Acetyl-CoA Synthase. *J. Am. Chem. Soc.* **2017**, *139* (30), 10328–10338. https://doi.org/10.1021/jacs.7b03892.

(48) Nath, S.; Griego, L.; Mirica, L. M. The Mechanism of Acetyl-CoA Synthase through the Lens of a Nickel Model System. *Nat. Commun.* **2025**, *16* (1), 5177. https://doi.org/10.1038/s41467-025-60163-z.

(49) Ito, M.; Kotera, M.; Matsumoto, T.; Tatsumi, K. Dinuclear Nickel Complexes Modeling the Structure and Function of the Acetyl CoA Synthase Active Site. *Proc. Natl. Acad. Sci. U. S. A.* **2009**, *106* (29), 11862–11866. https://doi.org/10.1073/pnas.0900433106.

(50) Manesis, A. C.; Shafaat, H. S. Electrochemical, Spectroscopic, and Density Functional Theory Characterization of Redox Activity in Nickel-Substituted Azurin: A Model for Acetyl-CoA Synthase. *Inorg. Chem.* **2015**, *54* (16), 7959–7967. https://doi.org/10.1021/acs.inorgchem.5b01103.

Chapter 2 An Alcove at the Acetyl-CoA Synthase Nickel Active Site is Required for Productive Substrate CO Binding and Anaerobic Carbon Fixation

2.1 Abstract

One of the seven natural CO_2 fixation pathways, the anaerobic Wood-Ljungdahl pathway (WLP) is unique in generating CO as a metabolic intermediate, operating through organometallic intermediates, and in conserving (*versus* utilizing) net ATP. The key enzyme in the WLP is acetyl-CoA synthase (ACS), which uses an active site [2Ni-4Fe-4S] cluster (A-cluster), a CO tunnel, and an organometallic (Ni-CO, Ni-methyl, and Ni-acetyl) reaction sequence to generate acetyl-CoA. Here, we reveal that an alcove, which interfaces the tunnel and the A-cluster, is essential for CO_2 fixation and autotrophic growth by the WLP. *In vitro* spectroscopy, kinetics, binding, and *in vivo* growth experiments reveal that a Phe229A substitution at one wall of the alcove decreases CO affinity thirty-fold and abolishes autotrophic growth; however, a F229W substitution enhances CO binding 80-fold. Our results indicate that the structure of the alcove is exquisitely tuned to concentrate CO near the A-cluster; protect ACS from CO loss during catalysis, provide a haven for inhibitory CO, and stabilize the tetrahedral coordination at the Ni_p site where CO binds. The directing, concentrating, and protective effects of the alcove explain the inability of F209A to grow autotrophically. The alcove also could help explain current controversies over whether ACS binds CO and methyl through a random or ordered mechanism. Our work redefines what we historically refer to as the metallocenter "active site". The alcove is so crucial for enzymatic function that we propose it is *part of* the active site. The community should now look for such alcoves in all "gas handling" metalloenzymes.

2.2 Introduction

An existential threat facing humanity is the increasing global concentration of carbon dioxide in the atmosphere, affecting wide-reaching aspects such as rising sea levels, ocean

acidification, and severe climate conditions (1, 2). There is an urgent need to better understand carbon fixation and apply this information to enhance CO_2 uptake from the atmosphere and efficiently convert it into fuels and valuable chemicals (3, 4, 5). There are seven known CO_2 fixation pathways and among these, the Wood-Ljungdahl (or reductive acetyl-CoA) pathway (WLP) exhibits high energy efficiency and is the only one that generates net ATP (Fig. 1*A*). The WLP is widely distributed in nature and is responsible for the production of acetic acid, an important chemical intermediate and microbial nutrient in anaerobic environments, including the gastrointestinal tracts of humans and ruminants, soil, bogs, marshes, and sediments (6). Found in strictly anaerobic microbes, this pathway allows acetogenic microbes to grow on H_2 and CO_2 as their sole energy and carbon sources and is important to the origin and evolution of life, as it was present in the last universal common ancestor (7). The WLP can also drive growth of anaerobic methanotrophic archaea on methane (8) and operate in reverse to allow microbes, *e.g.*, methanogens and sulfate reducers, to grow on acetate (9). The WLP is unique among biochemical pathways in using both CO_2 and CO, generating CO as a metabolic intermediate, operating through organometallic intermediates, and generating acetyl-CoA as an energy source and metabolic building block (9) (Fig. 1*A*). Here, we report that a molecular alcove in the key WLP enzyme, acetyl-CoA synthase (ACS), is required for CO_2 fixation. Without this alcove, the WLP cannot function because ACS cannot productively bind CO to form the key Ni-CO intermediate.

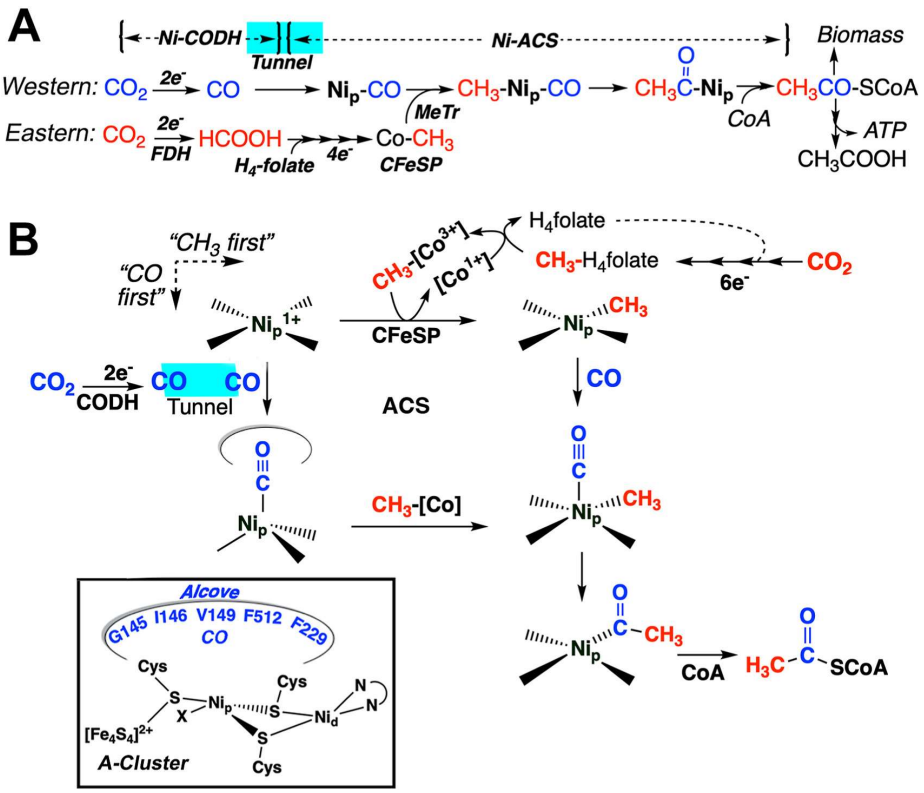

Figure 2-1 **An alcove in the Wood-Ljungdahl pathway (WLP) of anaerobic CO_2 fixation.** *A*, focus on CODH, ACS, and the organometallic nature of the pathway. One CO_2 enters the WLP at the Eastern (Methyl) branch (*red*), where it undergoes 2-electron reduction to formate by FDH), followed by 4-electron reduction to a methyl group methyltetrahydrofolate (CH_3-THF), and transferred to the B_{12} center of the CFeSP (Co-CH_3). In the Western (carbonyl) branch (*blue*), the other CO_2 undergoes enzymatic 2-electron reduction by CODH to CO, which migrates to the Ni_p site in the A-cluster of ACS through a tunnel, which is tightly interfaced to the A-cluster. The A-cluster reacts with CH_3-[Co] to generate CH_3-Ni, binds CO, and undergoes C-C bond formation to form acetyl-Ni, and then reacts with CoA to generate acetyl-CoA, which serves as a metabolic building block for all carbon-containing molecules in the organism and as a source of ATP, through the enzymatic reactions of phosphotransacetylase and acetate kinase. *B*, catalytic mechanism of ACS and introduction of the alcove in the WLP. The Ni_p site of the A-cluster of ACS react first with either CO or methyl-Co, generated as described above, then the other substrate, and finally with CoA. The A-cluster and the residues of the Alcove are depicted in the inset. See the text for further details. ACS, acetyl-CoA synthase; CODH, carbon monoxide dehydrogenase; CFeSP, the corrinoid iron-sulfur protein; FDH, formate dehydrogenase; WLP, Wood-Ljungdahl pathway.

The central enzymes in the WLP are carbon monoxide dehydrogenase (CODH) and ACS, encoded by the *acsA* and *acsB* genes, which assemble into a heterotetrameric $(\alpha\beta)_2$ enzyme complex (CODH/ACS) containing seven [Fe_4S_4] clusters (9) (Fig. 2-2). Each αβ dimer, contains two unique nickel clusters: the C-cluster of CODH (a Ni-Fe_4S_4 cluster), which catalyzes CO_2 reduction to CO, and the A-cluster of ACS (a Ni_2-Fe_4S_4 cluster (Figs. 2-1*B* and 2-2), which is responsible for acetyl-CoA synthesis. CO is generated at the CODH C-cluster and then migrates 70 Å through an interprotein gas tunnel to the ACS A-Cluster (10), where one (Ni_p) of the two Ni A-cluster binds nascent CO and a methyl group, donated by the

methylated corrinoid iron-sulfur protein (CFeSP), to form Ni-CO (11, 12) or Ni-methyl intermediates (13) (Fig. 2-1*A*). ACS can productively and randomly bind either CO or methyl as the first substrate (14), then catalyze C-C bond formation to form a Ni-acetyl (13) intermediate, which reacts with CoA to generate acetyl-CoA (Fig. 2-1*B*) (9).

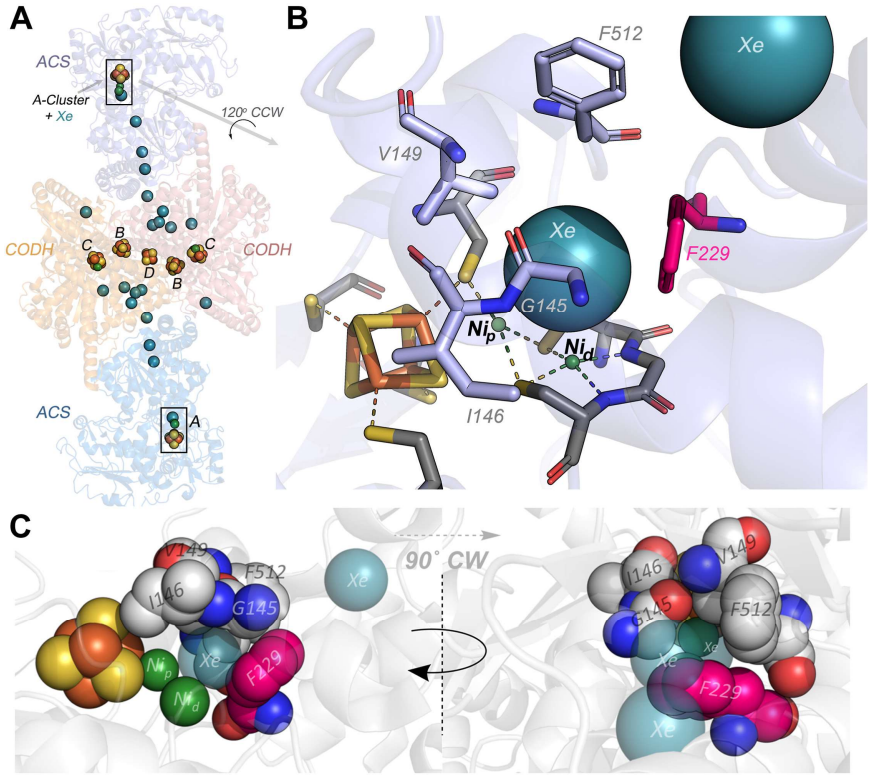

Figure 2-2 **Crystal structure of Xe-bound CODH-ACS, with focus on the alcove in ACS.** Crystal structure of (*A*) the CODH/ACS complex obtained under high-pressures of Xenon (*teal spheres*) to reveal the gas channel and show the 7 clusters in CODH (B–D) and ACS (A) involved in electron transfer and catalysis (C and A). *B*, expanded view of the A-cluster of ACS, highlighting the CO tunnel spanning from the CODH C-cluster (not shown) to the ACS A-cluster, with nearby residues as *spheres*. The residues that form the Alcove (Fig. 1*B*) are shown surrounding one of the Xe atoms. *C*, side-on perspective of the A-cluster, showing the alcove's role in maintaining CO near Ni_p, with F229 shown in *magenta*. (*left*) Down-tunnel perspective, 90˚ CW toward viewer (relative to (*right*)), showing how F229 and nearby residues form an opening for CO to reach the A-cluster. Stereoscopic versions of these images are found in the supplemental materials (Figs. S4 and S5). PDB 2Z8Y. ACS, acetyl-CoA synthase; CODH, carbon monoxide dehydrogenase; CW, clockwise; PDB, Protein Data Bank.

Earlier kinetic, spectroscopic, and structural studies identified a constellation of hydrophobic residues at the end of this tunnel near the proximal nickel center in the A-cluster (10, 15, 16) (Figs. 2-1*B* and 2-2). The X-ray crystallographic structure of CODH/ACS, obtained under a xenon overpressure, revealed a xenon atom cradled in a hydrophobic basket of residues (F229, I146, F512, V149, and G145) at the end of the CO tunnel only 3.5 Å from Ni_p of the A-cluster (Fig. 2) (10). Bender, *et al.* (15) showed that low-temperature photolysis of the Ni-CO intermediate generates a species that lacks the characteristic Ni(I)-C≡O electron paramagnetic

resonance (EPR) and infrared (IR) signals and yields a new EPR signal corresponding to a CO-cleaved $Ni_p(I)$ species. Temperature-dependent kinetic studies revealed an activation energy barrier for CO rebinding of <1 kJ/mol, suggesting that CO migrates freely between Ni_p and a putative "alcove". Here, we use *in vitro* and *in vivo* experiments to compare the properties of variant enzymes in two acetogens (*Moorella thermoacetica* and Clostridium *autoethanogenum*) with the WT proteins and establish that this CO alcove is required for productive interactions between ACS and substrate CO to form the key Ni-CO intermediate in the WLP. Disruption of this alcove prevents CO_2 fixation and autotrophic growth by this pathway. This work demonstrates that the CO alcove is a required and integral component of the A-cluster active site.

2.3 Results

2.3.1 An intact alcove is required for productive carbonylation of ACS

To investigate the role of the alcove, we made substitutions in a residue (F229) that forms one of its walls in the well-characterized ACS from *M. thermoacetica* and compared the properties of F229A and a conservative F229W with those of WT ACS (Table 2-1). We hypothesized that this mutation would open one wall of the alcove by replacing the bulky benzene group of Phe (accessible surface area, 220.0 A^2) (17) with the small hydrophobic methyl group in Ala (121.0 A^2), and examined the effect of substitution with Trp (264.0 A^2). Both variants exhibit a metal content very similar to that of WT protein, consistent with near complete occupancy of the A-cluster (Table S1).

Table 2-1 Monitoring methylation activity of ACS variants by single-turnover stopped-flow kinetics

Variant	**390 nm**			**470 nm**		
	k_{obs} (s^{-1})[a]	**Relaxation factor or stretch (β)[a]**	**Max conversion percent[b]**	**k_{obs} (s^{-1})[a]**	**Relaxation factor or stretch (β)[a]**	**Max conversion percent[b]**
WT	0.0464 (±0.0006)	0.575 (±0.005)	84.5 (±0.2)	0.0781 (±0.0009)	0.783 (±0.009)	57.8 (±0.6)
F229W	0.180 (±0.002)	0.573 (±0.004)	71 (±1)	0.164 (±0.002)	0.709 (±0.008)	60 (±2)

F229A	0.124 (±0.001)	0.533 (±0.005)	74.4 (±0.6)	0.105 (±0.002)	0.72 (±0.01)	74 (±2)

[a] The methylation data (Fig. 2-7) are best fit by a stretched exponential, which includes a "relaxation" factor (β) allowing for a distribution of rate constants. The equation for the stretched exponential fit is $y = c + Ae^{(-(kt)^{\beta})}$, where $0 < \beta \leq 1$.

[b] Maximum percent conversion of MeCbi to Co(I)-Cbi based on their extinction coefficients. At 390 nm, $\varepsilon_{390,MeCbi}$ = 8 mM^{-1} cm^{-1} and $\varepsilon_{390,Co(I)\text{-}Cbi}$ = 25 mM^{-1} cm^{-1}, so $\Delta\varepsilon_{390}$ = 17 mM^{-1}. At 470 nm, $\varepsilon_{470,MeCbi}$ = 11 mM^{-1} cm^{-1} and $\varepsilon_{470,Co(I)bi}$ = 3 mM^{-1} cm^{-1}, thus $\Delta\varepsilon_{470}$ = 8 mM^{-1} cm^{-1}.

CO binding to ACS was directly monitored by FTIR and EPR spectroscopies. Incubation of the F229W variant with CO leads to an intense 1995 cm^{-1} FTIR signal, which is assigned to the stretching frequency of the nickel-carbonyl of the A-cluster (18) and is similar to that of the WT protein (Fig. 2-3*A*). Transient kinetic experiments have shown that this Ni(I)-CO IR band appears upon reaction of CODH/ACS with CO (19) and disappears at catalytically competent rates (*i.e.* faster than the steady-state rate of acetyl-CoA synthesis) when the Ni-CO complex is reacted with the methylated CFeSP (20).

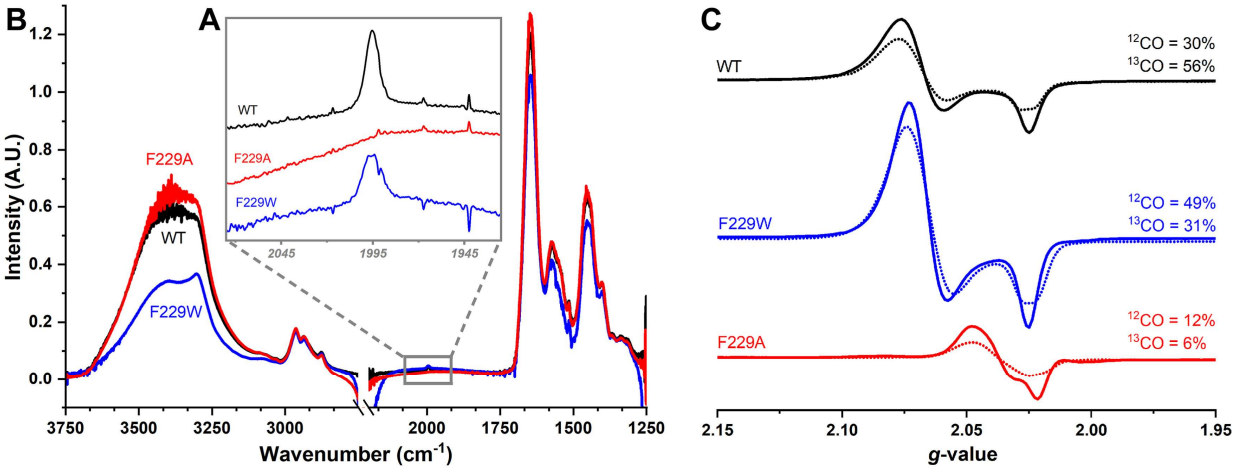

Figure 2-3 **FTIR and EPR spectra of ACS variants.** *A*, FTIR: highlight of the characteristic Ni-CO IR stretch at 1995 cm^{-1} between the region 1970 to 2020 cm^{-1}. The Ni-CO stretch is noticeably absent in F229A, while the WT and F229W have strong Ni-CO signals. The integrated area of the F229W Ni-CO peak is 83% of the WT area. The protein concentrations were as follows: WT, 580 ± 12 µM; F229W, 590 ± 26 µM, and F229A, 580 ± 16 µM. *B*, the full spectra of the ACS variants showing global folding similarity. Bands belonging to ACS include the various amide bands over the 1250 to 1750 cm^{-1}, the C-H bonds from 2800 to 3000 cm^{-1}, and the N-H and O-H stretches from 3200 to 3750 cm^{-1}. The region between 2200 to 2750 cm^{-1} was omitted due to strong D_2O signals obscuring the spectra. *C*, EPR spectra of the ACS variants exposed to naturally abundant ^{12}CO (—) compared with isotopically labeled ^{13}CO (---). Quantified spin percentages are listed on the right as NA%/^{13}CO%. The ^{13}C splitting is most prominent at g = 2.028. Less intense broadening can be seen at 2.08 for WT and F229W, and at 2.062, 2.057, and 2.024 for the F229A variant. The protein concentrations for the EPR were 236 µM (WT), 280 µM (F229A), 276 µM (F229W) and the spin concentrations are shown. ACS, acetyl-CoA synthase; EPR, electron paramagnetic resonance; IR, infrared; NA, natural abundance.

While the F229W variant was proficient at CO binding, the F229A variant lacks any obvious FTIR signal in the 1980 to 2150 cm^{-1} range (Figs. 2-3*A* and S1). However, the similarity of the FTIR spectra for the variants and WT proteins in the amide (1250–1750 cm^{-1}) and C-H (2800–3000 cm^{-1}) regions (Fig. 2-3) indicate that the mutations did not cause a broad protein disruption and that the decreased CO affinity of the F229A variant is not due to global protein misfolding.

When the ACS F229W variant was incubated with CO, formation of the paramagnetic Ni(I)-CO (NiFeC) species was observed by EPR (Fig. 2-3*C*). Its intensity and *g*-values (at 2.074 and 2.028) were characteristic of the WT protein (21). In contrast, the CO-incubated F229A variant showed 3- to 4-fold less intensity than that of WT and F229W and a marked shift in the *g*-values to 2.062, 2.046, and 2.028. By incubating ACS with ^{13}CO, line broadening of the EPR spectrum was observed for all variants, unambiguously demonstrating that CO binds to their A-clusters (21). The EPR spectrum of F229A resembles that of a minority species sometimes observed in WT ACS (22) and of the CO-treated methanogenic ACS (23), which lacks the first 320 amino acids (including F229) of the bacterial enzyme. Recent electron nuclear double resonance (ENDOR) results reveal that the low intensity EPR spectrum of F229A consists of three components including one assigned to a Ni(I) species that lacks CO (16). The NiFeC signal of F229A, like those of WT and F229W, forms during mixing (ca. 30 s) and does not increase with incubation time for up to 1 h.

CO-binding proficiency of the variants was measured by following the increase in intensity of their NiFeC EPR signals at increasing CO concentrations (Fig. 2-4). The F229A variant exhibits at least 30-fold lower (K_D = 340 μM) affinity for CO than WT ACS (K_D = 12.8 μM). At saturating CO levels, F229A also exhibits a NiFeC EPR signal that amounts to only 10 to 20% that of either the WT protein or of F229W.The value for the WT protein matches that measured earlier (23, 24, 25). On the other hand, F229W binds CO too tightly to accurately measure by this EPR-based approach ($K_D << 1$ μM), with a calculated K_D in the pM range, but an unreasonably wide confidence interval (CI).

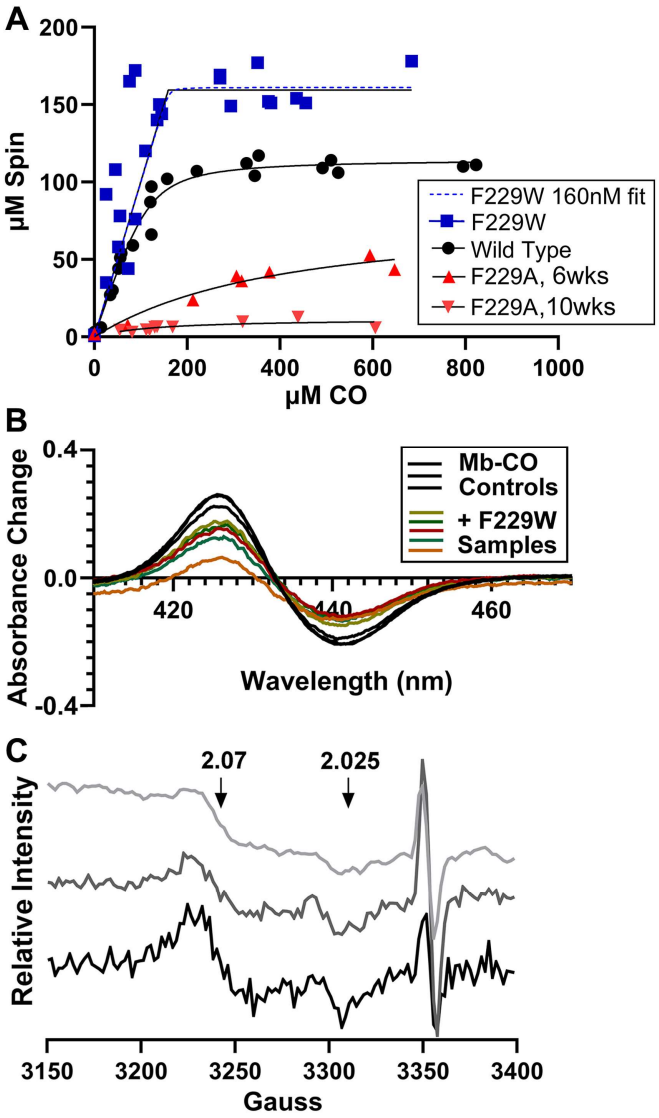

Figure 2-4 Comparison of the CO binding affinity of the alcove variants. *A*, direct CO titration showing individual data points at varying CO concentrations for the ACS variants fit to a quadratic tight-binding equation (see Experimental procedures). EPR samples of ACS were exposed to increased concentration of CO (concentration measured by binding at 424 nm to equine Mb), frozen in liquid N_2, and placed in an EPR cryostat maintained at 100 K for EPR spectroscopy. The spectrum was doubly integrated and spin quantified by comparison to a Cu(II) perchlorate standard. The measured K_D values (and the 95% confidence intervals) were 12.8 µM (7.3–20.2 µM, 95% CI), 0.16 µM (<1 pM-8 µM, 95% CI), and 340 µM (140–940 µM at 95% CI), respectively, for WT, F229W, and F229A. *B* and *C*, anaerobic equilibrium CO competition experiment between F229W and dithionite-reduced (Fe^{2+}) equine myoglobin (Mb). In (*B*), UV-visible spectra of triplicate Mb-CO control samples were determined from a solution of 4 µM Fe^{2+}-Mb reacted with 4.0 µM CO in 50 mM Tris–HCl, pH 7.6 in a 1 cm cuvette at 25 ˚C. For the quintuplicate competition experiments, 4.0 µM CO was added to 4 µM active F229W, sealed with a rubber septum, equilibrated for 5 min, and an initial spectrum was recorded. Then, 4 µM Fe^{2+}-Mb was added, incubated for 30 min, and the equilibrium spectrum was recorded. The difference spectra (Fe^{2+}-Mb-CO minus Fe^{2+}-Mb) are shown. Based on the five UV-visible experiments, the K_D(CO) for F229W was 160 ± 30 nM (95% confidence interval, CI). In (*C*), triplicate EPR experiments were performed in which 200 µl samples were transferred from the UV-visible cuvette to a quartz capillary, quickly frozen in liquid N2, and EPR spectra were run to determine the amount of F229W-CO. Based on the EPR measurements, the average K_D value was 160 ± 90 nM (95% CI). Thus, the three K_D(CO) measurements (from the direct CO binding and CO competition experiments)

reveal a K_D(CO) for the F229W-CO complex between 150 to 190 nM at a 95% confidence level. ACS, acetyl-CoA synthase; CI, confidence interval; EPR, electron paramagnetic resonance.

Because the CI for the K_D(CO) in the direct CO binding experiments (Fig. 2-4*A*) with F229W was so wide, we used an anaerobic equilibrium CO competition experiment between F229W and dithionite-reduced (Fe^{2+}) equine myoglobin (Mb), which exhibits a K_D(CO) of 22 nM (26). In this approach, we added Fe^{2+}-Mb to F229A-CO in the anaerobic chamber, allowed them to reach equilibrium, and measured the initial and final equilibrium amounts of Mb-CO by UV-visible spectroscopy (Fig. 2-4*B*) and F229W-CO by EPR spectroscopy (Fig. 2-4*C*). The three K_D(CO) measurements obtained from the direct CO binding and Mb-CO/F229W-CO competition approaches converge on a K_D(CO) for the F229W-CO complex between 130 to 190 nM at a 95% confidence level. Thus, the Kd(CO) varies over 2125-fold (from 0.160 to 340 μM), depending on the identity of the alcove residue at position 229. To understand how mutation of a second-sphere aromatic residue near Ni_p could disrupt formation of the organometallic Ni_p-CO bond, we performed Ni and Fe K-edge X-ray absorption spectroscopic (XAS) and high-*k* extended X-ray absorption fine structure (EXAFS) experiments for the three variants in the presence and absence of CO and compared the preedge, near, and extended regions of the Ni (Fig. 2-5) and Fe (Fig. S3) absorption edges. Ni- (or Fe-) XAS experiments detect all the Ni (or 4 Fe's) in the sample; thus, this experiment reflects the average Ni_p, Ni_d, and Fe structural and electronic states. Before exposure to CO, each of the variants treated with dithionite display a nearly identical Ni K-preedge features at 8331.7 eV, indicating that their Ni_p (and Ni_d) centers remain unchanged by the F229 substitutions. The differences at higher energies (~8348 eV and higher) between WT and F229W may indicate changes in long-range multiple scattering effect due to the presence of the bulkier tryptophan ligand. Similarly, upon addition of CO to WT ACS or the F229W variant caused a similar decrease in the Ni K rising-edge intensity (indicating tetrahedral geometry at Ni_p), splitting of the Ni K-preedge (electronic structure change at Ni_p upon CO binding) and damping of the EXAFS signal (suggesting elongation of the Ni_p-S bond upon CO binding) as seen earlier for the WT protein (11) (Fig. 2-5). Thus, the F-to-W mutation has little to no effects on structure of Ni(I)-CO.

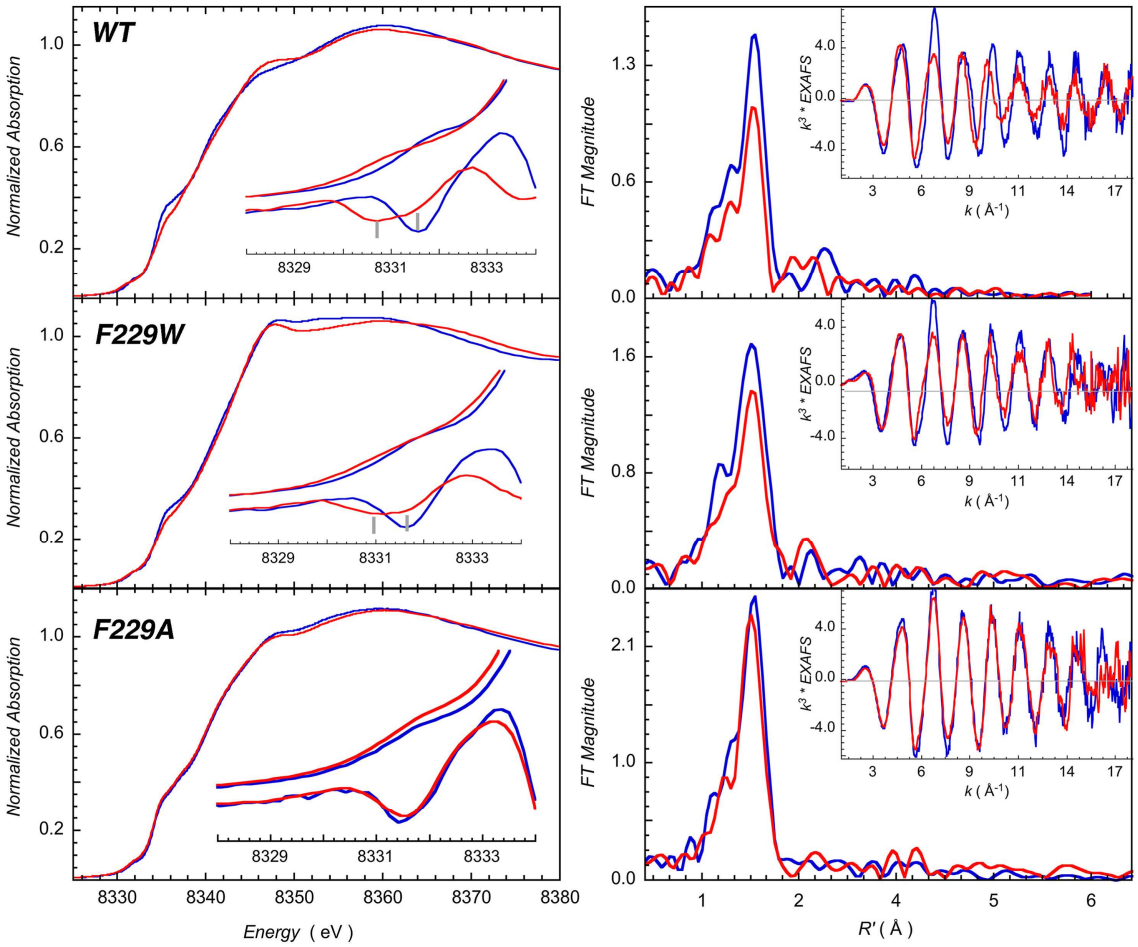

Figure 2-5 **Ni K-edge XAS data showing pre-edge changes on the left and related EXAFS on the right.** *Insets* show shifts in the pre-edge for CO-exposed (*red*) ACS relative to unexposed (*blue*), where the first derivative shows distinct shifts for one of the two A-cluster Ni. Ni K-edge data for F229A does not show a change seen in the WT and F229W. Consistent with these pre-edge data are the EXAFS, which show little to no changes for CO-exposed F229A relative to unexposed. WT data adapted with permission from ref (11). Copyright 2017 American Chemical Society. ACS, Acetyl-CoA synthase; EXAFS, extended X-ray absorption fine structure; XAS, X-ray absorption spectroscopy.

Fig. S3 shows the Fe K-edge XAS data for the WT, F229A, and F229W species (treated with dithionite) before and after exposure to CO. The data unambiguously show no change upon CO binding supporting the assignment of Ni_p as the sole CO binding site in the A-cluster, in accordance with prior XAS (11) and X-ray diffraction (12) studies as well as EPR and FTIR experiments triggered by photolysis (15) and stopped flow (19) instrumentation.

Thus, the similarity of the Ni- and Fe-XAS data for the dithionite-reduced WT and F229 variants, which demonstrate that the A-cluster is properly formed, support the methylation data and the FTIR spectral results (above) indicating that the mutations did not disrupt the overall structure of ACS.

However, for the F229A variant, we observed no significant differences in the Ni K-preedge, rising-edge or in the EXAFS region between the dithionite-reduced and CO-exposed protein (Fig. 2-5). Since CO-incubated F229A variant exhibits an EPR spectrum that shows ^{13}CO splittings (Fig. 2-3*C*), the lack of changes in the Ni-preedge, XAS, or EXAFS on CO exposure likely reflects its four-fold lower CO binding proficiency (above), leaving most of the protein in its resting planar $Ni_p(II)$ state. Similarly, treatment of F229A-ACS with CO does not show differences in the Fe K-edge XAS data (Fig. S3). On the other hand, earlier ENDOR studies, which focus on the EPR-active components of the carbonylation reaction, demonstrated that the remaining paramagnetic Ni in the A-cluster of the F229A variant is composed of is a heterogeneous mixture of species, including a $Ni_p(I)$ species that lacks CO (16).

2.3.2 An intact alcove is required for autotrophic growth by the WLP

The kinetic and spectroscopic results described above suggest that the alcove may be essential for productive CO binding during anaerobic CO_2 fixation. To test the effect of the alcove on growth by the WLP pathway, we chose *C. autoethanogenum* as the host, due to the robust genetic tools available for this acetogen (4) and previous demonstration on mutagenesis and plasmid based complementation of the CODH/ACS complex (27). Following the earlier study where *acsA* had been deleted, we applied the same strategy and successfully deleted the native ACS gene (*acsB)* in the genome of *C. autoethanogenum* and complemented the resulting *C. autoethanogenum* Δ*acsB* strain with both WT *acsB* and well as *acsB* (F209A). Although the *C. autoethanogenum* AcsB enzyme lacks the first 20 AA compared with the *M. thermoacetica* AcsB, the two proteins share 43% identity. The region around F229 of the *M. thermoacetica* enzyme is highly conserved among acetogens and corresponds to F209 of the *C. autoethanogenum* ACS (Fig. 2-6, top). The Δ*acsB* strains carrying the respective plasmids were tested, in biological triplicate, for their ability to grow heterotrophically on fructose and autotrophically on a blend of CO, CO_2, and H_2. All three strains were able to grow heterotrophically but, in the absence of WT *acsB*, strains strikingly did not grow autotrophically (Fig. 2-6, bottom). While the WT *acsB* could complement the genomic deletion in autotrophic growth, the F209A variant was unable to rescue the KO. Thus, *C. autoethanogenum* F209A *(M. thermoacetica* F229A) is unable to grow on syngas ($CO/H_2/CO_2$).

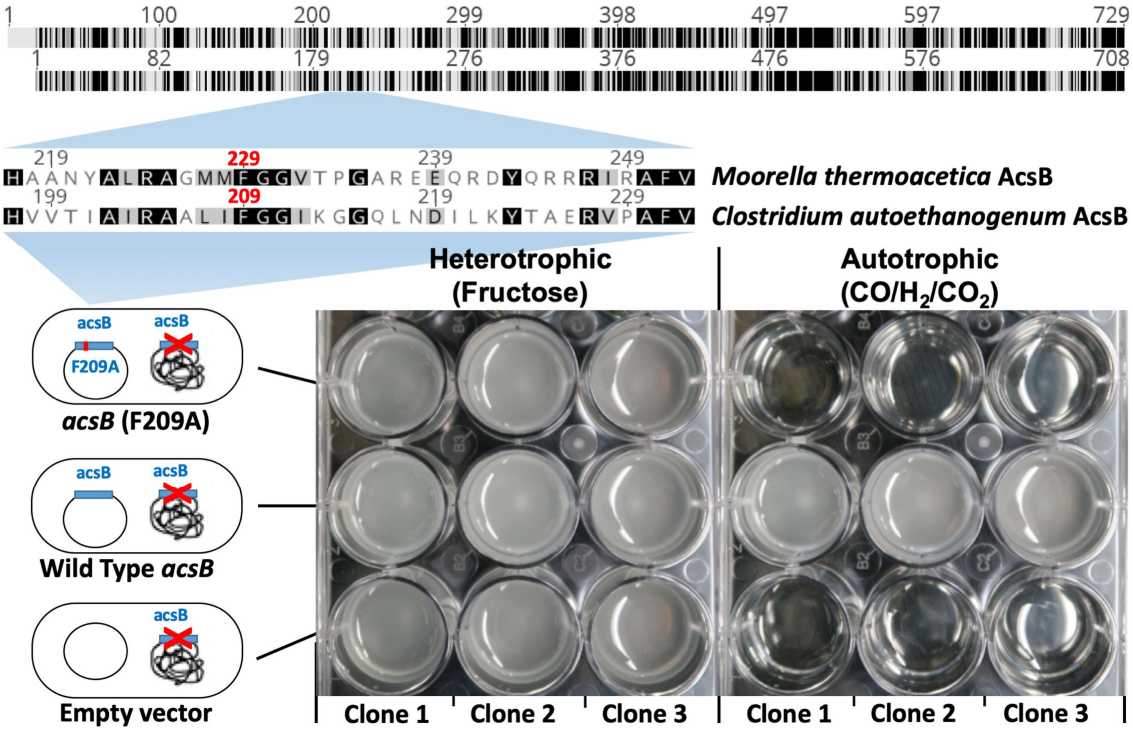

Figure 2-6 **(*Top*) Alignment of AcsB showing highly conserved region around AA position 229 in Moorella thermoacetica and corresponding position 209 in Clostridium *autoethanogenum* (*bottom*) Complementation of *C. autoethanogenum ΔacsB*.** Only wild-type *acsB* but not *acsB*(F209A) is able to restore growth under $CO/H_2/CO_2$ autotrophic conditions. ACS, Acetyl-CoA synthase; AcsB, bacterial ACS.

2.3.3 The alcove is not required for methylation of ACS

The above results suggest that the alcove, which is critical for CO binding and for autotrophic growth by the WLP, plays a significant role in CO access, control, and precise binding to the ACS active site. Crystallographic and electron microscopic data (10, 12, 28, 29) demonstrate that the ACS-CO state exhibits a closed conformation that facilitates CO transport through the tunnel connecting the C-cluster of CODH to the A-cluster, with the alcove residues closing as a hand would grasp a ball and Ni_p adopting a tetrahedral Ni_p(I)-CO coordination geometry (11, 12), as diagrammed in Figure 2-1*B*. However, methyl transfer from methyl-Co(III) to Ni_p requires an open conformation poised for binding the CFeSP and, in this state, the alcove residues (except F512) disperse (12, 13, 29). Thus, the transition between methylation and carbonylation would require alcove formation and dispersal at each catalytic cycle as a hand opens and closes to catch a ball. These major structural changes radiating out from the A-cluster provoke the question, is the alcove required for ACS methylation? Similarly, since the alcove seems to stabilize the open-channel/closed-conformation of ACS to facilitate CO binding, does the F229A substitution facilitate the open (extended) methylation-ready conformation?

The methylation activity of the F229A variant was compared to those of WT and F229W by monitoring decrease in the UV-visible band at 470 nm, associated with methyl-cob(III)inamide (MeCbi) and increase in the Co(I)-cobinamide (Cbi) absorption peak at 390 nm (Figs. 2-7 and S2). We used MeCbi instead of the methylated CFeSP to allow rigorous characterization of the methyl-ACS product, because the CFeSP contains cobalt and an Fe_4S_4-cluster that would obscure any changes in the Fe_4S_4-cluster of ACS that might occur during methyl transfer. MeCbi has been shown to serve as an effective methyl donor to ACS, with a reaction mechanism identical to that with the methylated CFeSP, albeit 100-fold slower than the methylated CFeSP (30).

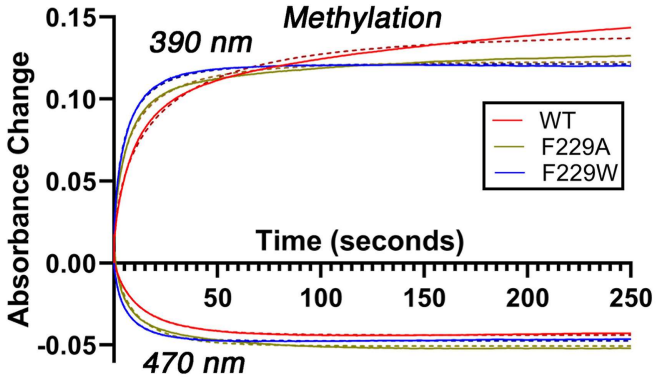

Figure 2-7 **Transient kinetics of methylation of ACS with MeCbi.** Stopped-flow traces of 10 µM ACS reduced with 3x Ti(III) citrate and methylated with 10 µM MeCbi measured by monitoring the time-dependent decrease in absorbance at 470 nm of MeCbi and the increase at 390 nm of Co(I)-Cbi. Data were fit with the equation for a stretched exponential. ACS, acetyl-CoA synthase; MeCbi, methyl-Cbi; Ti(III) citrate, titanium(III) citrate.

All three variants underwent methylation to similar extents (70%) and at similar rates (Table 2-1), indicating that the alcove is not required for methylation of ACS. These activity data also demonstrate that the F229 substitutions have not disrupted the A-cluster, in concurrence with the XAS, backbone FTIR, and metal determination results described above. They also conform with recent electron microscopic studies, which indicate that interactions between Ni_p and methyl-cob(III)inamide occur in an extended conformation (29) *versus* carbonylation which requires a closed state, with F229 and the other alcove residues clustered around Ni_p, and the CO channel, alcove, and Ni_p forming a cohesive unit (Fig. S6).

2.4 Discussion

Much effort has been invested to trap and characterize the proposed organometallic intermediates in the WLP (Fig. 2-1). Now, just as this effort seemed to have come to fruition with characterization of the Ni-CO, Ni-CH_3, and Ni-acetyl intermediates (11, 12, 13), we reveal here

that we must broaden our metal-centric view of the active site of ACS. Here, we rigorously and quantitatively demonstrate that the Ni_p center in the A-cluster that forms the organometallic bonds, has insufficient affinity to bind CO at the low micromolar levels required for enzymatic catalysis and autotrophic (H_2/CO_2) growth. The ACS active site requires augmentation by an alcove consisting of five highly conserved hydrophobic amino acid residues, which form an alcove connected directly to the A-cluster and the gas tunnel. A Xe-pressurized structure of CODH/ACS (10), provided a glance at the alcove. This structure revealed a xenon atom cradled in a hydrophobic basket of residues between Ni_p of the A-cluster on one side and the CO tunnel on the other (Fig. 2-2). A structure-function relationship and the term “alcove” were proposed in an article describing a very low barrier for substrate CO to rebind to Ni_p after photolytic dissociation (15). Here, we reveal that the alcove is required for productive binding of substrate CO during anaerobic carbon fixation by the WLP. *In vitro* and *in vivo* experiments reveal that substitution of the bulky benzene group of Phe229 at one wall by the small methyl group of Ala decreases CO affinity thirty-fold and abolishes autotrophic growth by the WLP. However, the F229A variant is otherwise competent for A-cluster assembly and reaction with the methyl donor. Since disrupting Ni-CO formation obstructs the WLP, is it possible that enhancing CO binding could improve the pathway? Replacement of the benzene group of F229 with the larger indole of Trp enhances CO affinity 80-fold without affecting methyltransferase activity. Our work redefines what we historically refer to as the metallocenter "active site". Thus, as serine proteases like carboxypeptidase lack biological function without an intact tripartite active site consisting of a catalytic triad (Ser195, Asp102, and His57), an electropositive oxyanion hole (the backbone NHs of Gly193 and Ser195), and a polypeptide substrate recognition/binding site (31), the A-cluster alone is not a productive catalyst and requires several key functions of the alcove for concentrating and directing CO to the metallocofactor and preventing CO loss and inhibition. As ACS contains a tunnel that, like in methane monooxygenase (32), serves as an extension of the active site, we propose that the alcove should be considered part of the ACS active site and suggest that the community seek similar alcoves in the active site of other gas-handling enzymes, *e.g.*, formate dehydrogenase, hydrogenase, and nitrogenase.

We propose several potential mechanistic roles for the alcove (Fig. 2-8). One is to enhance CO binding by increasing the local CO concentration near Ni_p of the A-cluster

(Fig. 2, *B* and *C*). The inherent CO affinity of the A-cluster ($K_D \geq 340$ μM), based on the value for the F229A variant. This is consistent with weak CO binding to a Ni(I)-cyclam ($K_D = 30$ μM) (33) and a Ni-substituted M121A azurin variant ($K_D = 1$ mM) (34). However, its CO-binding affinity can be tuned at least 2000-fold by site-specific substitutions of a single alcove residue (F229) without affecting other steps in the catalytic mechanism. While anaerobic microbes evolved this mechanism to enhance CO binding by ACS, aerobic organisms positioned distal residues in O_2-binding proteins, *e.g.* Mb and hemoglobin, to sterically lower their CO affinity, relative to that of the heme metallocofactor, to protect against CO toxicity (35).

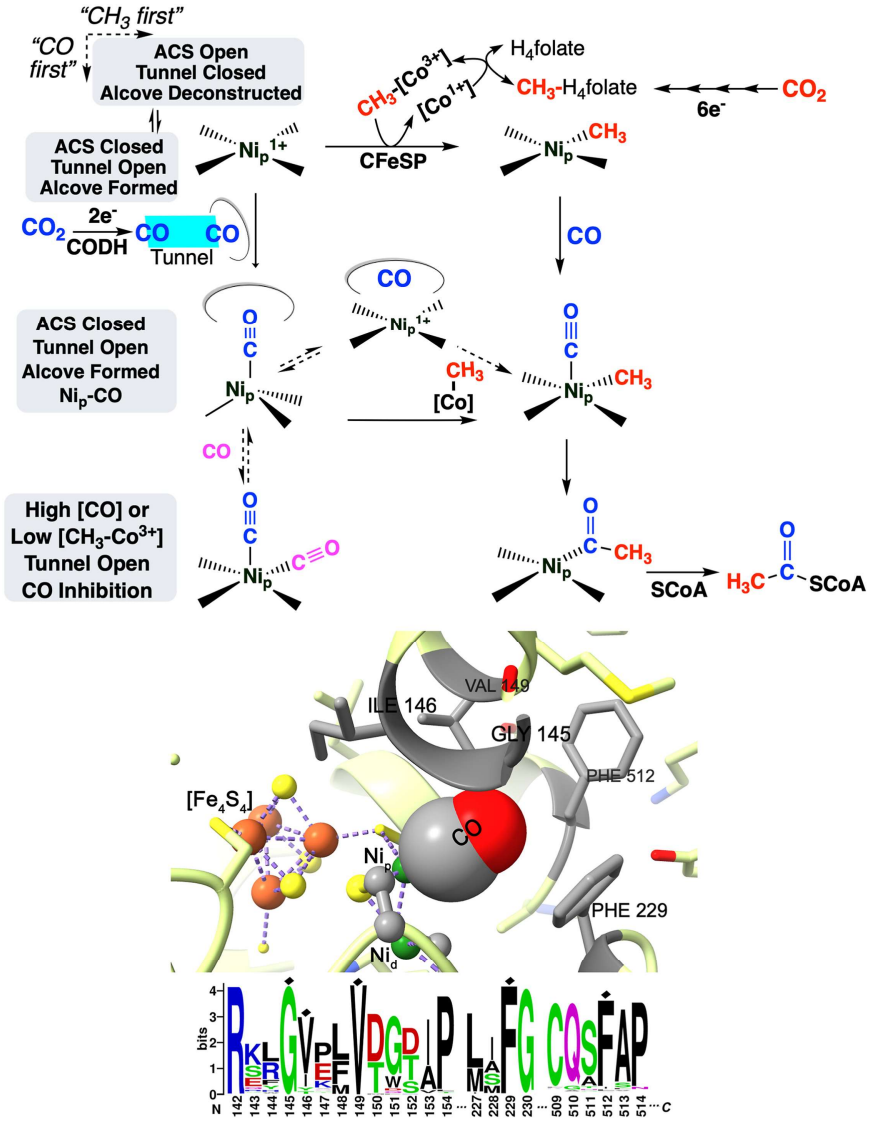

Figure 2-8 **Alcove requirement for ACS catalysis.** (*Top*), the alcove integrated on one side with Ni_p and the A-cluster metallocofactor as the ACS active site and on the other with the tunnel, serving as an extension of the active site. The alcove significantly lowers the K_s for CO. The directing actions of the tunnel combined with the concentrating and protective effects of the alcove near Ni_p, prevents CO loss and inhibition, ensuring ACS can

randomly bind either substrate (CO or methyl) at the low CO concentrations required for autotrophic growth. See the text for details. (*Bottom*), conserved sequences containing the five alcove residues. A blast search and multiple sequence alignments were performed of 5000 prokaryotic genomes (excluding archaea) against the *Moorella thermoacetica* ACS (AcsB) sequence (mta_Moth_1202, (55). Sixty amino acids were then loaded into the Weblogo program (56) to visualize the 27 to 28 amino acids with the highest conservation in each of the three Alcove sequence motifs. ACS, acetyl-CoA synthase; AcsB, bacterial ACS.

Other likely roles of the alcove are to protect ACS from loss of CO and to stabilize the changes in metallocenter ligation (tetrahedral Ni(I)-CO, planar Ni-CH_3, and planar Ni-acetyl) and overall protein conformation (closed, open, extended, and hyperextended (29)), that it transits during catalysis. Thus, it needs a flexible ligand system that can stabilize both CO- and Me-ACS bound intermediates, including the proposed pentacoordinate methyl-Ni-CO that would undergo CO insertion to generate the Ni-acetyl state (Fig. 2-8). Having an alcove at the interface of Ni_p and the gas tunnel may prevent CO depletion, which would be devastating for autotrophic growth by the WLP, given the significant energy expenditure of acetogens to accomplish the thermodynamically demanding CODH-catalyzed reduction of CO_2 to CO (E_o' = −540 mV). The inability of F209A to grow autotrophically likely results partly from loss of CO from the active site during acetyl-CoA synthesis. ENDOR and EPR studies indicate that F229A binds CO both weakly and haphazardly with CO migrating between the CO and methyl binding sites (16). We envision the alcove grasping CO as it leaves the gas tunnel and approaches Ni_p of the A-cluster, as our hands grasp a baseball.

Another role for the alcove highlighted in Figure 2-8 is to protect ACS from CO inhibition. There has been much discussion about whether methyl and CO bind randomly, or sequentially with methylation occurring first, followed by ordered binding of CoA to the acetyl-Ni species. The random mechanism is supported by pulse-chase experiments in which $^{14}CO_2$ incorporation into acetyl-CoA was unaffected by the presence of ^{12}CO in solution and $^{14}CH_3$ incorporation was unaffected by increasing levels of $^{12}CH_3$-Co(III), with strictly ordered binding of CoA (14). Similarly, stopped-flow and freeze quench EPR experiments demonstrate that either methylation or carbonylation to form the methyl-Ni or Ni-CO intermediates at rates faster than the overall steady-state rate of acetyl-CoA synthesis (19, 20). Furthermore, recent XAS and X-ray crystallographic studies have revealed these organometallic Ni(I)-CO, methyl-Ni, and acetyl-Ni complexes (11, 12, 13). On the other hand, evidence supporting an ordered mechanism includes the finding that high CO concentrations can competitively inhibit methylation (23, 36, 37, 38), leading some to propose that the ACS

mechanism is strictly ordered with methylation occurring first. Our work resolves these divergent viewpoints and apparent contradictions because the potentially inhibitory CO can escape into the alcove and rebind to Ni_p with a nearly barrier-less activation energy of <1 kJ/mol (15). If indeed the organometallic mechanism on Ni_p does requires methylation to occur first, when the wrong substrate (CO) binds, the ACS mechanism would still accommodate random substrate binding in which the alcove would provide a temporary harbor for CO, allowing formation of methyl-Ni and then rebinding of CO to form acetyl-Ni.

As shown in Figure 2-8, this process is exquisitely orchestrated. Prior crystallographic and electron microscopic studies (29) indicating large conformational changes associated with opening and closing of the A-cluster domain of ACS at each catalytic cycle. Based on their location in this domain, the five alcove residues would close like the fingers of a hand around incoming CO as it grasps a ball, holding it near Ni_p and enhancing formation of the tetrahedral Ni-CO species. They would open to allow Ni_p to bind methyl-Cob(III) (and the CFeSP). Then, to bind CO, they approach in unison like the fingers of a hand as it grasps a ball, holding it near the axial position at Ni_p for precise delivery in a *cis* position to the methyl-Ni-CO complex. This sequence of events would be reversed for the "methyl-first" scenario, but in either case, carbonyl insertion would form the planar acetyl-Ni_p for reaction with CoA to generate acetyl-CoA.

CO binding is rate limiting in the ACS mechanism and in the WLP; ACS methylation and CoA thiolysis of Ni-acetyl to form acetyl-CoA occur 10- and 100-fold faster (9, 20, 39). Thus, our demonstration that disruption of Ni-CO formation obstructs the WLP suggests that enhancing CO binding (as per the F229W mutation) or delivery through the gas tunnel, could improve the pathway. These strategies are not only important for understanding mechanistic features of this remarkable pathway but suggest opportunities to boost CO_2 capture and utilization for the benefit of the climate and biotechnology.

Related to CO inhibition, while all alcove residues are highly conserved among bacteria that use the WLP, the homologous CdhC subunit of the methanogenic ACS lacks the N-terminal domain of the bacterial ACS (AcsB). This domain contains four of the five alcove residues and participates in the conformational change that allows interaction with the CFeSP. Mutation of Phe195 (F512 in *M. thermoacetica*), the only alcove residue present in the homologous methanogenic subunit, lowers affinity of AcsB for methyl-Co(III) and enhances CO inhibition of acetyl-CoA synthesis apparently by competing with methylation (23). Thus, either

the methanogens do not use an alcove and avoid the striking conformational changes observed in the bacterial ACS (29) or, as others have suggested (40, 41), another subunit of the methanogenic enzyme complex provides these functions. We eagerly await a structure of this five-subunit complex to understand the molecular dynamics and architecture underlying acetyl-CoA synthesis and utilization in methanogens.

In a nutshell, this work reveals how an alcove augments and tunes the inherent gas-binding properties of a metallocofactor, indicates ways to enhance the metabolism of gaseous substrates, and prompts researchers to look for alcoves in other gas-handling proteins that could be considered part of the metalloenzyme active site.

2.5 Experimental procedures

2.5.1 Generation of monofunctional ACS alcove variants

A pET29 vector (Kan^R, His6-tagged, *lac*-inducible) harboring the *M. thermoacetica acsB* gene containing the ACS subunit of CODH/ACS, known as $pET29ACSMT_{HT}$ was used as a basis for generation of ACS phenylalanine-229 variants. ACS variants F229A and F229W were generated with a QuikChange II site-directed mutagenesis kit from Agilent Technologies using primers (Integrated DNA Technologies) containing the sequences for F229W and F229A, respectively: F229W-*sense* 5′- C CTG CGG GCT GGT ATG ATG TGG GGT -3′ *antisense* 5′- GT AAC GCC ACC CCA CAT CAT ACC AGC -3’; F229A-*sense* 5′- G CGG GCT GGT ATG ATG GCC GGT GGC -3′ *antisense* 5′- GGT AAC GCC ACC GGC CAT CAT ACC A -3’. WT ACS was left unadulterated. The ACS variant plasmids were, respectively, transformed into competent BL21(DE3) *Escherichia coli* cells along with the pBD1282 plasmid (Amp^R, *ara*-inducible) containing the genes *iscS-iscU-iscA-hscB-hscA-fdx* from Azotobacter vinlandii for proper [Fe_4S_4] construction (14).

2.5.2 Growth of C. autoethanogenum

Growth of *C. autoethanogenum* was carried out under strictly anaerobic conditions as described earlier using a modified version of ATCC medium 1754 with yeast extract and fructose omitted (42) and a derivative strain (43) of *C. autoethanogenum* type strain DSM10061 obtained from DSMZ (Deutsche Sammlung von Mikroorganismen und Zellkulturen). When noted, 10 g L^{-1} of fructose was added to the medium. For plasmid maintenance, thiamphenicol was added to a concentration of 15 mg L^{-1}. Tests for autotrophic

and heterotrophic growth were performed in 12-well round-well plates with each well containing 2 ml of growth medium. Wells were inoculated in a glovebox (Inert) with a N_2 atmosphere, then the plates were placed in custom pressure-rated stainless-steel jars. For each genotype, we tested three biological replicates. The headspace of the jar was replaced with 170 kPa (gauge) of a synthetic $CO/CO_2/H_2/N_2$ (50%/30%/10%/10%) gas blend (Airgas) for autotrophic growth conditions and left with ambient pressure of N_2 (Airgas) for heterotrophic growth on fructose. Jars were shaken at 90 rpm with a 2.5 cm throw and incubated at 37 °C for growth.

2.5.3 Genetic modification of C. autoethanogenum

Homologous recombination, with counter selection, facilitated deletion of *acsB* in *C. autoethanogenum* with target-specific modifications from the method previously described (44). Namely, we amplified homology arms from genomic DNA with the oligonucleotides listed in Table S2 and used TCACCAAATGTCATTCCAAG as the recognition sequence for the guide RNA. The vector was assembled with the GeneArt Seamless Cloning kit (Thermo Fisher Scientific). We included fructose in the medium during deletion of *acsB* since we anticipated the essentiality of the gene for autotrophic growth. For expression of *acsB*, we amplified the gene from genomic DNA and cloned it into pMTL83151-P_{acsA} (27) using oligonucleotides listed in Table S2. We created the F209A substitution using the kinase, ligase, and DpnI (KLD enzyme mix) kit (New England Biolabs) with oligonucleotides listed in Table S2.

2.5.4 Expression and purification of monofunctional ACS variants in competent E. coli cells

Growth of *E. coli* cells harboring the ACS variant plasmids was conducted as previously described (14). Lysis and purification of ACS and variants were performed as previously described with protein concentrations verified by the Rose Bengal assay (45). All buffers and reagents were prepared under strict anaerobic conditions (≤2.5 ppm O_2), and all glassware used in purification was acid washed for no less than 1 h to remove any metal contaminants.

Metal reconstitution of pure ACS was performed as described previously (46). ACS metal content post reconstitution is quantified by inductively coupled plasma optical emission spectroscopy through the Center for Applied Isotope Studies at the University of Georgia (Athens, GA) in comparison to the protein concentration verification by the Rose Bengal assay (45).

2.5.5 EPR analysis of natural abundance and isotopically labeled ACS-CO variants

Continuous-wave X-band EPR data were collected on a Bruker EMX equipped using a variable-temperature ColdEdge liquid helium condensing unit with a MercuryiTC cryostat by Oxford Instruments. All spectra were collected using the WinEPR software package (https://www.bruker.com/en/products-and-solutions/mr/epr-instruments/epr-software/winepr.html). EPR samples were prepared as previously described (21) by anaerobic mixing of ACS in 50 mM potassium phosphate pH 7.5 with 2 mM sodium dithionite, transferred to an EPR tube capped with a rubber septum, and purged with 100% carbon monoxide gas (ultra-high purity; Cryogenic Gases) for 25 min before being flash frozen in liquid nitrogen. Protein concentration was assessed in parallel by the Rose Bengal assay (45). Isotopically labeled ACS variants were treated as previous CO samples, but purge time was reduced to 10 min to minimize wasted ^{13}CO gas. All samples were stored at −80 ˚C prior to spectrum acquisition. Natural abundance (NA) WT and F229W EPR spectra were collected at 40 K with a power of 20.8 mW, a modulation frequency of 100 kHz, a modulation amplitude of 10 G, gain of 2000, conversion time of 81.92 ms, and a time constant of 40.96 ms. NA F229A EPR spectrum was collected at 100 K with a power of 20.8 mW, a modulation frequency of 100 kHz, a modulation amplitude of 10 G, gain of 4480, conversion time of 40.96 ms, and a time constant of 20.48 ms. ^{13}CO WT EPR spectrum was collected at 100 K with a power of 2.08 mW, with a modulation frequency of 100 kHz, a modulation amplitude of 10 G, gain of 4480, conversion time of 163.84 ms, and a time constant of 40.96 ms. The ^{13}CO F229W and F229A spectra were collected at 100 K with a power of 20.8 mW, modulation frequency of 100 kHz, a modulation amplitude of 10 G, gain of 4480, conversion time of 40.96 ms, and a time constant of 20.48 ms. Analysis of EPR spectra was conducted using the WinEPR software package, and the resultant ACS spectra were quantitatively measured by comparison to a 1 mM Cu(II) perchlorate standard using the equation from Fee, 1978 (47).

For spin quantification by EPR, an initial 10 mM Cu(II) perchlorate standard stock was prepared for spin quantitation by mixing together 12.24 g sodium perchlorate (Sigma-Aldrich), 0.125 g Cu(II) sulfate pentahydrate (99.999% purity; Sigma-Aldrich), and 42 µl saturated (12 M) HCl with ultrapure water to a final volume of 50 ml. Subsequently, 10 mM Cu(II) perchlorate stock was diluted by 10 to 1 mM standard with high purity water, where a 200 µl aliquot is transferred to an EPR tube and frozen with liquid N_2.

2.5.6 CO titration of ACS WT and variants monitored by EPR

The headspace of the protein samples in 50 mM Tris, pH 7.6 with 20% glycerol and 5 mM dithionite (concentration measured by Rose-Bengal assay) were exchanged for varied lengths of time (from 15 s to 10 min) with a 5% CO/N_2 gas mix and 100% CO gas to achieve wide-ranging CO concentrations. The final CO concentrations were measured by CO binding to equine Mb at 424 nm, prior to flash-freezing. All samples were stored at −80 °C prior to acquisition. The continuous-wave X-band EPR data were acquired on a Bruker EMX equipped with a liquid nitrogen cryostat. All spectra were collected using WinEPR Acquisition software. WT spectra were collected at 100K with a single scan at a power of 0.644 mW, a modulation frequency of 100 kHz, a modulation amplitude of 5 G, gain of 1 x 10^5, conversion time of 163.84 ms, and a time constant of 81.92 ms. F229W spectra were collected at 100K with a single scan at a power of 0.644 mW, a modulation frequency of 100 kHz, a modulation amplitude of 5 G, gain of 1 x 10^5, conversion time of 81.92 ms, and a time constant of 81.92 ms. F229A spectra were collected at 100K with four scans at a power of 0.644 mW, a modulation frequency of 100 kHz, a modulation amplitude of 5 G, gain of 1 x 10^5, conversion time of 81.92 ms, and a time constant of 81.82 ms. Analysis of EPR spectra was conducted using WinEPR Processing software, and the resultant ACS spectra were quantitatively measured by comparison to a 1 mM Cu(II) perchlorate standard using the equation from Fee, 1978 (47). The quantified spin percentages were plotted against the concentration of CO for each sample. Since the enzyme concentration is greater than the calculated KD for each of the variants, the free-ligand assumption for a simple binding isotherm does not apply; the data were fitted to the quadratic tight-binding equation (Equation 2-1) to reveal average K_D values (with 95% *CIs*) of 12.8 μM (7.3–20.2 μM), <1 PM (<1 pM-8 μM), and 340 μM (140–940 μM), respectively, for WT, F229W, and F229A.

$$y = \frac{(E_T + x + K_D) - \sqrt{(E_T + x + K_D)^2 - 4 * E_T * x}}{2} \qquad \text{(Equation 2-1)}$$

where x = [CO] (uM)

2.5.6.1 CO competition assays with equine Mb

Because the direct CO binding experiments (Fig. 4*A*) returned such wide CIs of the K_D(CO) for F229W, scaling orders of magnitude, we used anaerobic equilibrium CO competition experiments between F229W and dithionite-reduced (Fe^{2+}) equine Mb, which exhibits a K_D(CO) of 22 nM (26). The titrations were measured by UV-visible and EPR spectroscopy.

2.5.6.2 UV-visible measurement of Mb-CO

The competition experiment was performed in the anaerobic chamber (<1 ppm O_2) using stock solutions of 800 μM equine Fe^{2+}-Mb (Sigma-Aldrich, EC 309-705-0) reduced with 500 mM dithionite; 77 μM active A-cluster of F229W (from 336 μM F229W, measured by EPR as the Ni(I)-CO complex with saturating CO); and CO (1140 μM). All stock solutions were prepared in 50 mM Tris–HCl, pH 7.6. For the triplicate Mb-CO control samples, Fe^{2+}-Mb (7.5 μl, 4 μM, final) was added anaerobically *via* a 10 μl Hamilton syringe to 1187 μl of buffer (50 mM Tris–HCl, pH 7.6) and the cuvette was sealed with a rubber sleeve stopper. The initial spectrum of reduced Fe^{2+}-Mb was recorded; then CO (5.3 μl, 4.0 μM, final) was added to make Mb-CO. The difference spectrum (*i.e.*, the spectrum of reduced Fe^{2+}-Mb-CO minus from Fe^{2+}-Mb)_represents the maximum Mb-CO and was used to calculate the fraction of Mb-CO during the equilibrium experiment with ACS. For the quintuplicate competition experiments, F229W (78 μl, 4 μM active A-cluster, final) was added to 1402 μl buffer in a 1 cm path-length cuvette, sealed with a rubber sleeve stopper; then CO (5.3 μl, 4 μM) was added and equilibrated for 5 min before recording an initial spectrum. Then Mb (7.5 μl, 4 μM) was added and incubated for 30 min before recording the equilibrium spectrum. Some samples were remeasured after 24 h, and we saw no further spectral changes. All spectra were adjusted for dilution to a final volume of 1500 μl. The initial CO-F229W spectrum was subtracted from the equilibrium spectrum to isolate the absorbance from Mb during competition with F229W. The 4 μM reduced Mb spectrum was subtracted from the equilibrium competition Mb spectrum to quantify the amount of Mb-CO at equilibrium. The fraction of Mb-CO (f_{myo}) during competition with F229W was compared to the Mb-CO controls and Equation 2-2 was used to calculate the apparent K_D for CO binding to F229W-ACS, where the $K_{D,myo}$ (K_D(CO) for equine Mb-CO) is 22 nM (26), [CO] is 4 μM, and f_{myo} is the fraction of Mb bound by CO. Based on the five UV-visible experiments, the K_D(CO) for F229W was 160 ± 30 nM (95% CI).

$$K_{D,F229W} = \frac{K_{D,myo} * [CO]}{f_{myo} - K_{D,F229W}}$$

2.5.6.3 EPR measurement of F229W-CO

The amount of F229W-CO was determined in triplicate equilibrium binding EPR experiments in which 200 µl samples were transferred from the cuvette to a quartz capillary and quickly frozen (30 s). The EPR samples (four scans) were run at 15 K, 0.4 mW power, 10 G modulation amplitude, 9.372 GHz frequency. Two of the three samples had a measurable A-cluster signal which was quantified against a 1 mM Cu perchlorate standard. For the third sample, the anaerobic syringe became clogged, and we reverted to a micropipette, which may have led to CO loss during the transfer, causing the signal to be too low to accurately quantify above the noise. For the other two samples, the µM spin was used to calculate f_{myo}, and Equation 1 was used to calculate the apparent K_D for CO binding to F229W. The relevant parameters for sample 4 were 0.86 µM spin giving f_{myo} = 0.79 and a 115 nM K_D for F229W-CO (the UV-visible had 2.5 µM CO and an f_{myo} = 0.63; for sample 5 were spin = 2.18 µM giving f_{myo} = 0.46 leading to a 203 nM K_D for F229W-CO (the UV-visible had 2.3 µM CO and an f_{myo} = 0.57). Thus, based on EPR measurements, the average K_D value was 160 ± 90 nM (95% CI). Because of the signal/noise of the tiny EPR signals, there was a larger 95% CI; furthermore, there were two EPR samples compared to five UV-visible experiments. Regardless, the f_{myo} between the EPR and UV-visible results is within the random error associated with the EPR measurements. Finally, to compare the equilibrium binding results to those obtained from the direct CO titrations, the quadratic fit of the direct CO titration data using a K_D of 160 nM (Fig. 2-4*A*, dotted line) returned a similar R^2 as that for the unconstrained fit (K_D of 1 pM, solid line) with an unreasonably high CI.

Thus, the three K_D(CO) measurements (from the direct CO binding and CO competition experiments) are consistent with a K_D(CO) for the F229W-CO complex between 130 to 190 nM at a 95% confidence level, which demonstrates a CO affinity 80-fold higher than WT F229 and 2125-fold higher than F229A.

2.5.7 XAS measurements

XAS spectra were measured at the Stanford Synchrotron Radiation Lightsource on the focused 16-pole, 2 T wiggler side-station beam line 9-3 under standard ring conditions of 3 GeV and ~500 mA. A Si(220) double crystal monochromator was used for energy selection. A Rh-coated harmonic rejection mirror was used to reject components of higher harmonics. During data collection, the samples were maintained at a constant temperature of ~10 K using an Oxford Instruments CF 1208 liquid helium cryostat. A 100-element Ge monolith fluorescence detector from Canberra Industries was used for fluorescence data measurement.

2.5.7.1 Fe K-edge measurements

Fe K-edge XAS data were measured on the dithionite reduced (ACS_{red}) and dithionite reduced followed by CO exposure (ACS_{red}-CO) in the fluorescence mode by using soller-slits equipped with Mn-filter in front of the Ge detector and using an Fe-foil for energy calibration. The first inflection point of the foil spectrum was fixed at 7111.2 eV. The samples were monitored for photoreduction and showed no signs of change during data collection. Fe K-edge EXAFS data were measured up to $k = 15$ Å^{-1}. The data presented here are 8-scan (WT) and 4-scan (variants) average spectra, collected over four fresh-sample positions for each of the samples.

2.5.7.2 Ni K-edge measurements

Ni K-edge XAS data were measured in fluorescence mode by using soller-slits equipped with Co-filter in front of the Ge detector and using a Ni-foil for energy calibration. The first inflection point of the foil spectrum was fixed at 8331.6 eV. The samples were monitored for photoreduction and no sign of photodamage or Ni-CO bond-cleavage was observed during the course of data collection. Ni K-edge EXAFS data were measured up to $k = 18$ Å^{-1}. The data presented here are 12-scan (WT) and 9-scan (variants) average spectra, collected over four fresh-sample positions for each of the samples.

2.5.7.3 XAS data reduction

Data presented in this study were processed by fitting a second-order polynomial to the preedge region and subtracting this from the entire spectrum as background in PySpline (48). A four-region spline of orders 2, 3, 3, and 3 was used for both the Ni and Fe datasets to model the smoothly decaying postedge region. Theoretical Ni K-edge EXAFS signals $\chi(k)$ were calculated by using *FEFF* (macintosh version 7) (49, 50) on the active site structure derived from the

crystal structure of ACS (pdb = 1RU3). Structural models were generated for the different putative forms of Ni_p and Ni_d sites. The molecule editing software Avogadro (51) was used to modify the structural parameters obtained from the crystal structure. Theoretical models were fit to the data using EXAFSPAK (52). The structural parameters varied during the fitting process were the bond distance (R) and bond-variance σ^2, which is related to the Debye-Waller factor resulting from thermal motion, and static disorder of the absorbing and scattering atoms. The nonstructural parameter ΔE_0 (the energy at which $k = 0$) was also allowed to vary but was restricted to a common value for every component in a given fit. Coordination numbers were systematically varied in the course of the fit but were fixed within a given fit.

2.5.7.4 XAS sample preparation

XAS samples of the F229W and F229A variants of activated ACS were prepared as previously described (11): two protein states were prepared for each; ACS_{red} and ACS_{red}-CO. ACS_{red} was the protein reduced with 2 mM sodium dithionite, while ACS_{red}-CO was similarly reduced and then purged with pure CO for 10 min in a sealed and crimped vial. Final variant concentration was 1 mM after addition of 30% glycerol as a glassing agent in 50 mM potassium phosphate, pH 7.5, and protein concentration was verified by the Rose Bengal assay (45). Variant samples were quickly placed in XAS sample cells, removed from the anaerobic chamber, flash frozen in liquid nitrogen, and shipped overnight to the Stanford Synchrotron Radiation Lightsource for data acquisition and analysis.

2.5.8 FTIR sample preparation

FTIR ACS variant samples were prepared by buffer exchange of variants into 50 mM potassium phosphate in D_2O, pH 7.7, then concentration of the variants to an expected 1 mM using ultracentrifugal filters with a 30 kDa cutoff membrane, spun in a tabletop centrifuge at 10,000 rpm for 4 min. Concentrated ACS samples were purged with pure CO gas for 10 min in stoppered and crimped 2 ml vials, where the final ACS concentration was assessed by the Rose Bengal assay (45). After CO purging, the samples were transported in airtight containers to a collaborator's anaerobic chamber, where the samples were transferred to a CaF_2 FTIR sample window. Once in the FTIR window, the sample was removed from the chamber and the IR spectrum taken immediately (JASCO FT/IR-4600) compared to a D_2O buffer blank.

2.5.9 Methylation of WT and variant ACS

Methylation of ACS variants was performed in darkness with red light by Stopped-Flow UV-visible spectrophotometry (Applied Photophysics SX20; single-wavelength monochromator), using MeCbi as a methyl donor, and titanium(III) citrate (Ti(III)) citrate as a reducing agent. A reaction solution consisting of 10 μM ACS and 30 μM Ti(III) citrate was prepared in 50 mM potassium phosphate, pH 7.5. Reaction solutions containing ACS were blanked, and the experiment began with addition of 10 μM MeCbi. Resultant spectral changes associated with Cbi ligand changes and redox shift from 3+ to 1+ state and were quantified using the change in extinction coefficient at 390 nm ($\Delta\varepsilon_{390}$ = 17 mM^{-1} cm^{-1}), *i.e.*, for methyl-Cob(III)inamide, $\varepsilon_{390,MeCbi}$ = 8 mM^{-1} cm^{-1} and for Cob(I)inamide $\varepsilon_{390,Co(I)bi}$ = 25 mM^{-1} cm^{-1}. The spectral changes were also quantified at 470 nm ($\varepsilon_{470,MeCbi}$ = 11 mM^{-1} cm^{-1}; $\varepsilon_{470,Co(I)bi}$ = 3 mM^{-1} cm^{-1}; $\Delta\varepsilon_{470}$ = 8 mM^{-1} cm^{-1}).

Calculation of percentages associated with methylation of ACS was performed using the following equation:

$$Conversion_{390}\% = \left(\frac{\frac{Abs_{390} - Abs_{o,390}}{(\varepsilon_{CO(I)} - \varepsilon_{MeCo(III)})} * 1000 * \frac{\mu M}{mM}}{[MeCo(III)binamide]_o} \right) * 100$$

2.5.10 Preparation of MeCbi and TI(III) citrate reductant

MeCbi was prepared as described (53) with an anaerobic 40% methyl iodide/60% methanol solution prepared on ice by blowing high purity nitrogen over the mixture for 5 min. Once the 40% methyl iodide/methanol solution is prepared, the MeCbi is made anaerobically by mixing 1x (mol/mol) dicyano-Cbi (≥93%; Sigma-Aldrich) with 6x (mol/mol) Ti(III) citrate in a brown glass vial. The vial is then stoppered with rubber septum, and 240x (mol/mol) of the previously prepared 40% methyl iodide/methanol solution is added and left to react at room temperature for ≥ 2 h. After reacting, the solution is then purified *via* size-exclusion with 50 mM potassium phosphate buffer, pH 7.5 under green light by an anaerobic Bio-Gel P2 (Bio-Rad; 100–1800 MW cutoff) and collected in 0.5 ml aliquots and checked for purity *via* UV-visible spectroscopy using ε_{390} = 8 mM^{-1} cm^{-1} and ε_{470} = 10.8 mM^{-1} cm^{-1}. Pure and concentrated MeCbi aliquots are pooled, quantified, and stored at −20 ˚C.

Ti(III) citrate (83 mM stock) reductant was prepared anaerobically as previously described (54). Ti(III) citrate solutions were stored anaerobically at room temperature away from light in a brown glass vial.

Note: The supplemental information (SI) for this publication is available at https://doi-org.proxy.lib.umich.edu/10.1016/j.jbc.2024.107503

2.6 Attributions

Seth Wiley [1], Claire Griffith [1], Peter Eckert [2], Alexander P. Mueller [3], Robert Nogle [3], Séan D. Simpson [3], Michael Köpke [3], Mehmet Can [1], Ritimukta Sarangi [4], Kevin Kubarych [2], Stephen W. Ragsdale [1]

[1]Department of Biological Chemistry, University of Michigan, Ann Arbor, Michigan, USA

[2]Department of Chemistry, University of Michigan, Ann Arbor, Michigan, USA

[3]LanzaTech Inc, Skokie, Illinois, USA

[4]Stanford Synchrotron Radiation Lightsource, SLAC National Accelerator Laboratory, Menlo Park, California, USA

2.7 Author Contributions

As second author on this article, I determined the Kd for CO binding to wild type ACS and both mutants, F229A and F229W by an EPR titration after testing and troubleshooting a variety of other methods. I also performed and analyzed the myoglobin/F229W competition experiments to further narrow the estimate of the F229W Kd for CO binding. I wrote the methods sections related to my experiments, added my data to the results, made figures related to this data and participated in the review process.

2.8 Acknowledgements

We are grateful for the contributions of Stephen Gonzalez during his NSF REU research on mechanistic studies of ACS. We thank Adam Thompson, Bethany Regnerus, Shivani Garg, and Steven D. Brown for their support and conversations about this work.

2.9 Conflict of interest

A. P. M., R. N., S. D. S, M. K. are employees of LanzaTech that has commercial interest in gas fermentation. All other authors declare no conflict of interest with the contents of this article.

2.10 References for Chapter 2

1. Rabiu, K. O., Han, L., and Bhusan Das, D. (2017) CO2 Trapping in the Context of Geological Carbon Sequestration in Encyclopedia of Sustainable Technologies. *Elsevier*, Oxford: 461–475.
2. Metz, B., Davidson, O., de Coninck, H., and Loos, M. (2005) IPCC, 2005: Working Group III of the Intergovernmental Panel on Climate Change. IPCC Special Report on Carbon Dioxide Capture and Storage, Cambridge University Press, Cambridge, United Kingdom and New York, NY.
3. Cueto-Rojas, H. F., van Maris, A. J., Wahl, S. A., and Heijnen, J. J. (2015) Thermodynamics-based design of microbial cell factories for anaerobic product formation. *Trends Biotechnol.* **33**, 534–546.
4. Köpke, M., and Simpson, S. D. (2020) Pollution to products: recycling of 'above ground' carbon by gas fermentation. *Curr. Opin. Biotechnol.* **65**, 180–189.
5. Liew, F. E., Nogle, R., Abdalla, T., Rasor, B. J., Canter, C., Jensen, R. O., et al. (2022) Carbon-negative production of acetone and isopropanol by gas fermentation at industrial pilot scale. *Nat. Biotechnol.* **40**, 335–344.
6. Adam, P. S., Borrel, G., and Gribaldo, S. (2018) Evolutionary history of carbon monoxide dehydrogenase/acetyl-CoA synthase, one of the oldest enzymatic complexes. *Proc. Natl. Acad. Sci.* U. S. A. **115**, E1166–E1173.
7. Weiss, M. C., Preiner, M., Xavier, J. C., Zimorski, V., and Martin, W. F. (2018) The last universal common ancestor between ancient Earth chemistry and the onset of genetics. *PLoS Genet.* **14**, e1007518.
8. Yang, S., Lv, Y., Liu, X., Wang, Y., Fan, Q., Yang, Z., et al. (2020) Genomic and enzymatic evidence of acetogenesis by anaerobic methanotrophic archaea. *Nat. Commun.* **11**, 3941.
9. Can, M., Armstrong, F. A., and Ragsdale, S. W. (2014) Structure, function, and mechanism of the nickel metalloenzymes, CO dehydrogenase, and acetyl-CoA synthase. *Chem. Rev*. **114**, 4149–4174.

10. Doukov, T. I., Blasiak, L. C., Seravalli, J., Ragsdale, S. W., and Drennan, C. L. (2008) Xenon in and at the end of the tunnel of bifunctional carbon monoxide dehydrogenase/acetyl-CoA synthase. *Biochemistry* **47**, 3474–3483.
11. Can, M., Giles, L. J., Ragsdale, S. W., and Sarangi, R. (2017) X-Ray absorption spectroscopy reveals an organometallic Ni-C bond in the COtreated form of acetyl-CoA synthase. *Biochemistry* **56**, 1248–1260.
12. Cohen, S. E., Can, M., Wittenborn, E. C., Hendrickson, R. A., Ragsdale, S. W., and Drennan, C. L. (2020) Crystallographic characterization of the carbonylated A-cluster in carbon monoxide dehydrogenase/acetyl-CoA synthase. *ACS Catal.* **10**, 9741–9746.
13. Can, M., Abernathy, M. J., Wiley, S., Griffith, C., James, C. D., Xiong, J., et al. (2023) Characterization of methyl- and acetyl-Ni intermediates in acetyl CoA synthase formed during anaerobic CO2 and CO fixation. *J. Am. Chem. Soc.* **145**, 13696–13708.
14. Seravalli, J., and Ragsdale, S. W. (2008) Pulse-chase studies of the synthesis of acetyl-CoA by carbon monoxide dehydrogenase/acetyl-CoA synthase: evidence for a random mechanism of methyl and carbonyl addition. *J. Biol. Chem.* **283**, 8384–8394.
15. 15. Bender, G., Stich, T. A., Yan, L., Britt, R. D., Cramer, S. P., and Ragsdale, S. W. (2010) Infrared and EPR spectroscopic characterization of a Ni(I) species formed by photolysis of a catalytically competent Ni(I)-CO intermediate in the acetyl-CoA synthase reaction. *Biochemistry* **49**, 7516–7523.
16. James, C., Wiley, S., Ragsdale, S. W., and Hoffman, B. M. (2020) 13C electron nuclear double resonance spectroscopy shows acetyl-CoA synthase binds two substrate CO in multiple binding modes and reveals the importance of a CO-binding 'alcove'. *J. Am. Chem. Soc.* **142**, 15362–15370.
17. Tien, M. Z., Meyer, A. G., Sydykova, D. K., Spielman, S. J., and Wilke, C. O. (2013) Maximum allowed solvent accessibilites of residues in proteins. PLoS One 8, e80635.
18. Kumar, M., and Ragsdale, S. W. (1992) Characterization of the carbon monoxide binding site of carbon monoxide dehydrogenase from Clostridium thermoaceticum by infrared spectroscopy. *J. Am. Chem. Soc.* **114**, 8713–8715.
19. George, S. J., Seravalli, J., and Ragsdale, S. W. (2005) EPR and infrared spectroscopic evidence that a kinetically competent paramagnetic intermediate is formed when acetyl-coenzyme A synthase reacts with CO. *J. Am. Chem. Soc*. **127**, 13500–13501.

20. Seravalli, J., Kumar, M., and Ragsdale, S. W. (2002) Rapid kinetic studies of acetyl-CoA synthesis: evidence supporting the catalytic intermediacy of a paramagnetic NiFeC species in the autotrophic Wood-Ljungdahl pathway. *Biochemistry* **41**, 1807–1819.
21. Ragsdale, S. W., Wood, H. G., and Antholine, W. E. (1985) Evidence that an iron-nickel-carbon complex is formed by reaction of CO with the CO dehydrogenase from Clostridium thermoaceticum. *Proc. Natl. Acad. Sci. U. S. A.* **82**, 6811–6814.
22. Ragsdale, S. W., and Wood, H. G. (1985) Acetate biosynthesis by acetogenic bacteria: evidence that carbon monoxide dehydrogenase is the condensing enzyme that catalyzes the final steps of the synthesis. *J. Biol. Chem.* **260**, 3970–3977.
23. Gencic, S., Kelly, K., Ghebreamlak, S., Duin, E. C., and Grahame, D. A. (2013) Different modes of carbon monoxide binding to acetyl-CoA synthase and the role of a conserved phenylalanine in the coordination environment of nickel. *Biochemistry* **52**, 1705–1716.
24. Tan, X., Loke, H. K., Fitch, S., and Lindahl, P. A. (2005) The tunnel of acetyl-coenzyme a synthase/carbon monoxide dehydrogenase regulates delivery of CO to the active site. *J. Am. Chem. Soc.* **127**, 5833–5839.
25. Tan, X. S., Sewell, C., and Lindahl, P. A. (2002) Stopped-flow kinetics of methyl group transfer between the Corrinoid-iron-Sulfur protein and acetyl-coenzyme A synthase from Clostridium thermoaceticum. *J. Am. Chem. Soc.* **124**, 6277–6284.
26. Moffet, D. A., Case, M. A., House, J. C., Vogel, K., Williams, R. D., Spiro, T. G., et al. (2001) Carbon monoxide binding by de novo heme proteins derived from designed combinatorial libraries. *J. Am. Chem. Soc.* **123**, 2109–2115.
27. Liew, F., Henstra, A. M., Winzer, K., Kopke, M., Simpson, S. D., and Minton, N. P. (2016) Insights into CO2 fixation pathway of Clostridium autoethanogenum by targeted mutagenesis. *mBio* **7**, e00427–e00516.
28. Darnault, C., Volbeda, A., Kim, E. J., Legrand, P., Vernede, X., Lindahl, P. A., et al. (2003) Ni-Zn-[Fe(4)-S(4)] and Ni-Ni-[Fe(4)-S(4)] clusters in closed and open alpha subunits of acetyl-CoA synthase/carbon monoxide dehydrogenase. *Nat. Struct. Biol.* **10**, 271–279.
29. Cohen, S. E., Brignole, E. J., Wittenborn, E. C., Can, M., Thompson, S., Ragsdale, S. W., et al. (2021) Negative-stain electron microscopy reveals Dramatic structural

Rearrangements in Ni-Fe-S-dependent carbon monoxide dehydrogenase/Acetyl-CoA Synthase. *Structure* **29**, 43–49.e43.

30. Seravalli, J., Brown, K. L., and Ragsdale, S. W. (2001) Acetyl coenzyme A synthesis from unnatural methylated corrinoids: requirement for "baseoff" coordination at cobalt. *J. Am. Chem. Soc.* **123**, 1786–1787.
31. Hedstrom, L. (2002) Serine protease mechanism and specificity. *Chem. Rev.* **102**, 4501–4524.
32. Banerjee, R., and Lipscomb, J. D. (2021) Small-molecule tunnels in metalloenzymes viewed as extensions of the active site. *Acc. Chem. Res.* **54**, 2185–2195.
33. Rroehlich, J. D., and Kubiak, C. P. (2015) The homogeneous reduction of CO2 by [Ni (cyclam)]+: increased catalytic rates with the addition of a CO scavenger. *J. Am. Chem. Soc.* **137**, 3565–3573.
34. Manesis, A. C., O'Connor, M. J., Schneider, C. R., and Shafaat, H. S. (2017) Multielectron chemistry within a model nickel Metalloprotein: mechanistic implications for acetyl-CoA synthase. *J. Am. Chem. Soc.* **139**, 10328–10338.
35. Collman, J. P., Brauman, J. I., and Doxsee, K. M. (1979) Carbon monoxide binding to iron porphyrins. *Proc. Natl. Acad. Sci. U. S. A.* **76**, 6035–6039.
36. Lindahl, P. A. (2004) Acetyl-Coenzyme A synthase: the case for a Nip0based mechanism of catalysis. *J. Biol. Inorg. Chem.* **9**, 516–524.
37. Bramlett, M. R., Stubna, A., Tan, X., Surovtsev, I. V., Munck, E., and Lindahl, P. A. (2006) Mossbauer and EPR study of recombinant acetylCoA synthase from Moorella thermoacetica. *Biochemistry* **45**, 8674–8685.
38. Gencic, S., Duin, E. C., and Grahame, D. A. (2023) The two-electron reduced A cluster in acetyl-CoA synthase: preparation, characteristics and mechanistic implications. *J. Inorg. Biochem*. **240**, 112098.
39. Lu, W. P., and Ragsdale, S. W. (1991) Reductive activation of the coenzyme A/acetyl-CoA isotopic exchange reaction catalyzed by carbon monoxide dehydrogenase from Clostridium thermoaceticum and its inhibition by nitrous oxide and carbon monoxide. *J. Biol. Chem.* **266**, 3554–3564

40. Volbeda, A., Darnault, C., Tan, X., Lindahl, P. A., and Fontecilla-Camps, J. C. (2009) Novel domain arrangement in the crystal structure of a truncated acetyl-CoA synthase from Moorella thermoacetica. *Biochemistry* **48**, 7916–7926.
41. Gencic, S., Duin, E. C., and Grahame, D. A. (2010) Tight coupling of partial reactions in the acetyl-CoA decarbonylase/synthase (ACDS) multienzyme complex from Methanosarcina thermophila: acetyl C–C bond fragmentation at the a cluster promoted by protein conformational changes. *J. Biol. Chem.* **285**, 15450–15463.
42. Kopke, M., Mihalcea, C., Liew, F., Tizard, J. H., Ali, M. S., Conolly, J. J., et al. (2011) 2,3-butanediol production by acetogenic bacteria, an alternative route to chemical synthesis, using industrial waste gas. *Appl. Environ. Microbiol*. **77**, 5467–5475.
43. Heijstra, B. D., Kern, E., Koepke, M., Segovia, S., Liew, F., Heijstra, B., et al. (2013) inventors; Novel Bacteria and Methods of Use Thereof US20130217096A1. U.S. Patent and Trademark Office, Washington, DC.
44. Nagaraju, S., Davies, N. K., Walker, D. J., Kopke, M., and Simpson, S. D. (2016) Genome editing of Clostridium autoethanogenum using CRISPR/ Cas9. *Biotechnol. Biofuels* **9**, 219.
45. Elliott, J. I., and Brewer, J. M. (1978) The inactivation of yeast enolase by 2,3-butanedione. *Arch. Biochem. Biophys*. **190**, 351–357.
46. Burton, R., Can, M., Esckilsen, D., Wiley, S., and Ragsdale, S. W. (2018) Production and properties of enzymes that activate and produce carbon monoxide. *Methods Enzymol.* **613**, 297–324.
47. Fee, J. A. (1978) Transition metal electron paramagnetic resonance related to proteins. *Methods Enzymol.* **49**, 512–528.
48. Tenderholt, A., Hedman, B., and Hodgson, K. O. (2007) PySpline: a modern. In: Hedman, B., Pianetta, P., eds. Cross-Platform Program for the Processing of Raw Averaged XAS Edge and EXAFS Data in X-Ray Absorption Fine Structure - XAFS13, American Institute of Physics, Stanford University, Stanford, CA: 105–107.
49. Rehr, J. J., Deleon, J. M., Zabinsky, S. I., and Albers, R. C. (1991) Theoretical X-ray absorption fine-structure standards. *J. Am. Chem. Soc.* **113**, 5135–5140.

50. Zabinsky, S. I., Rehr, J. J., Ankudinov, A., Albers, R. C., and Eller, M. J. (1995) Multiple-scattering Calculations of X-ray-absorption spectra. *Phys. Rev. B* **52**, 2995–3009.
51. Hanwell, M. D., Curtis, D. E., Lonie, D. C., Vandermeersch, T., Zurek, E., and Hutchison, G. R. (2012) Avogadro: an advanced semantic chemical editor, visualization, and analysis platform. *J. Cheminform.* **4**, 17.
52. George, G. N. (2000) EXAFSPAK and EDG-FIT, Stanford Synchrotron Radiation Laboratory. Stanford Linear Accelerator Center, Stanford, CA.
53. Wedemeyer-Exl, C., Darbre, T., and Keese, R. (2008) Preparation of Dicyano- and Methylcobinamide from Vitamin B 12a. *Synthesis* 2008, 3429–3432.
54. Seefeldt, L. C., and Ensign, S. A. (1994) A continuous, spectrophotometric activity assay for nitrogenase using the reductant titanium(III) citrate. *Anal. Biochem.* **221**, 379–386.
55. Morton, T. A., Runquist, J. A., Ragsdale, S. W., Shanmugasundaram, T., Wood, H. G., and Ljungdahl, L. G. (1991) The primary structure of the subunits of CO dehydrogenase/acetyl-CoA synthase from Clostridium thermoaceticum. *J. Biol. Chem.* **266**, 23824–23838.
56. Crooks, G. E., Hon, G., Chandonia, J.-M., and Brenner, S. E. (2004) WebLogo: a sequence logo generator. *Genome Res.* **14**, 1188–1190

Chapter 3 Characterization of the Methyl- and Acetyl-Ni Intermediates in Acetyl CoA Synthase Formed During Anaerobic CO_2 and CO fixation

3.1 Abstract

The Wood-Ljungdahl Pathway is a unique biological mechanism of carbon dioxide and carbon monoxide fixation proposed to operate through nickel-based organometallic intermediates. The most unusual steps in this metabolic cycle involve a complex of two distinct nickel-iron-sulfur proteins: CO dehydrogenase and acetyl-CoA synthase (CODH/ACS). Here we describe the nickel-methyl and nickel-acetyl intermediates in ACS completing the characterization of all its proposed organometallic intermediates. A single nickel site (Nip) within the A cluster of ACS undergoes major geometric and redox changes as it transits the planar Nip, tetrahedral Nip-CO and planar Ni-Me and Nip-Ac intermediates. We propose the Nip intermediates equilibrate among different redox states, driven by an electrochemical-chemical (EC) coupling process, and that geometric changes in the A-cluster linked to large protein conformational changes control entry of CO and the methyl group

3.2 Introduction

The Wood-Ljungdahl pathway (WLP) is the sole carbon-fixing pathway that conserves energy and is central to Earth's environmental chemistry. The key pathway enzymes, acetyl-CoA synthase (ACS) and carbon monoxide dehydrogenase (CODH), were present in the last universal common ancestor, (1) thus recycling and mineralizing atmospheric CO_2 or CO for billions of years.

The WLP has been proposed to operate through a series of nickel-based organometallic intermediates bound to ACS (Figure 3-1), (2) reminiscent of the rhodium-based Monsanto process for industrial acetic acid synthesis. While this concept has been widely accepted, its validation by visualization of the metal-carbon bonds has been challenging. The carbonylated, methylated, and acetylated species are enzyme-bound and thought to occur at a single Ni (Ni_p) within the Ni_2-[4Fe-4S] A-cluster of ACS (Figure 3-1). The existence of an intermediate state in which both CO and methyl are independently bound to the Ni is based on the observation of an

exchange reaction catalyzed by CODH/ACS between ^{12}CO and [1-^{14}C]-acetyl-CoA. (2) Furthermore, ACS has been traditionally studied as part of the CODH/ACS complex, which exhibits relatively low (~30%) activity, is subject to rapid inactivation by exposure to even low oxygen levels, and contains a total of 3 Ni and 14 Fe atoms. Other major limitations are that many of the intermediates shown in Figure 1 appear to be unstable.

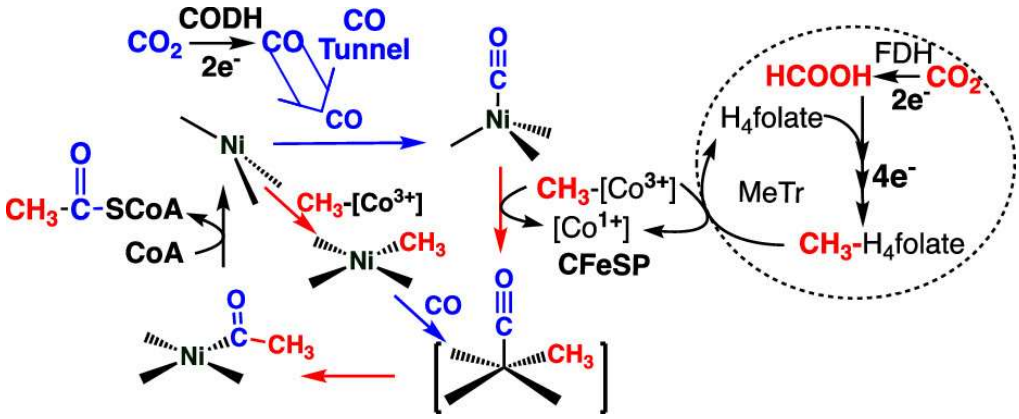

Figure 3-1 Simplified scheme of the ACS intermediates involved in the WLP highlighting the nickel–carbon bonds formed in the catalytic cycle.

To overcome these challenges, we developed a highly active recombinant ACS-only construct lacking CODH, which was used previously to trap the Ni_p-CO intermediate, and characterize it by X-ray absorption spectroscopy (XAS) (3) and X-ray diffraction (XRD) (4) methods. As described here, we have now isolated and characterized the methyl (A_{Me}) and the acetyl (A_{Ac}) intermediates, validating the key tenet of the organometallic nature of the WLP.

A debate exists regarding whether the WLP operates through a paramagnetic (Figure 3-2a) or diamagnetic (Figure 3-2d) mechanism. The paramagnetic scheme includes $Ni_p(I)$, $Ni_p(I)$–CO, $Ni_p(III)$–Me, and $Ni_p(III)$–Ac species as the catalytic intermediates. Pulse-chase experiments demonstrate that both $Ni_p(I)$–CO and Ni_p–CH_3 are viable intermediates. (5) On the other hand, the diamagnetic mechanism (Figure 3-2d) proposes "$Ni_p(0)$", $Ni_p(II)$–Me, and $Ni_p(II)$–Ac intermediates. As shown in Figure 3-2c, $Ni_p(0)$ is usually formulated as a Ni^{1+}–$[Fe4S4]^{1+}$ state. Proponents of the diamagnetic mechanism also propose that $Ni_p(I)$–CO (A_{NiFeC}) is an inhibited state and that substrates bind in a strictly ordered manner, first methyl and then CO. (6-8) In yellow highlighting of Figure 3-2d, we include the mechanism with CO binding first.

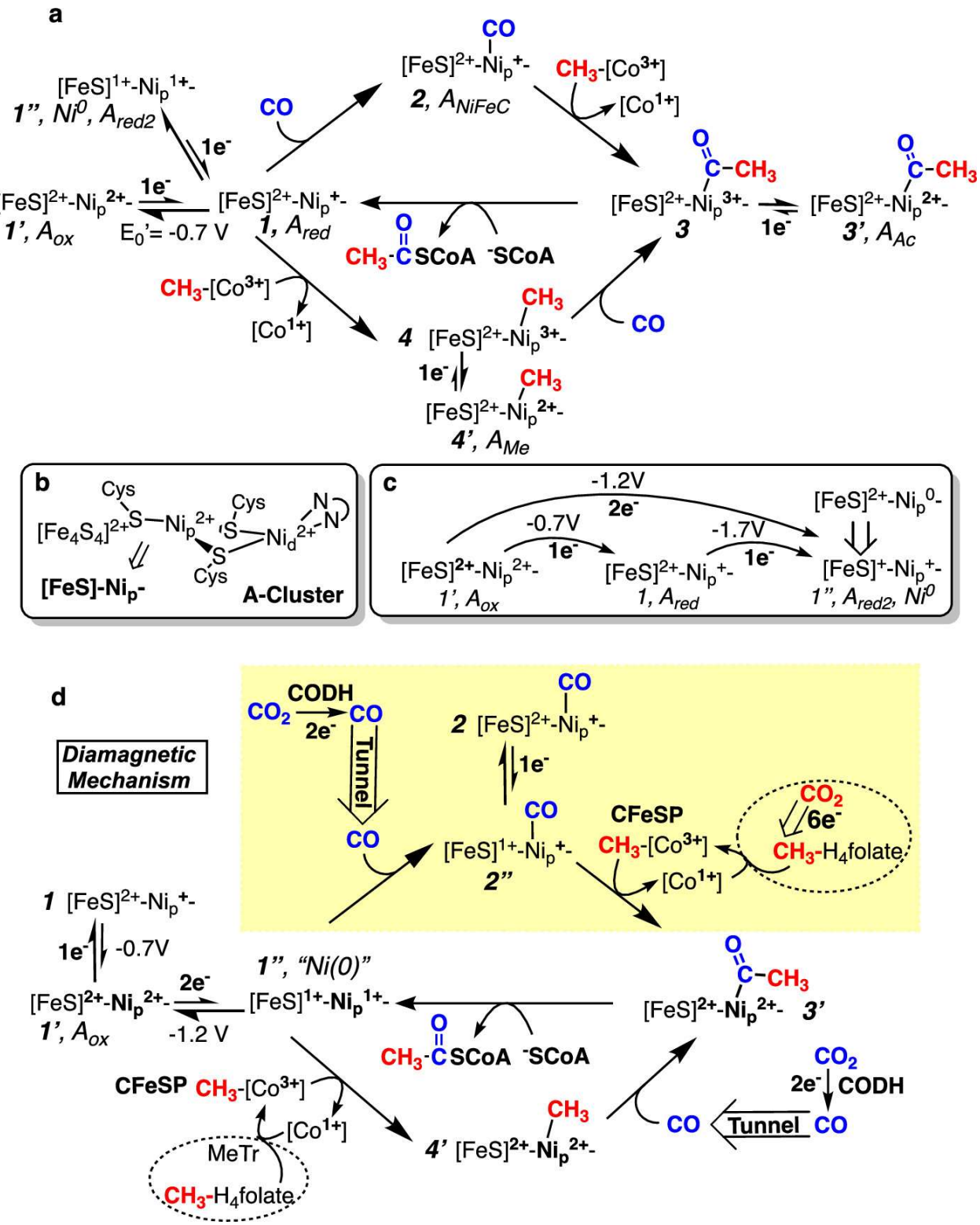

Figure 3-2 Proposed ACS mechanism including electrochemical coupling (EC mechanism). (a) WLP catalytical cycle with proposed intermediates and formal oxidation states in ACS. The WLP includes two branches, which converge at the ACS A-cluster active site. Methyl branch (red): CO_2 undergoes reduction to a methyl group (methyl-tetrahydrofolate, methyl-H_4folate) shown in the dashed circles, which experiences stepwise transfer to cobalt in a B_{12} cofactor bound to the corrinoid iron–sulfur protein (CFeSP) and then to ACS. Carbonyl branch (blue): CODH

catalyzes CO2 reduction to CO, which enters a 75 Å tunnel (12,13) to the ACS active site. The proximal Ni (Ni_p) in the A-cluster (1) randomly binds either CO or CH_3 to form Ni_p–CO (2, ANiFeC) or Nip–CH3 (4) (or vice versa). (5) C–C bond condensation generates acetyl-Nip (3, Nip–Ac), followed by CoA binding and thiolysis to form acetyl-CoA, which is then incorporated into biomass or converted to acetate and ATP. (b) The A cluster structure with oxidation states corresponding to its resting A_{Ox} state. (c) Calculated electrochemical potentials associated with the different states of the A-cluster, including the hypothesized diamagnetic Nip(0) state. (14) (d) The diamagnetic mechanism involving conversion of Ni_p("0") to Ni_p(II)–CH3 and Ni_p(II)–Ac as intermediates. The highlighted box includes the option of CO binding first, then methyl, consistent with pulse-chase experiments (see text for details).

In Figure 3-2, we omitted the proposed intermediate Ni_p(CO)(CH3) state shown in Figure 3-1 in which both CO and methyl are independently bound to Ni. This state is an intermediate in the WLP because ACS catalyzes an exchange reaction between ^{12}CO and the [1-^{14}C] carbonyl group of acetyl-CoA. This reaction requires C–C and C–S bond cleavage to form the state with CH_3, CO, and CoA independently bound to ACS, $^{12}CO/^{14}CO$ exchange, then condensation of these three groups to reform acetyl-CoA. (2) An analogous state has been observed in inorganic complexes as an intermediate in carbonyl insertion into the metal–CH3 bond during acetate synthesis. (9)

Here, we describe a combination of spectroscopic experiments on trapped Ni_p(II)-Me (4′, A_{Me}) and Ni_p(II)–Ac (3′, A_{Ac}) intermediates in the WLP. We propose a novel electrochemical (EC) coupling mechanism to address the debate between the diamagnetic and paramagnetic mechanisms, (10) which explains how ACS transits through these characterized Ni_p(II) species, while recruiting transient Ni_p(I), Ni_p(III)–Me, and Ni_p(III)–Ac intermediates into the catalytic cycle to generate acetyl-CoA. These studies complete the electronic and geometric structure characterization of all organometallic intermediates in the catalytic mechanism of ACS and provide important insight into how anaerobic microbes fix CO_2 and CO.

3.3 Results

3.3.1 The Methylated Intermediate

An array of spectroscopic and biochemical methods was used to characterize the organometallic Nip–Me (A_{Me}) state of the A-cluster. Details of A_{Me} synthesis are included in the Materials and Methods section in the Supporting Information. Methyl-cob(III)inamide, instead of methyl-CFeSP, was used as a methyl donor because it employs the same mechanism (11) and eliminates the Fe signals from the CFeSP's $[4Fe–4S]^{2+}$ cluster from averaging into those of ACS. This allows for the interrogation of the methyl transfer reaction using Co, Fe, and Ni X-ray absorption spectroscopy. Prior to characterizing the methylated form, the amount of active A_{Ox}

was confirmed by creating the paramagnetic species A_{NiFeC} (2) by reacting A_{Ox} with CO, as we have described previously. (3) This species was then characterized using X-band cw-EPR, yielding a spin quantification of 83%. Given the metal loading of this ACS preparation (100% Fe and 85% Ni), this signals the complete conversion of active A_{Ox} to A_{NiFeC} and 83% active A_{Ox}. With this in mind, the extent of cob(III)inamide demethylation by ACS was assessed using Co K-edge XAS, and a comparison was made on the extent of Ni_p methylation using Ni K-edge XAS (Figures 3-3, S1 and Table S1). The Co K-rising-edge of AOx treated with methyl-cob(III)inamide is ∼0.8 eV redshifted relative to methyl-cob(III)inamide (Figures 3-3b and S1) and matches well with the ∼1.2 eV redshift observed in the reference compounds methyl-cob(III)alamin and the two-electron reduced cob(I)alamin (Figure 3-3a). Additionally, the intense pre-edge feature characteristic of the Co–C bond at 7710.9 eV disappears and a lower energy, weak feature appears at 7709.8 eV, suggesting near full conversion of methyl-cob(III)inamide to cob(I)inamide. These data support the transfer of the methyl group as a methyl cation from methyl-cob(III)inamide to AOx. The Co K-edge XAS (Figure 3-3) suggests the near-complete conversion of 1 equivalent of methyl-cob(III)inamide to cob(I)inamide upon reaction with A_{Ox} in the presence of the reductant Ti(III)-citrate.

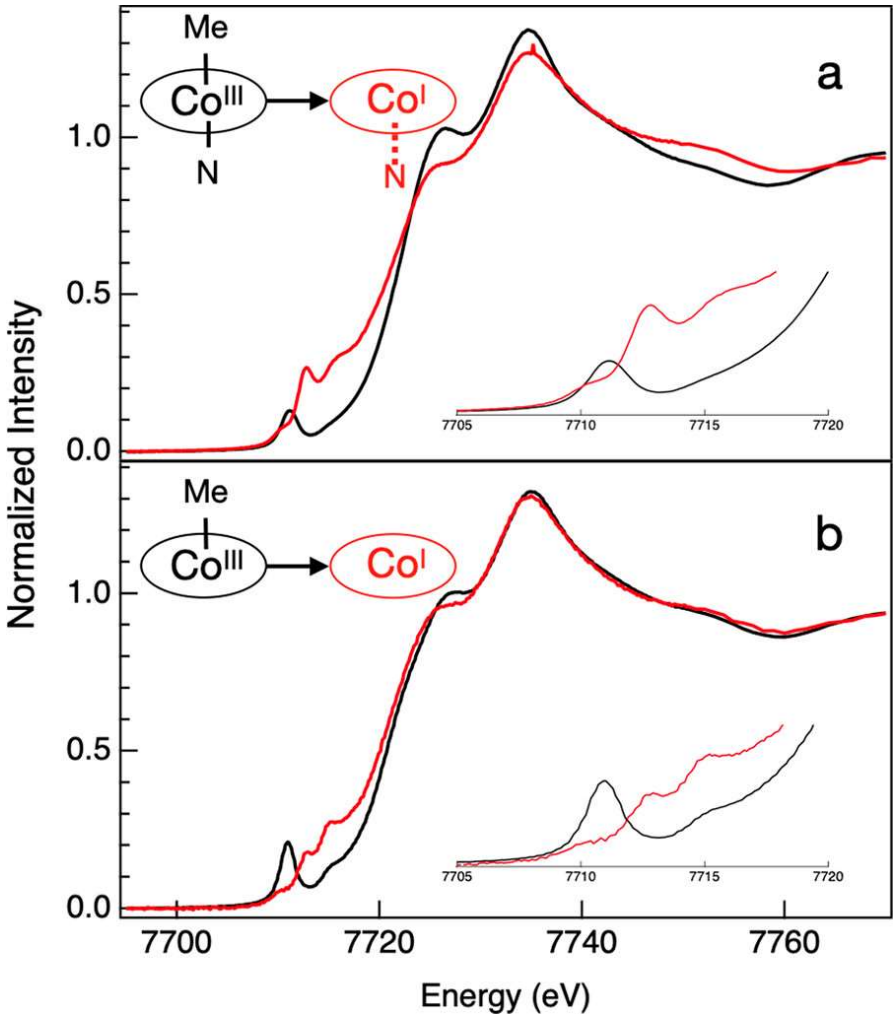

Figure 3-3 Methylation of ACS observed by Co K-edge XAS. (a) Normalized Co K-edge XAS of methyl-cob(III)alamin (black lines) and cob(I)alamin (red lines) as reference compounds. (b) Co K-edge XAS of the reaction of methyl-cob(III)inamide with no ACS present (black lines) and cob(I)alamin (red lines) as reference compounds. (b) Co K-edge XAS of the reaction of methyl-cob(III)inamide with no ACS present (black lines) and with Ti(III) citrate-treated AOx to generate cob(I)inamide (red lines). The insets show the expanded pre-edge regions.

Transformations at the cobinamide cobalt during the methylation of ACS were also monitored using UV–visible spectroscopy (Figure S1) using a separate preparation of ACS (further details are available in the SI), providing evidence for the stoichiometric conversion to methylated-ACS by a nucleophilic SN2-type methyl transfer and suggesting the formation of a Nip(III)–Me product, as described previously. (11) Generation of Co(II) or Co(III) would have suggested transfer of a methyl radical or anion, respectively. Importantly, reduction of the methyl-cob(III)inamide by Ti(III)-citrate was not observed, indicating that the Cob(I)inamide was exclusively formed through the methyl transfer reaction (Figure S1c).

Ni K-edge XAS measurements were performed on the same sample as the Co K-edge XAS (1 equivalent (1×) methyl-cob(III)inamide) and on another sample with 5 equivalents (5×) of methyl-cob(III)inamide. The comparison Ni K-edge XAS and EXAFS data are presented in Figure S1e,f. These data indicate near-identical levels of methylation in the 1× and 5× samples, as judged by the similarity in the spectral shape, but are also consistent with the presence of only a small percentage of unconverted A_{Ox} in the 1×. Therefore, the results and analysis presented here (Figure 3-4) are based on the 5× dataset. Note that, as expected by the similarity in the datasets, the pre-edge analysis and fits to the Ni K-edge EXAFS data on the 1× and 5× samples were nearly identical.

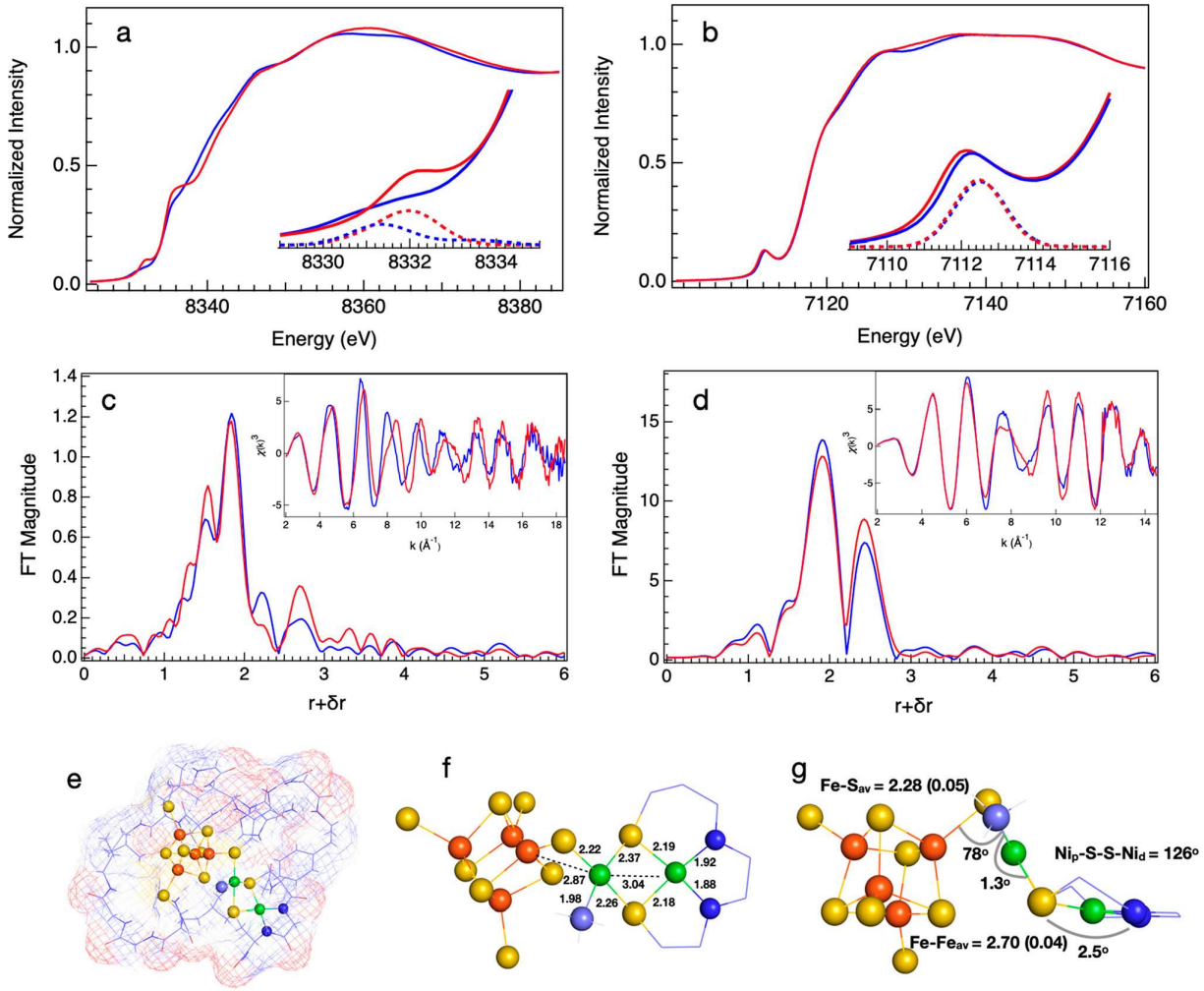

Figure 3-4 Structure of A_{Ox} and A_{Me} obtained from XAS and DFT. (a) Ni K-edge XAS and (b) Fe K-edge XAS showing changes to the near and rising edge regions upon methylation of A_{Ox} (blue lines) to A_{Me} (red lines). The insets show the expanded pre-edge region and corresponding TD-DFT calculations (dotted lines). (c) Ni K-edge EXAFS (inset) and (d) Fe K-edge EXAFS (inset) with corresponding Fourier transforms. (e–g) Calculated structural parameters of the [4Fe–4S]–Ni_p(Me)–Ni_d active site of A_{Me} obtained from DFT.

Upon addition of a five-fold excess of methyl-cob(III)inamide and Ti(III)-citrate to AOx, significant changes are observed in the Ni K-pre-edge and rising-edge regions (Figure 3-4a). The pre-edge, which is reflective of the 1s → 3d transition, blueshifts by ∼0.8 eV and its intensity increases markedly. The rising-edge shifts to higher energy by ∼1.0 eV and the feature at ∼8335.2 eV in A_{Ox} changes to a pronounced shoulder. These results suggest that methyl binds at the Nip center (Nid has been shown to play a largely structural role), which is further confirmed by high-k EXAFS refinement. Detailed first and second shell EXAFS fits and their comparison to A_{Ox} are presented in the Supporting Information (Table S2). The fit results indicate that while the geometries remain similar for A_{Ox} and A_{Me}, the weak water ligand is replaced by a light atom ligand in the first shell at a shorter distance. This is fit well with a Ni_p–C at 1.98 Å (Figures 3-4c, S2 and Table S2). (1) Ni–S ligand elongates by 0.13 Å (Table S2). A prominent backscattering peak owing to the Ni_p–Ni_d and Ni_p–Fe contributions is also present in the second shell of the Fourier-transform Ni EXAFS, which was also fit to 2.98 Å, confirming the proper metal loading at the active site. Additionally, sharpening of the Ni K-rising-edge feature on conversion of A_{Ox} to A_{Me} is consistent with increasing planarity at the Ni sites suggested by theoretical calculations (see below) that show that the planarity of Ni_d remains unaltered while Ni_p approaches a square-planar configuration upon methyl binding. (15−19) It is important to note here that our XAS results contrast with prior XAS studies of the A_{Me} form of *Carboxydothermus hydrogenoformans* ACS, (20) which showed a rising-edge shifted to lower-energy relative to A_{Ox}, and assignment of a weak ∼2.4 Å Ni–Me, bound in the apical position of a square pyramid. The study lacks from supporting kinetic or spectroscopic quantification of the percentage methylation as well as the extent of metal loading at the Ni_p, Ni_d, and $[4Fe–4S]^{2+}$ cluster sites and comparison with the data presented here suggest only modest methylation in the experiments on the *C. hydrogenoformans* ACS. Our studies on multiple samples (Figures S1 and S3) found that at least 75% methylation is required to sufficiently describe the A_{Me} state. Additional discussion comparing this work to our study is presented in the SI.

The ∼1 eV blue-shift in the rising-edge energy position in A_{Me} indicates an increase in average positive charge at the Ni centers, attributable either to the formation of a Ni_p(III)–Me (21,22) or a Ni_p(II)–Me exhibiting rearrangement/delocalization. (17,18,23) To differentiate, we compared EPR and Q-band ENDOR spectra of Ti(III)-citrate-treated ACS samples that were reacted with CH_3-, $^{13}CH_3$-, and CD_3-cobinamide, which would generate the corresponding CH_3,

$^{13}CD_3$, and $^{13}CH_3$ forms of A_{Me}. All A_{Me} samples exhibit EPR spectra with a prominent feature at g ~ 2.32 (Figure 3-5A), reminiscent of the Ni(I) or Ni(III)–Me states of methyl-coenzyme M reductase (24) and the Nip(I) state of ACS, generated by photolysis; (25) however, signals in this region could also be attributed to the g⊥ feature of the Co(II) states of the CFeSP (26) and cob(II)inamide. (27) If the EPR signal derives from A_{Me}, hyperfine splitting from the labeled methyl group would be observed; however, if the EPR signal derives from Co(II), no splittings are expected. Thus, we compared ENDOR analysis of this reaction of ACS with methyl-cob(III)inamide (Figure 3-S5).

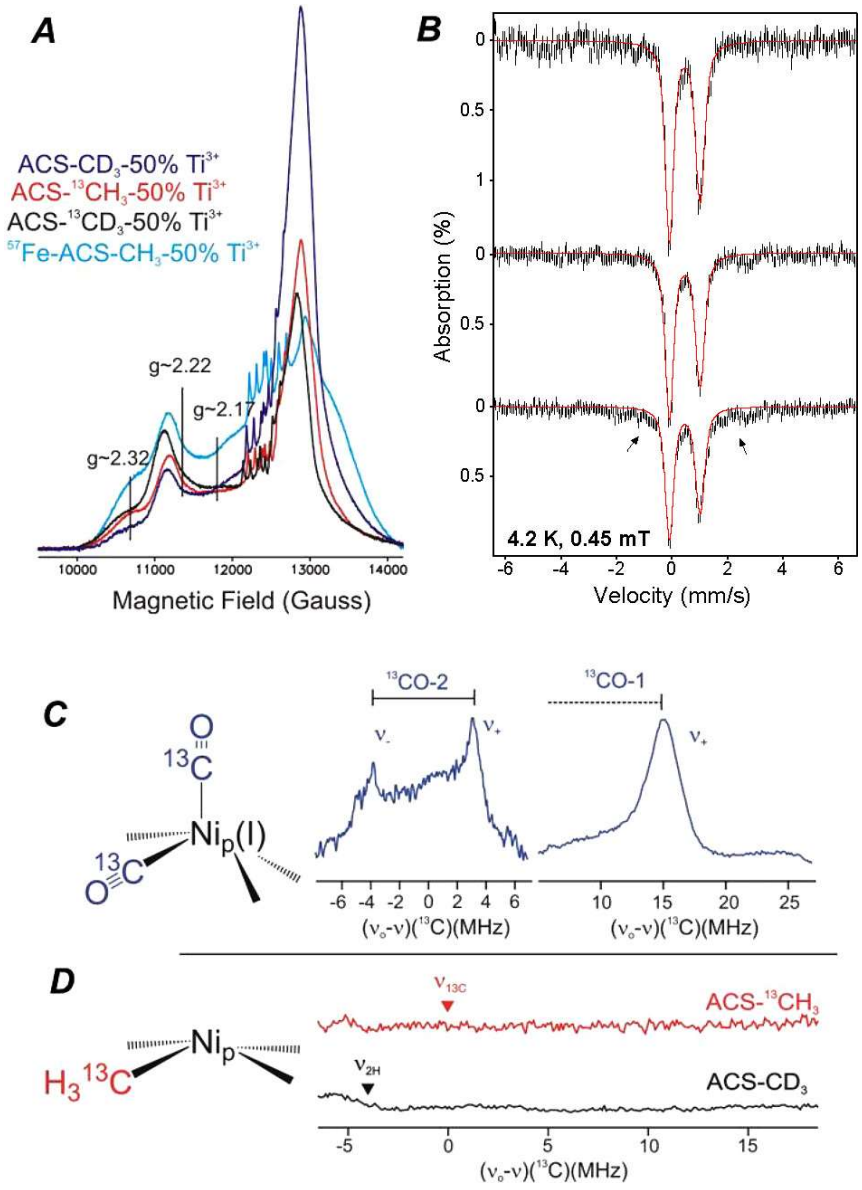

Figure 3-5 Characterization of the AMe State of ACS. (a) Absorption-display, dispersion-detected Q-band CW-EPR (2 K) of AMe with the following isotopes: CD3-, 13CH3-, 13CD3-, 57Fe/13CH3. (b) 4.2 K Mössbauer spectra

(black lines) and simulations (red lines) of Aox (top), AMe (middle) and AAc (bottom), with arrows indicating regions not included in the simulations. (c) 13C ENDOR spectra of ANiFeC (2) with two (13) COs covalently bound to the Nip(I) center in the A-cluster of ACS. (51) (d) ENDOR spectra of 13C- and 2H-labeled AMe to test whether the EPR spectrum of Figure 4A is from a Nip(III)–Me complex. The absence of a 13C signal from the presence of 13CH3 and of a 2H signal from the presence of CD3 shows that this EPR signal is not from a Nip(III)–Me complex. The 13C and 2H Larmor frequencies are shown on the spectra.

The ^{1}H and ^{2}H ENDOR for ACS-$^{13}CH_3$ and ACS-$^{13}CD_3$, respectively, are indistinguishable (Figure S5C), the ^{1}H ENDOR spectrum is unchanged by deuteration of the methyl group, and there is no ^{2}H ENDOR response from ACS-CD3 (Figure S5A) at g-2.32 for AMe. While strong ^{13}C couplings (~30 MHz) have been observed for the carbonylated state of ACS (Species 2, Figure 3-5C), the ^{13}C ENDOR spectra of $^{13}CH_3$-AMe showed no ^{13}C signal (Figure 3-5D). Additional ENDOR spectra of $^{13}CH_3$-A_{Me} and $^{12}CH_3$-A_{Me} were collected over a broader frequency range and likewise showed no ^{13}C signals (Figure S5B). Lastly, ENDOR spectra of ^{61}Ni- and ^{57}Fe- labeled A_{Me} showed no signals attributable to those nuclei (Figure S6). These combined ENDOR results conclusively demonstrate that the g ~ 2.32 feature in the EPR spectrum of A_{Me} (Figure 3-5A) does not arise from a paramagnetic Ni–Me center. Instead the EPR signals at or near g ~ 2.32 are attributable to Co(II) formed by equilibration between Ti(III)-citrate and a majority cob(I)inamide product formed during the methyl transfer reaction. It should be noted that the redox potential for the Co(II)/(I) couple is −490 mV, (27) which is near that for Ti(IV)/Ti(III)-citrate (−570 mV), allowing for this equilibriation. (28) Together, the Ni-XAS, EPR, and ENDOR data indicate that the A_{Me} product observed in this reaction is a Ni_p(II)–Me species, not an EPR-active Ni_p(I)–Me or Ni_p(III)–Me, the expected product of the SN2 cob(III)inamide methyl transfer.

One possible explanation for formation of Ni_p(II)–Me instead of the expected Ni_p(III)–Me is that the spin on Ni is highly delocalized onto the [4Fe–4S] of the A-cluster, converting it from the 2+ to the paramagnetic 3+ state. To test this hypothesis, we performed Mössbauer spectroscopy on A_{Ox}, A_{Me}, and A_{Ac} (Figure 3-5B). All datasets exhibit a quadruple doublet with an asymmetric absorption linewidth representing ~95% of the total iron in both A_{Ox} and A_{Me}, with isomer shifts (δ, 0.47 mm/s) and quadrupole splittings (ΔEQ, 1.11 mm/s) consistent with the [4Fe–4S] cluster of A_{Me} remaining in the diamagnetic $[4Fe–4S]^{2+}$ state upon methylation (Table S4). These spectra are also consistent with previous Mössbauer studies on ACS. (29,30) We also obtained Fe K-edge XAS and EXAFS data (Figure 3-4b,d, Table S3) on A_{Ox} and A_{Me} which show very similar Fe K-edge XAS data, with only a small shift in the pre-edge energy position.

More prominent changes are observed in the Fe K-edge EXAFS data. These results indicate structural perturbations, not oxidation state changes, in the cluster upon methyl binding. Together, these lines of evidence suggest that delocalization of spin from a Ni_p(III)–Me onto the [4Fe–4S] cluster does not resolve the conundrum.

With the possibility of spin delocalization ruled out, broken symmetry (BS) DFT calculations on the low-spin as well as a high-spin (triplet) calculation were performed using a ∼300 atom model (Figure S7) of the Ni_p(II)–Me species, A_{Me} (4′) (Figure 4e–g and Tables S5–S7) to better understand the potential electronic configurations and structures in question. DFT and TD-DFT have been successfully employed in prior investigations to describe the electronic and geometric structures of ACS and other biological Fe–S clusters. (3,31−35) Both BS-low-spin and high-spin ground states converged to approximately square planar geometries. The low-spin configuration was lower in energy (∼8.8 kcal mol–1) and showed better agreement with the experimental data. The high-spin state converged with unpaired spin density localized on the $[4Fe–4S]^{2+}$ cluster, a situation already ruled out by the Mössbauer data. Furthermore, a high-spin Nip(II) species would perturb the ENDOR dataset relative to A_{Ox}, which is not observed. Additionally, the blueshift observed in the Ni K-rising-edge in A_{Me} relative to A_{Ox} is inconsistent with the conversion of a low-spin Ni_p(II) to a high-spin Ni_p(II) species with similar ligands. (36) XAS is useful for diagnosing spin transitions within similar ligand systems since low-spin systems exhibit rising edges to higher energies than their high-spin counterparts. (37) This interpretation is based on multiple scattering theory, which proposes that the rising-edge energy positions are inversely correlated to the M–L bond distance. All other factors being equal, high-spin systems tend to bear longer M–L bond lengths, which manifest in lower rising-edge energy positions. (38,39) The calculated Ni–C_{methyl} distances were 1.98 and 1.99 Å for the low-spin and high-spin Ni_p(II)–Me (4′) structures, respectively, with the methyl group forming a planar Me–Ni_p(II)$S(Cys)_3$ site in both spin states. The Ni_p(II) sits closer to the S_3C plane in the low-spin (∠Ni_pSSS dihedral angle = ∼1.4°) case (Figure 4g) than it does in A_{Ox} (∼5.2°, Figure S8). The high-spin structure is slightly more distorted with ∠NiSSS closer to A_{Ox} (3.9°). In both spin cases, the Ni_d(II) undergoes small first-shell bond distance perturbations but remains in its square-planar Ni_p(II)S_2N_2 arrangement similar to that in A_{Ox}. It should be noted that a quantitative correlation between the dihedral angle of nearly square-planar systems and the rising-edge energy position cannot be made due to other factors contributing to the intensity of

the shoulder. However, the sharpening of the shoulder in 4′ is qualitatively consistent with the low-spin calculation. It is interesting that the high-spin calculation did not converge to a tetrahedral geometry or with a longer Ni–Me distance at the Ni_p site since high-spin Ni_p(II) complexes favor tetrahedral geometry with longer distances, leading to an energetically favorable scenario for the unpaired electrons. This is likely because the DFT structure is optimized from the "open" conformation crystal structure (1OAO) and the F512 residue position prevents Ni_p(II) from becoming tetrahedral (Figures S13 and S14, see discussion on Role of Second-Sphere Ligands below. The closed conformation structure has been shown to be associated with the CO bound intermediate). In other words, a tetrahedral or D_{2d} distorted site is also incompatible with crystallography data (1OAO). Additionally, the data on 4′ are consistent with square-planar geometry, as shown in a comprehensive Ni K-edge XAS study by Colpas et al. (17) They demonstrate that square planar complexes have sharp rising-edge features in contrast to tetrahedral complexes which have comparatively featureless rising edges. A more recent study by Shearer and co-workers also demonstrates the stark difference in the rising-edge position of square planar and D2d distorted binuclear Ni centers. (40) Another important comparison from the Colpas study is between high-spin (41) versus low-spin (42) complexes with comparable S4 ligand systems. The low-spin complex has a rising-edge ∼0.7 eV higher than the high-spin complex with similar ligands. The ∼1 eV blueshift of the rising-edge in A_{Me} (4′) relative to the low-spin A_{Ox} can therefore only be supported by a low-spin assignment of 4′. Other supporting evidence comes from the EXAFS elongation of Fe–Fe distance from A_{Ox} to A_{Me} (ΔFe–Fe = 0.01 Å), which, albeit small, is reproduced by the BS-low-spin Nip(II) calculations (Table S6). Furthermore, the corresponding low-spin TD-DFT calculated ground states of this system successfully simulate the intensity and energy trends for the Ni and Fe K-pre-edge features (Figure 3-4a,b (inset), Tables S8 and S9). The Ni K-edge XAS data and TD-DFT calculations convey an increase in Ni 3d–4p mixing in A_{Me} (relative to A_{Ox}) which is consistent with the formation of a short Ni–C_{methyl} bond along the equatorial plane relative to water that occupies that position in A_{Ox}. Finally, Hirshfeld spin-density analysis indicates a diamagnetic ground state for the $[4Fe–4S]^{2+}$ cluster, consistent with the Mössbauer data (Table S10). Together, these results support the formation of a low-spin Ni_p(II)–Me species in A_{Me} (4′).

A comparison of the 1.98 Å Ni–C_{methyl} distance was made with available Ni–Me molecular structures in the Cambridge structure database (Figure S9a) (without separating on the

basis of spin states). The comparison reveals more than 80 examples of complexes containing Ni–Me moieties with a Ni–C_{methyl} distance of 1.98 Å (±0.01 Å). Of these, the closest methylated ACS analogue is reported by Ito et al. (43) The Ni–C_{methyl} distance in this low-spin, square-planar complex with an equatorially bound methyl group is 1.96 Å which is similar to A_{Me} (Figure S9b). The ∼0.02 Å discrepancy is within the resolution of the experimental EXAFS measurement and could also reflect the role of the Fe-S cluster which is missing in this reference compound. This small molecule comparison further supports our assignment of A_{Me} as a low-spin Ni_p(II)–Me complex with a square-planar geometry.

Formation of Ni_p(II)–Me presents a conundrum. The Co K-edge XAS and UV–visible experiments (Figures 3-3 and S1) agree with prior transient kinetic studies, which demonstrate generation of Co(I) from methyl-Co(III), (11,44) suggesting a methyl carbocation transfer and generation of Ni_p(III)–Me. However, when we monitor ACS, our results, in agreement with prior stopped-flow and rapid freeze quench EPR studies, (45,46) reveal a diamagnetic Ni_p(II)–Me, which suggests either a methyl radical intermediate or transfer of a methyl cation to a two-electron reduced "Ni_p0" state, as shown in Figure 3-2d. This Ni_p0 state is generally configured as a Ni_p(I)–$[4Fe–4S]^{1+}$ cluster (8) (Figure 3-2c,d) and is inconsistent with the Ni- and Fe-XAS data presented here. We propose an alternative solution to this conundrum: the EC mechanism (Figure 3-2a) in which Ni_p(II)–$[4Fe–4S]^{2+}$ (1′) is coupled to the reaction with methyl-cob(III)inamide in the presence of a reductant (Ti(III)-citrate) to generate an unstable Ni_p(III)–Me intermediate (4) that undergoes immediate reduction by the excess Ti(III)-citrate (required for reductive activation of the A-cluster) forming the stable Ni_p(II)–Me state (4′) that we trap and characterize here. While it is clear that the species that we have trapped is Nip(II)–Me, the UV–vis and XAS data on SN2 reaction between 1′ and Co(III)–Me clearly suggest the formation of a transient, high-potential Ni_p(III)–Me species, which undergoes spontaneous reduction to the trapped Ni_p(II)–Me via reaction with the excess Ti(III)-citrate in solution (note that any excess Ti(III)/Ti(IV) (∼ −500 mV) in solution will not reduce A_{Ox} by two-electrons to invoke the Ni_p0 species (Figure 3-2) in the diamagnetic mechanism). This reaction would also occur within the microbial cell, which is replete with low-potential reductants such as ferredoxin, which is a redox activator for ACS. (47)

To ensure that we had not overlooked the proposal that methylation of ACS occurs on Cys residues laid out by Pezacka and Wood, (48) we reacted ACS with methyl-cob(III)inamide

and examined the product by LC/MS/MS. Pezacka and Wood had reported that reaction of CODH/ACS with ^{14}C-methyl iodide or ^{14}C-methyl-CFeSP led to formation of a $^{14}CH_3$-Cys residue on the β subunit (now known to be CODH) and that this methyl group is converted to acetyl-CoA upon further reaction with CO and CoA. However, as shown in Figure S10, the methylated sample contained a very low level (7/80 peptide reads, 8.8%) of methyl-Cys at residues C509, C528, and C597, which are part of the A-cluster. In addition, Cys and other residues (Lys, Met, Gln, and Asn) underwent methylation in the as-isolated, methylated, and acetylated states. Furthermore, while carbonylation of an active methyl-ACS intermediate would be expected to form acetyl-Cys, there was no evidence for the formation of any acetylated peptides. Lastly, it was the beta subunit (CODH) that had been reported to undergo methylation, not ACS. Thus, our evidence suggests that formation of methyl-Cys is not relevant to the catalytic mechanism of acetyl-CoA synthesis by ACS.

3.3.2 The Acetyl Intermediate

ACS uses a random mechanism for binding CO and methyl to produce the acetylated enzyme, which does not turn over in the absence of CoA, enabling us to generate and trap acetyl-ACS (A_{Ac}) by incubating A_{Me} with CO. (2,5,7,44) While it is tempting to call the trapped Ni_p(II)–Me a reduced, off-cycle species, our data clearly show that this species is capable of reacting with CO to form the trapped Ni_p(II)–Ac intermediate ***3′***. Fe K-edge XAS, EXAFS, and ^{57}Fe-labeled Mössbauer spectra of A_{Me} and A_{Ac} are nearly identical, indicating similar diamagnetic $[4Fe–4S]^{2+}$ clusters (Figures 5b and 6b,d). A small (∼19%) paramagnetic fraction is observed in the ^{57}Fe-labeled Mössbauer for A_{Ac} that can be simulated using the previously reported parameters of species ***2*** (A_{NiFeC}) and is thus attributed to the competitive formation of ∼19% carbonylated A_{NiFeC}, (29) while the other 81% is attributable to A_{Ac} iron. In contrast, clear differences are observed in the Ni K-edge spectra (Figure 3-6a,c). Carbonylation of A_{Me} leads to an increase in intensity at the Ni K-pre-edge and decreased intensity of the rising-edge shoulder (Figure 3-6a), while the rising-edge energy-position of A_{Ac} remains unchanged. These data indicate that A_{Ac} is a Ni_p(II) species similar to A_{Me}. A more dramatic difference between A_{Me} and A_{Ac} is observed in the EXAFS data (Figure 3-6c). Structural fits indicate an increase in the first-shell coordination number; 1.4 in A_{Ac} relative to 1 in A_{Ox} (Figure S11, Table S2). The 1.4 in A_{Ac} is split into 1.0 from Ni-N and 0.4 from the Ni–C_{acetyl} contribution, supporting the addition of a shorter 1.87 Å Ni_p–C_{acetyl} ligand at the Ni_p site and indicating an 80% conversion from A_{Me},

consistent with the Mössbauer analysis. This contrasts with the longer 1.98 Å Ni_p–C_{methyl} bond in A_{Me}. BS DFT calculations indicate that the Ni_p–C_{acetyl} is in the $Ni_p(II)S(Cys)_3$ plane with the acetyl OCO plane perpendicular to the $Ni_p(II)S_3$ plane (Figure 6e–g). The calculated 1.90 Å Ni_p–C_{acetyl} distance is ~0.08 Å shorter than the Ni_p–C_{methyl} of A_{Me} (Table S5), in good agreement with the Ni K-edge XAS data (Table S2). TD-DFT calculations of the Ni pre-edge peak reproduce this change (Figure 3-6a (inset)). These data reveal that carbonylation of A_{Me} forms a square planar acetyl-bound $Ni_p(II)$ intermediate with a short Ni_p–C_{acetyl} bond at 1.87 Å, with insignificant structural or electronic change to the $[4Fe–4S]^{2+}$ cluster. The fact that the diamagnetic $Ni_p(II)$–Me species is catalytically active, binds CO, and forms a $Ni_p(II)$–Ac species is explained through the EC mechanism (see the EC Mechanism discussion below).

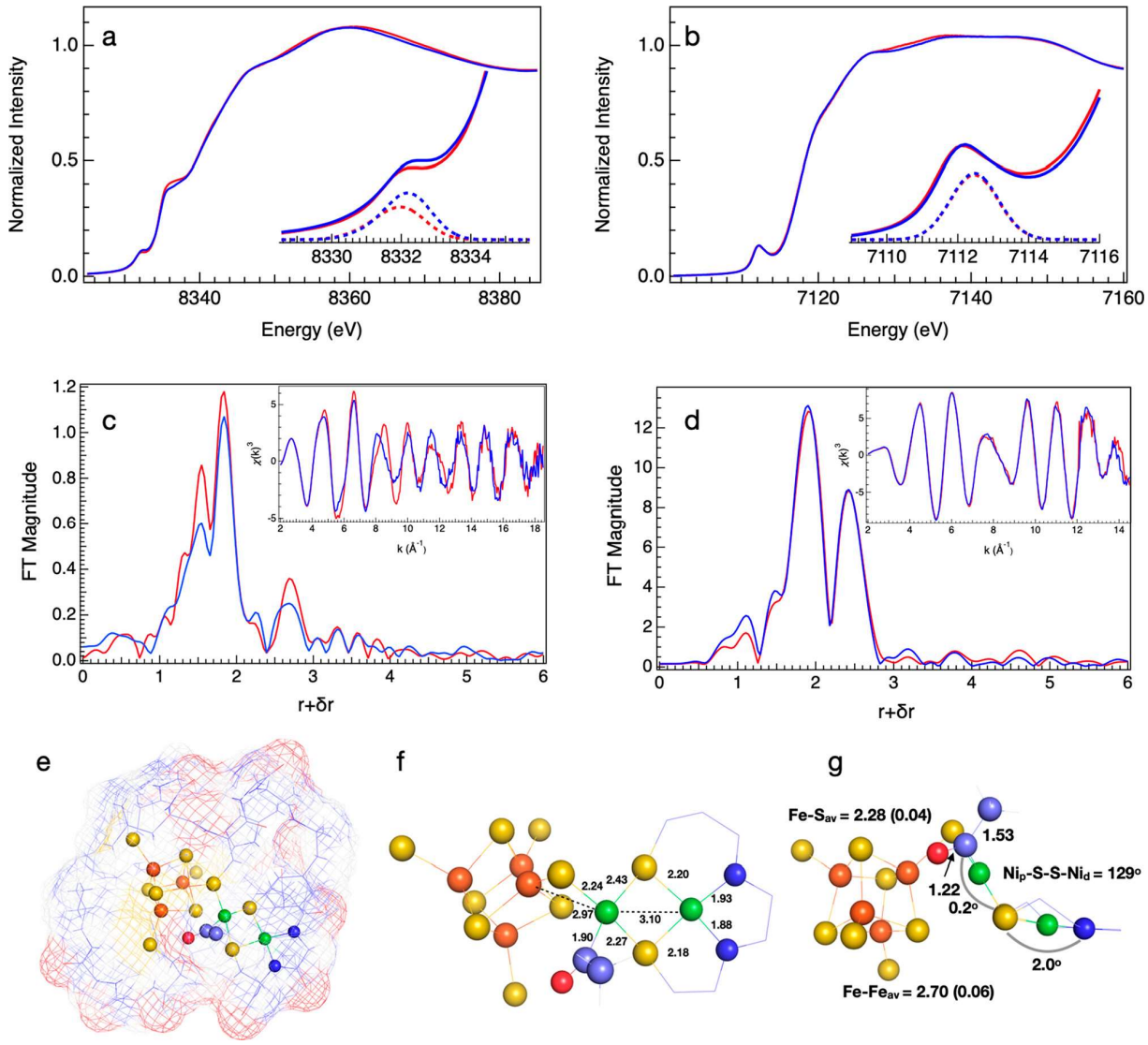

Figure 3-6 Structure of A_{Ac} obtained from XAS and DFT in comparison to A_{Me}. (a) Ni K-edge XAS and (b) Fe K-edge XAS showing changes to the near and rising edge regions upon acetylation of A_{Me} (red lines) to A_{Ac} (blue lines). The insets show the expanded pre-edge region and corresponding TD-DFT calculations (dotted lines). (c) Ni K-edge EXAFS (inset) and (d) Fe K-edge EXAFS (inset) with corresponding Fourier-transforms. (e–g) Calculated structural parameters of the [4Fe–4S]–Ni_p(Ac)–Ni_d active sites of A_{Ac}.

3.4 Discussion

3.4.1 A Delocalized [4Fe-4S]-Ni_p-Ni_d Active Site

The role of the various metal ions in the active site of ACS has remained a subject of debate. (8,10,49) Evidence indicates Ni_p to be the site of substrate binding and catalysis. For example, reductive activation of A_{Ox} in the presence of CO generates a stable Ni_p(I)–CO species (***2***, A_{NiFeC}) in which the organometallic Ni–C bond was observed and characterized by XAS (3) and XRD (4) methods. This species has also been characterized by a variety of static

and time-resolved spectroscopic studies (as reviewed) (10,50) and shown to have a $S = 1/2$, $[4Fe–4S]^{2+}–Ni_p^{1+}(CO)–Ni_d^{2+}$ ground state. While we have been unsuccessful in observing direct reduction of the resting ***1′*** state to ***1*** (A_{red}) using chemical or electrochemical reductants, we and others have successfully obtained the apparent midpoint potential ($E_{app}°′$) for the chemically coupled formation of A_{NiFeC} (***2***) from A_{Ox} (***1′***). These studies were performed with CODH/ACS and ACS in a three-electrode cell containing low-potential mediators and include reaction of CODH/ACS with acetyl-CoA in the absence of CO or CO_2 ($E_{app}°′ = −541$ mV vs SHE (52)), titration of CODH/ACS with CO_2 at varying redox potentials ($E_{cat} = −430$ mV (53)), and measurement of the potential dependence of the CoA/acetyl-CoA exchange reaction for acetogenic and methanogenic CODH/ACS ($E_{cat} = −486$ mV (54,55)). Similarly, we have studied formation of A_{Me} (species *4′*) from the methylated CFeSP ($E_{app}°′ = −450$ mV (56)). Despite the variation of $E_{app}°′$ values, the results are consistent with a model involving the one-electron reductive activation of A_{Ox} (***1′***) coupled to substrate, e.g., CO or methyl binding. As shown in Figure 2c, the computed redox potential for the one-electron ***1′/1*** (Ni_p^{2+}/Ni_p^{1+}) couple is −0.7 V, −1.7 V (***1/1″***) for the one-electron reduction of Ni_p(I) to Ni_p(0) and −1.2 V for the two-electron (***1′/1″***) reduction of A_{Ox} to Ni_p(0). (14)

The consensus electronic configuration of A_{Ox} has a low-spin $[4Fe–4S]^{2+}–Ni_p^{2+}–Ni_d^{2+}$ ground state (Figure 3-2b). (10,14) The $[4Fe\text{-}4S]^{2+}$ cluster participates through spin delocalization to form the $S = 1/2$, Ni_p(I) (***1***) species upon reductive activation, which is required for the initial CO or Me binding. While the Ni is responsible for CO binding, the electronic spin is highly delocalized into the $[4Fe–4S]^{2+}$ cluster and CO, leading to its name, the "A_{NiFeC} intermediate". (3,10) Intermediate ***1*** (A_{red}) in the EC mechanism (Figure 2c) was identified by photolysis of A_{NiFeC} and characterized by EPR, and FTIR experiments to be a very unstable Ni_p(I) species (unlike the stable $S = 1/2$ A_{NiFeC}, which was described by XAS). (3,25) Based on its highly rhombic EPR spectrum ($g = 2.56$, 2.10, and 2.01), it was proposed that the unpaired spin in ***1*** (A_{red}) largely resides on Ni_p, enhancing its reactivity toward CO or cob(III)inamide to generate the highly delocalized intermediates.

While we show that major structural and redox changes occur at Ni_p as the A-cluster transits the catalytic mechanism (Figure 2a), the Ni_d, which is strongly bridged to Ni_p by two S(cys) ligands, putatively plays mostly a structural role, e.g., providing the thiolate ligands to Ni_p. The close alignment of the spectroscopic and DFT data presented here provide an excellent opportunity to

theoretically compare the experimentally accessible Ni_p(II) species, A_{Ox}, A_{Me} (***4′***) and A_{Ac} (***3′***) with the DFT accessible oxidized Ni_p(III) species, ***4*** and ***3***. Methylation of ***1*** leads to ***4***, a formally $S = 1/2$, $[4Fe–4S]^{2+}$–Ni_p(III)–Me)–Ni_d^{2+} ground state, which undergoes rapid reduction to the more stable Ni_p(II)–Me (A_{Me}, ***4′***). (57) The calculations on low-spin ***4*** reveal that the extra hole ($\psi^*_{(LUMO)}$) is delocalized over the entire [4Fe–4S]–Ni_p(Me)–Ni_d framework with partial Hirshfeld spin densities on the [4Fe–4S]$S(Cys)_4$ (0.52), Ni_p(−0.07), and Ni_d (0.22) (Table S10 and Figure S12). Similarly, in the oxidized, formally Ni_p(III)–Ac species ***3***, the ground state wavefunction ($\psi^*_{(LUMO)}$) has contributions from the entire cluster with a majority of spin density residing on the $[4Fe–4S]^{2+}$ cluster (Figure S12). Interestingly, Ni_d has ∼20% spin density in both ***4*** and ***3***, suggesting an important role in dissipating the additional charge on Ni_p (Table S10). While hole delocalization has previously been observed onto the [4Fe–4S] cluster in the A_{NiFeC} (***2***) intermediate, our theoretical results reveal a hitherto unobserved electronic role of the Ni_d site in methylation and acetylation. In this way, Ni_p accumulates very little positive spin density in ***4*** and ***3***. Thus, the unstable Ni_p(I) intermediate ***1*** (Figure 3-2a) is the only ACS intermediate with its single unpaired electron spin density localized on the Ni center. (25)

3.4.2 Role of Second-Sphere Ligands

In the CODH/ACS complex, CO_2 is reduced to CO, which is transported via a 140 Å long hydrophobic tunnel that connects the active sites of these two tightly associated proteins. (12,13) ACS binds to CODH in two distinct conformations. The “closed” site has a buried A-cluster with access to the tunnel, leading to CO approach and binding, while the “open” or “extended” site has a surface accessible A-cluster, poised for CFeSP binding and methyl transfer (Figures S13 and S14). (58,59) Our DFT calculations including second-sphere residues reveal a “gatekeeping” role of the residues in CO and methyl binding. To account for the role of conformational changes in the EC mechanism, the rearrangement of second-sphere residues (especially I146 and F512) not only blocks CO and methyl access in the “closed” and “open” states but also they prevent the A-cluster from assuming tetrahedral (for CO-binding) and square-planar (for methyl-binding) geometries, respectively (Figures S13 and S14). This strategic rearrangement of F512 and I146 in the two conformations shows both a tight control of the physical access of substrates to the active site and the ability to achieve the geometric and electronic structures necessary to bind the substrates. We thus acknowledge that the EC mechanism could also be called a CEC mechanism to account for these conformational controls.

3.4.3 Comparison to the Ni-Azurin Model

In recent studies, a novel Ni-Azurin (Ni-Az) construct of the A-cluster Ni_p site has been developed and used to gain insights into CO and methyl binding by ACS. (60) The active site in Ni-Az differs from ACS in three important aspects: (a) it is not catalytic, (b) it lacks the [4Fe–4S]$^{2+}$ cluster and Ni_d of ACS, and (c) methylation occurs along the molecular *z*-axis, leading to a high-spin tetrahedral Ni–Me intermediate. Despite these differences, both ACS and M121A Ni azurin form unstable, formally Ni(III)–Me species. In Ni-Az, the Ni(III)–Me intermediate quickly reduces to Ni(II)–Me. (60) Potentiometric titrations demonstrate a high Ni(III)/(II) redox potential in Ni-Az (> +0.8 V). (61) However, in ACS, only the reduced methyl-Ni_p(II) species, A_{Me} (***4'***), is experimentally observed, likely because ACS methylation requires reductive activation at potentials in the < −400 mV range which quickly reduces the high potential methyl-Ni_p(III) (***4***) species. Chemically coupling carbonylation to form acetyl-Ni could recruit the higher valent formally Ni(III)–Me to form the acetyl-Ni product. Interestingly, the high-valent formally Ni(III)–Me Ni-Az was shown to be a d^9 Ni(I) instead of a d^7 Ni(III) ground state. (61) For ACS, we show using theoretical calculations that in the formally Ni_p(III)–Me species (***4***), the additional hole is delocalized away from the Ni_p and across the [4Fe–4S]$^{2+}$ cluster and the Ni_d site. Thus, in both systems, a high valent Ni(III)–Me intermediate is quickly quenched to Ni(II)–Me.

The Ni K-edge data further highlight the differences between the two systems. In their recent study of the Ni-Azurin model, Manesis et al. present Ni K-edge XAS data of the methyl and acetyl-bound Ni(II)-azurin model that differs substantially from the data of A_{Me} and A_{Ac} presented here. (62) The spectra of the Ni azurin model lack the edge feature at 8355.2 eV which is indicative of the near square planar geometry of the two Ni sites present in ACS. This feature sharpens into a shoulder upon methylation and acetylation in ACS due to increasing planarity at the Ni_p site. Additionally, the presence of the distal nickel site in ACS confers ∼50% of the intensity of this feature as the site remains square planar throughout the catalytic cycle. In contrast, the acetylated state of the Ni(II)-azurin model was found to be trigonal pyramidal, which does not give rise to this feature. Manesis et al. also performed theoretical calculations of the azurin Ni(II)-acetyl model in high- (s = 1) and low-spin (s = 0) configurations and found that the low-spin model converged to a square planar Ni(II) geometry, while the high-spin model converged to a trigonal pyramidal geometry. Comparison with their Ni K-edge EXAFS data revealed that the trigonal pyramidal, high-spin configuration was more consistent with their data,

while the low-spin configuration yielded Ni–L bond lengths that were too short. Such differences between the Ni-azurin model and ACS are key and serve to obfuscate any direct mechanistic comparisons between the two systems.

3.4.4 The EC mechanism

Our spectroscopic results offer important insights into the electronic properties of these intermediates. We have shown that the methyl- and acetyl-Ni_p sites are embedded within a highly delocalized system, containing 5 other metals (another Ni and a Fe_4S_4 cluster) and that they are isolated in the Ni_p(II) state. This is an interesting finding, given the debate surrounding the so-called paramagnetic versus the diamagnetic mechanism: the former involving an active one-electron reduced the Ni_p(I) (Ni_p(I)–Ni_d(II)–$[Fe_4S_4]^{2+}$) state and the latter a two-electron active "Ni_p^0" form, often formulated as Ni_p(I)–Ni_d(II)–$[Fe_4S_4]^{1+}$. (7,8,14,44) In the diamagnetic mechanism, the Ni_p^0 state reacts with the CH_3^+ of the methylated CFeSP to generate Ni_p(II)–Me, which subsequently undergoes carbonylation to generate Ni_p(II)–Ac. In favor of the paramagnetic mechanism, our photolysis experiments confirmed the formation of the Ni_p(I) species ***1***, (25) and our previous XAS data confirm a Ni_p(I)-CO ground state in ***2***. (3)

The formation of the Ni_p(II)–Me and Ni_p(II)–Ac states under reducing conditions leads us to develop the electrochemical coupling mechanism that we propose in Figure 3-2, which not only provides a novel conceptual framework that supports the paramagnetic mechanism but also includes intermediates proposed in the diamagnetic mechanism. The solution we favor (as shown in Figure 3-2a) is that Ni_p(I) (or Ni_p(I)–CO) reacts with methyl-Co(III) to generate Ni_p(III)–Me (or Ni_p(III)–Ac), respectively, which can undergo rapid reduction to Ni_p(II). The EC mechanism then recruits these Ni_p(III) states back into the catalytic cycle. For the Ni_p(II)–Ac state, this coupled reaction would regenerate the (Ni_p(I)–Ni_d(II)–$[Fe_4S_4]^{2+}$ state for the next catalytic cycle.

Furthermore, our BS DFT results on the experimentally inaccessible Ni_p(III)–Me and Ni_p(III)–Ac states, ***4*** and ***3*** in the EC mechanism (Figure 3-2) reveal their unique and delocalized electronic structures. In both cases, most of the unpaired electron spin resides on the [4Fe–4S]$^{2+}$ and the Ni_d sites of the A-cluster. The movement of the positive charge away from Ni_p is crucial. Recent studies of this pathway using Ni-azurin indicated that carbonylation of Ni_p(III)–Me is highly unfavorable and that reduction to the Ni_p(II)–Me state was necessary to form Ni_p(II)–Ac. (62,63) While this reduction was required in Ni-azurin, ACS is cleverly designed to delocalize the charge away from Ni_p in the formally Ni(III) state ***4***, such that it is best described

as Ni_p(II) poised for carbonyl insertion into the Ni–Me bond. Thus, the EC mechanism is a hybrid paramagnetic (involving Ni_p(I), and Ni_p(I)–CO) and diamagnetic (involving methyl and acetyl Ni_p(II) states) mechanism. Which state is observed depends on the redox poise of the solution. A labile Ni_p(III)–Me or −Ac, with a redox potential in the range of +800 mV would be too oxidizing, that is, too transient to observe in a solution in the low potential environment of the anaerobic microbial cell or in the biochemical reaction, which requires low potential reductants. (47)

There is one other likely intermediate in the pathway. When CO binds to A_{Me} (or when Me binds to A_{NiFeC}), we expect to form a transient intermediate where Me and CO are directly coordinated to Ni_p, i.e., Ni_p(Me)(CO). The formation of this intermediate is required to explain the ACS-catalyzed exchange reaction between CO and CH_3-^{14}CO-CoA. (2) Thus, CO binds to A_{Me} (***4′***) forming Ni_p(II)(Me)(CO), which would then lose an electron to form Ni_p(III)(Me)(CO), promoting C–C bond formation.

Besides the complex electronic and spin delocalization requirements for ACS, the A cluster undergoes major changes as Ni_p transits the spectroscopically accessible states: resting planar Ni_p(II) (A_{Ox}, ***1′***), tetrahedral Ni_p(I)–CO (A_{NiFeC}, ***2***), planar Ni_p(II)–Me (A_{Me}, ***4′***), Ni_p(II)–Ac (A_{Ac}, ***3′***), and the DFT-accessible states: transient, oxidized, highly delocalized methyl and acetyl Ni_p states (***4*** and ***3***, respectively). The planar to tetrahedral geometric changes in Ni_p also appear to be coupled to large-scale conformational changes in ACS. (58) Another important feature of this pathway is that reaction of ACS with both CO and methyl-Co(III) require reductive activation of A_{Ox}. The Ni_p(I) state of ACS has only been generated by photolysis of the Ni_p(I)–CO (A_{NiFeC}), (25) supporting the EC mechanism in which the reduction of Ni_p(II) to the unstable Ni_p(I) state is coupled to carbonylation (Species ***1*** → ***1′*** → ***2*** in Figure 3-2). (10) This reaction could also be called a CEC reaction, given that there is both conformational and chemical coupling to the electrochemical reduction. The source of the electron used in the reduction of Ni_p is unknown; however, the subsequent reaction of A_{Ac} with CoA to generate and release acetyl-CoA would lead to two-electron reduction of the cluster, which appears to be stored for the next round of catalysis. We propose a similar EC mechanism for methylation, where Ni_p achieves an electronic state similar to Ni_p(I) for nucleophilic attack on the cobinamide-bound methyl group. Thus, according to this mechanism, the formation of transient intermediates ***1***, ***3***, and ***4*** is coupled to substrate binding.

3.5 Conclusions

Here, we have described our significant and successful efforts to validate the hypothesis that the WLP of anaerobic CO_2 fixation occurs through organometallic Ni–Me and Ni–Ac species. Over the past three decades, we and others have tried many methods to unambiguously observe these Ni–carbon bonds. Our successful strategy presented in this manuscript required developing an expression and reactivation system that yields a highly active and sufficiently homogeneous state of ACS to offer unambiguous identification of the electronic states of these organometallic species using multi-element XAS. This breakthrough validates the most unique feature of the WLP that it occurs through a series of organonickel intermediates, akin to the Monsanto industrial process for acetic acid synthesis. This validation is crucial because it substantiates the figures presented in textbooks and hundreds of chemistry, biochemistry, and microbiology publications and justifies the efforts by bioinorganic chemists to model these Ni–carbon species. We have characterized the electronic properties of each of the species that we trapped. It remains to be determined whether these are the true catalytic intermediates, as depicted in the diamagnetic mechanism, or stable species in equilibrium with unstable transient species (whose properties we determine by computational methods) that enter the catalytic cycle by the paramagnetic mechanism suggested in Figure 3-2a. These studies significantly enhance our understanding of the unique organometallic nature of the WLP for converting carbon dioxide into the key metabolic precursor, acetyl-CoA, and reveal that a nucleophilic mechanism is responsible for the formation of A_{Me} in ACS, where comparable organometallic mechanisms have been ruled out in the related Ni enzyme methyl-CoM reductase in favor of a methyl radical model. (64)

Further studies of these Ni-based intermediates are expected to reveal how the structure and dynamics of ACS and its active site are finely tuned to promote the ACS mechanism. Both ACS and CODH are exquisitely designed systems that utilize large conformational changes and interprotein channels for fastidious delivery of substrates. ACS interacts with partner proteins (CODH and the CFeSP) and undergoes redox transitions during its enzymatic reaction, which overall is a redox-neutral process. We lack a structure of the ACS–CFeSP complex, which should reveal the Co–CH_3–Ni orientation during methyl group binding and help explain this metal-to-metal methyl transfer reaction. While the structures of A_{NiFeC}, A_{Me}, and A_{Ac} have now been revealed, we do not yet know how CoA binds to ACS. We also do not know how the

electrons released from the thiolytic cleavage of the Ni–Ac group are coupled to reductive activation of the A-cluster, allowing it to re-enter the catalytic cycle by binding CO or methyl groups.

The CODH and ACS reactions are the key steps in the WLP, a significant component of the global carbon cycle. The WLP also is being used in biotechnological applications. Thus, CODH/ACS and the WLP form a biological carbon capture and utilization machine that could be used to reduce the levels of CO_2 in the atmosphere. Developing a better understanding of the ACS reaction and what factors regulate it may lead to strategies to optimize, regulate, and perhaps stimulate CO_2 uptake helping lead us toward a carbon neutral (or negative) energy economy and help mitigate the effects of climate change.

3.6 Materials and Methods

ACS was prepared, purified and Ni-reconstituted as previously described.3 Methylated ACS was prepared using Ti(III)-citrate and methyl-Cob(III)inamide and monitored at the 390 nm Cob(I)inamide absorption band in a parallel UV-Vis experiment. Acetylated ACS was prepared via incubation of methyl-ACS with ultra-high-purity CO. All XAS measurements were collected cryostat on beamline 7-3 at the Stanford Synchrotron Radiation Lightsource. A liquid He cryostat was employed to minimize radiation damage to the samples. Demeter v9.26 and EXAFSPAK were used to process, normalize, and fit the XAS data. Theoretical calculations were conducted using Orca 3.0.3 and made use of the BP86 local functional and Ahlrich's all electron triple-ζ basis sets (TZVPP on Ni and TZVP on all other atoms). Mössbauer spectra were collected on a home-built system using a Janis Research SuperVaritemp dewar and LakeShore Model 331 A temperature controller and a 0.045 T permanent magnet. EPR and ENDOR (35 GHz) spectra were collected as continuous wave measurements with a 100 kHz field modulation. Additional, detailed information on all reagents, sample preparation, experimental procedures and analytical techniques employed are provided in the SI.

Note: The supplemental information (SI) for this publication is available at https://doi-org.proxy.lib.umich.edu/10.1021/jacs.3c01772

3.7 Author contributions

The manuscript was written through contributions of all authors. All authors have given approval to the final version of the manuscript.

As an author on this manuscript, I made one of the three sets of XAS samples and provided UV-visible absorbance data of the samples to directly demonstrate methylation had occurred and quantify it. I wrote the methods sections related to my experiment, and made a figure related to the methylation data and participated in the review process.

Funding Sources

Department of Energy-Basic Energy Sciences Field Work Proposal 100593 (R.S)

National Institutes of Health grant GM125924 (Y.G.)

National Institutes of Health grant R35-GM141758 (S.W.R.)

The Stanford Synchrotron Radiation Lightsource is supported by the U.S. Department of Energy Office of Basic Energy Science under Contract No. DE- AC02-76SF00515

Competing Interests: The authors declare that they have no competing interests.

3.8 Attributions

Mehmet Can[1], Macon J. Abernathy[2], Seth Wiley[3], Claire Griffith[4], Christopher D. James[5], Jin Xiong[6], Yisong Guo[6], Brian M. Hoffman[5], Stephen W. Ragsdale[4]*, and Ritimukta Sarangi[2]*

1 Department of Biochemistry, Faculty of Pharmacy, Ankara Medipol University, Ankara, Turkey

2 Stanford Synchrotron Radiation Lightsource, SLAC National Accelerator Laboratory; Menlo Park, CA 94025, USA.

3 Biosciences Center, National Renewable Energy Laboratory, Golden, CO 80401

4 Department of Biological Chemistry, University of Michigan; Ann Arbor, MI 48109, USA.

5 Department of Chemistry, Northwestern University; Evanston, IL 60208, USA.

6 Department of Chemistry, Carnegie Mellon University; Pittsburgh, PA 15213, USA

3.9 References for Chapter 3

1. Weiss, M. C.; Sousa, F. L.; Mrnjavac, N.; Neukirchen, S.; Roettger, M.; Nelson-Sathi, S.; Martin, W. F. The Physiology and Habitat of the Last Universal Common Ancestor. *Nat. Microbiol.* **2016**, *1*, 16116, DOI: 10.1038/nmicrobiol.2016.116
2. Ragsdale, S. W.; Wood, H. G. Acetate Biosynthesis by Acetogenic Bacteria: Evidence That Carbon Monoxide Dehydrogenase Is the Condensing Enzyme That Catalyzes the Final Steps of the Synthesis. *J. Biol. Chem.* **1985**, *260*, 3970– 3977, DOI: 10.1016/S0021-9258(18)89217-1
3. Can, M.; Giles, L. J.; Ragsdale, S. W.; Sarangi, R. X-Ray Absorption Spectroscopy Reveals an Organometallic Ni–C Bond in the CO-Treated Form of Acetyl-CoA Synthase. *Biochemistry* **2017**, *56*, 1248– 1260, DOI: 10.1021/acs.biochem.6b00983
4. Cohen, S. E.; Can, M.; Wittenborn, E. C.; Hendrickson, R. A.; Ragsdale, S. W.; Drennan, C. L. Crystallographic Characterization of the Carbonylated A-Cluster in Carbon Monoxide Dehydrogenase/Acetyl-CoA Synthase. *ACS Catal.* **2020**, *10*, 9741– 9746, DOI: 10.1021/acscatal.0c03033
5. Seravalli, J.; Ragsdale, S. W. Pulse-Chase Studies of the Synthesis of Acetyl-CoA by Carbon Monoxide Dehydrogenase/Acetyl-CoA Synthase. *J. Biol. Chem.* **2008**, *283*, 8384– 8394, DOI: 10.1074/jbc.M709470200
6. Gencic, S.; Kelly, K.; Ghebreamlak, S.; Duin, E. C.; Grahame, D. A. Different Modes of Carbon Monoxide Binding to Acetyl-CoA Synthase and the Role of a Conserved Phenylalanine in the Coordination Environment of Nickel. *Biochemistry* **2013**, *52*, 1705– 1716, DOI: 10.1021/bi3016718
7. Tan, X.; Surovtsev, I. V.; Lindahl, P. A. Kinetics of CO Insertion and Acetyl Group Transfer Steps, and a Model of the Acetyl-CoA Synthase Catalytic Mechanism. *J. Am. Chem. Soc.* **2006**, *128*, 12331– 12338, DOI: 10.1021/ja0627702
8. Lindahl, P. A. Acetyl-Coenzyme A Synthase: The Case for a Nip0-Based Mechanism of Catalysis. *J. Biol. Inorg. Chem.* **2004**, *9*, 516– 524, DOI: 10.1007/s00775-004-0564-x
9. Yoo, C.; Miller, A. J. M. Stepwise Iodide-Free Methanol Carbonylation via Methyl Acetate Activation by Pincer Iridium Complexes. *J. Am. Chem. Soc.* **2021**, *143*, 12633– 12643, DOI: 10.1021/jacs.1c05185

10. Ragsdale, S. W. Biological Carbon Fixation by an Organometallic Pathway: Evidence Supporting the Paramagnetic Mechanism of the Nickel-Iron-Sulfur Acetyl-CoA Synthase. In *Reference Module in Chemistry, Molecular Sciences and Chemical Engineering*; Elsevier, 2021.
11. Seravalli, J.; Brown, K. L.; Ragsdale, S. W. Acetyl Coenzyme A Synthesis from Unnatural Methylated Corrinoids: Requirement for "Base-Off" Coordination at Cobalt. *J. Am. Chem. Soc.* **2001**, *123*, 1786– 1787, DOI: 10.1021/ja005709k
12. Doukov, T. I.; Blasiak, L. C.; Seravalli, J.; Ragsdale, S. W.; Drennan, C. L. Xenon in and at the End of the Tunnel of Bifunctional Carbon Monoxide Dehydrogenase/Acetyl-CoA Synthase. *Biochemistry* **2008**, *47*, 3474– 3483, DOI: 10.1021/bi702386t
13. Doukov, T. I.; Iverson, T. M.; Seravalli, J.; Ragsdale, S. W.; Drennan, C. L. A Ni-Fe-Cu Center in a Bifunctional Carbon Monoxide Dehydrogenase/Acetyl-CoA Synthase. *Science* **2002**, *298*, 567– 572, DOI: 10.1126/science.1075843
14. Chmielowska, A.; Lodowski, P.; Jaworska, M. Redox Potentials and Protonation of the A-Cluster from Acetyl-CoA Synthase. A Density Functional Theory Study. *J. Phys. Chem. A* **2013**, *117*, 12484– 12496, DOI: 10.1021/jp402616e
15. Sarangi, R.; DeBeer George, S.; Rudd, D. J.; Szilagyi, R. K.; Ribas, X.; Rovira, C.; Almeida, M.; Hodgson, K. O.; Hedman, B.; Solomon, E. I. Sulfur K-Edge X-Ray Absorption Spectroscopy as a Probe of Ligand–Metal Bond Covalency: Metal vs Ligand Oxidation in Copper and Nickel Dithiolene Complexes. *J. Am. Chem. Soc.* **2007**, *129*, 2316– 2326, DOI: 10.1021/ja0665949
16. Szilagyi, R. K.; Lim, B. S.; Glaser, T.; Holm, R. H.; Hedman, B.; Hodgson, K. O.; Solomon, E. I. Description of the Ground State Wave Functions of Ni Dithiolenes Using Sulfur K-Edge X-Ray Absorption Spectroscopy. *J. Am. Chem. Soc.* **2003**, *125*, 9158– 9169, DOI: 10.1021/ja029806k
17. Colpas, G. J.; Maroney, M. J.; Bagyinka, C.; Kumar, M.; Willis, W. S.; Suib, S. L.; Mascharak, P. K.; Baidya, N. X-Ray Spectroscopic Studies of Nickel Complexes, with Application to the Structure of Nickel Sites in Hydrogenases. *Inorg. Chem.* **1991**, *30*, 920– 928, DOI: 10.1021/ic00005a010

18. Sarangi, R. X-Ray Absorption near-Edge Spectroscopy in Bioinorganic Chemistry: Application to M–O2 Systems. *Coord. Chem. Rev.* **2013**, *257*, 459– 472, DOI: 10.1016/j.ccr.2012.06.024
19. Gu, W.; Wang, H.; Wang, K. Extended X-Ray Absorption Fine Structure and Multiple-Scattering Simulation of Nickel Dithiolene Complexes Ni[S2C2(CF3)2]2(n) (n = −2, −1, 0) and an Olefin Adduct Ni[S2C2(CF3)2]2(1-Hexene). *J. Synchrotron Radiat.* **2015**, *22*, 124– 129, DOI: 10.1107/S1600577514025041
20. Schrapers, P.; Ilina, J.; Gregg, C. M.; Mebs, S.; Jeoung, J. H.; Dau, H.; Dobbek, H.; Haumann, M. Ligand Binding at the A-Cluster in Full-Length or Truncated Acetyl-CoA Synthase Studied by X-Ray Absorption Spectroscopy. *PLoS One* **2017**, *12*, e0171039 DOI: 10.1371/journal.pone.0171039
21. Cho, J.; Sarangi, R.; Annaraj, J.; Kim, S. Y.; Kubo, M.; Ogura, T.; Solomon, E. I.; Nam, W. Geometric and Electronic Structure and Reactivity of a Mononuclear "side-on" Nickel(Iii)–Peroxo Complex. *Nat. Chem.* **2009**, *1*, 568– 572, DOI: 10.1038/nchem.366
22. Ray, K.; Debeer George, S.; Solomon, E. I.; Wieghardt, K.; Neese, F. Description of the Ground-State Covalencies of the Bis(Dithiolato) Transition-Metal Complexes from X-Ray Absorption Spectroscopy and Time-Dependent Density-Functional Calculations. *Chem. – Eur. J.* **2007**, *13*, 2783– 2797, DOI: 10.1002/chem.200601425
23. Shearer, J.; Soh, P. Ni K-Edge XAS Suggests That Coordination of Ni(II) to the Unstructured Amyloidogenic Region of the Human Prion Protein Produces a Ni(2) Bis-Mu-Hydroxo Dimer. *J. Inorg. Biochem.* **2007**, *101*, 370– 373, DOI: 10.1016/j.jinorgbio.2006.09.032
24. Yang, N.; Reiher, M.; Wang, M.; Harmer, J.; Duin, E. C. Formation of a Nickel-Methyl Species in Methyl-Coenzyme m Reductase, an Enzyme Catalyzing Methane Formation. *J. Am. Chem. Soc.* **2007**, *129*, 11028– 11029, DOI: 10.1021/ja0734501
25. Bender, G.; Stich, T. A.; Yan, L.; Britt, R. D.; Cramer, S. P.; Ragsdale, S. W. Infrared and EPR Spectroscopic Characterization of a Ni(I) Species Formed by Photolysis of a Catalytically Competent Ni(I)-CO Intermediate in the Acetyl-CoA Synthase Reaction. *Biochemistry* **2010**, *49*, 7516– 7523, DOI: 10.1021/bi1010128
26. Ragsdale, S. W.; Lindahl, P. A.; Münck, E. Mössbauer, EPR, and Optical Studies of the Corrinoid/Iron-Sulfur Protein Involved in the Synthesis of Acetyl Coenzyme A by

Clostridium Thermoaceticum. *J. Biol. Chem.* **1987**, *262*, 14289– 14297, DOI: 10.1016/S0021-9258(18)47936-7

27. Stich, T. A.; Seravalli, J.; Venkateshrao, S.; Spiro, T. G.; Ragsdale, S. W.; Brunold, T. C. Spectroscopic Studies of the Corrinoid/Iron–Sulfur Protein from *Moorella Thermoacetica*. *J. Am. Chem. Soc.* **2006**, *128*, 5010– 5020, DOI: 10.1021/ja054690o
28. Panagiotidis, P.; Kefalas, E. T.; Raptopoulou, C. P.; Terzis, A.; Mavromoustakos, T.; Salifoglou, A. Delving into the Complex Picture of Ti(IV)–Citrate Speciation in Aqueous Media: Synthetic, Structural, and Electrochemical Considerations in Mononuclear Ti(IV) Complexes Containing Variably Deprotonated Citrate Ligands. *Inorg. Chim. Acta* **2008**, *361*, 2210– 2224, DOI: 10.1016/j.ica.2007.11.015
29. Bramlett, M. R.; Stubna, A.; Tan, X.; Surovtsev, I. V.; Munck, E.; Lindahl, P. A. Mossbauer and EPR Study of Recombinant Acetyl-CoA Synthase from Moorella Thermoacetica. *Biochemistry* **2006**, *45*, 8674– 8685, DOI: 10.1021/bi060003+
30. Tan, X.; Martinho, M.; Stubna, A.; Lindahl, P. A.; Munck, E. Mossbauer Evidence for an Exchange-Coupled {[Fe4S4]1+ Nip1+} A-Cluster in Isolated Alpha Subunits of Acetyl-Coenzyme A Synthase/Carbon Monoxide Dehydrogenase. *J. Am. Chem. Soc.* **2008**, *130*, 6712– 6713, DOI: 10.1021/ja801981h
31. Rees, J. A.; Bjornsson, R.; Kowalska, J. K.; Lima, F. A.; Schlesier, J.; Sippel, D.; Weyhermüller, T.; Einsle, O.; Kovacs, J. A.; DeBeer, S. Comparative Electronic Structures of Nitrogenase FeMoco and FeVco. *Dalton Trans.* **2017**, *46*, 2445– 2455, DOI: 10.1039/C7DT00128B
32. Szilagyi, R. K.; Winslow, M. A. On the Accuracy of Density Functional Theory for Iron─Sulfur Clusters. *J. Comput. Chem.* **2006**, *27*, 1385– 1397, DOI: 10.1002/jcc.20449
33. Dey, A.; Roche, C. L.; Walters, M. A.; Hodgson, K. O.; Hedman, B.; Solomon, E. I. Sulfur K-Edge XAS and DFT Calculations on [Fe4S4]2+ Clusters: Effects of H-Bonding and Structural Distortion on Covalency and Spin Topology. *Inorg. Chem.* **2005**, *44*, 8349– 8354, DOI: 10.1021/ic050981m
34. Dey, A.; Peng, Y.; Broderick, W. E.; Hedman, B.; Hodgson, K. O.; Broderick, J. B.; Solomon, E. I. S K-Edge XAS and DFT Calculations on SAM Dependent Pyruvate Formate-Lyase Activating Enzyme: Nature of Interaction between the Fe4S4 Cluster and

SAM and Its Role in Reactivity. *J. Am. Chem. Soc.* **2011**, *133*, 18656– 18662, DOI: 10.1021/ja203780t

35. Era, I.; Kitagawa, Y.; Yasuda, N.; Kamimura, T.; Amamizu, N.; Sato, H.; Cho, K.; Okumura, M.; Nakano, M. Theoretical Study on Redox Potential Control of Iron-Sulfur Cluster by Hydrogen Bonds: A Possibility of Redox Potential Programming. *Molecules* **2021**, *26*, 6129, DOI: 10.3390/molecules26206129
36. Khalil, M.; Marcus, M. A.; Smeigh, A. L.; McCusker, J. K.; Chong, H. H. W.; Schoenlein, R. W. Picosecond X-Ray Absorption Spectroscopy of a Photoinduced Iron(II) Spin Crossover Reaction in Solution. *J. Phys. Chem. A* **2006**, *110*, 38– 44, DOI: 10.1021/jp055002q
37. Wilson, S. A.; Green, E.; Mathews, I. I.; Benfatto, M.; Hodgson, K. O.; Hedman, B.; Sarangi, R. X-Ray Absorption Spectroscopic Investigation of the Electronic Structure Differences in Solution and Crystalline Oxyhemoglobin. *Proc. Natl. Acad. Sci. U. S. A.* **2013**, *110*, 16333– 16338, DOI: 10.1073/pnas.1315734110
38. Bianconi, A.; Dell'Ariccia, M.; Gargano, A.; Natoli, C. R. Bond Length Determination Using XANES. In *EXAFS and Near Edge Structure*; Bianconi, A., Incoccia, L., Stipcich, S., Eds.; Springer Series in Chemical Physics; Springer: Berlin, Heidelberg, 1983; pp 57– 61.
39. *EXAFS and Near Edge Structure III: Proceedings of an International Conference, Stanford, CA, July 16–20, 1984*; Hodgson, K. O., Hedman, B., Penner-Hahn, J. E., Eds.; Springer Proceedings in Physics; Springer Berlin Heidelberg: Berlin, Heidelberg, 1984; Vol. 2.
40. Keegan, B. C.; Ocampo, D.; Shearer, J. PH Dependent Reversible Formation of a Binuclear Ni2 Metal-Center within a Peptide Scaffold. *Inorganics* **2019**, *7*, 90, DOI: 10.3390/inorganics7070090
41. Rosenfield, S. G.; Armstrong, W. H.; Mascharak, P. K. Convenient Synthesis and Properties of (R4N)2[Ni(SAr)4] (Ar = C6H5, p-C6H4Cl, p-C6H4CH3, and m-C6H4Cl) and the Structure of Tetraethylammonium Tetrakis(p-Chlorobenzenethiolato)Nickelate(II). *Inorg. Chem.* **1986**, *25*, 3014– 3018, DOI: 10.1021/ic00237a018

42. Baidya, N.; Mascharak, P. K.; Stephan, D. W.; Campagna, C. F. Mononuclear Nickel(II) Thiolates of Square-Planar Geometry: Syntheses, Spectral and Redox Properties of [Ni(SCH2CH2S)2]2– and [Ni(SCH(CH3)CH(CH3)S)2]2– and the Structure of (Ph4P)2[Ni(SCH2CH2S)2]·4H2O. *Inorg. Chim. Acta* **1990**, *177*, 233– 238, DOI: 10.1016/S0020-1693(00)85981-2
43. Ito, M.; Kotera, M.; Matsumoto, T.; Tatsumi, K. Dinuclear Nickel Complexes Modeling the Structure and Function of the Acetyl CoA Synthase Active Site. *Proc. Natl. Acad. Sci. U. S. A.* **2009**, *106*, 11862– 11866, DOI: 10.1073/pnas.0900433106
44. Gencic, S.; Grahame, D. A. Two Separate One-Electron Steps in the Reductive Activation of the A Cluster in Subunit Beta of the ACDS Complex in Methanosarcina Thermophila. *Biochemistry* **2008**, *47*, 5544– 5555, DOI: 10.1021/bi7024035
45. Barondeau, D. P.; Lindahl, P. A. Methylation of Carbon Monoxide Dehydrogenase from Clostridium Thermoaceticum and Mechanism of Acetyl Coenzyme A Synthesis. *J. Am. Chem. Soc.* **1997**, *119*, 3959– 3970, DOI: 10.1021/ja963597k
46. Seravalli, J.; Kumar, M.; Ragsdale, S. W. Rapid Kinetic Studies of Acetyl-CoA Synthesis: Evidence Supporting the Catalytic Intermediacy of a Paramagnetic NiFeC Species in the Autotrophic Wood–Ljungdahl Pathway. *Biochemistry* **2002**, *41*, 1807– 1819, DOI: 10.1021/bi011687i
47. Bender, G.; Ragsdale, S. W. Evidence That Ferredoxin Interfaces with an Internal Redox Shuttle in Acetyl-CoA Synthase during Reductive Activation and Catalysis. *Biochemistry* **2011**, *50*, 276– 286, DOI: 10.1021/bi101511r
48. Pezacka, E.; Wood, H. G. Acetyl-CoA Pathway of Autotrophic Growth. Identification of the Methyl-Binding Site of the CO Dehydrogenase. *J. Biol. Chem.* **1988**, *263*, 16000– 16006, DOI: 10.1016/S0021-9258(18)37548-3
49. Ragsdale, S. W.; Pierce, E. Acetogenesis and the Wood–Ljungdahl Pathway of CO2 Fixation. *Biochim. Biophys. Acta, Proteins Proteomics* **2008**, *1784*, 1873– 1898, DOI: 10.1016/j.bbapap.2008.08.012
50. Can, M.; Armstrong, F. A.; Ragsdale, S. W. Structure, Function, and Mechanism of the Nickel Metalloenzymes, CO Dehydrogenase, and Acetyl-CoA Synthase. *Chem. Rev.* **2014**, *114*, 4149– 4174, DOI: 10.1021/cr400461p

51. James, C.; Wiley, S.; Ragsdale, S. W.; Hoffman, B. M. 13C Electron Nuclear Double Resonance Spectroscopy Shows Acetyl-CoA Synthase Binds Two Substrate CO in Multiple Binding Modes and Reveals the Importance of a CO-Binding "Alcove.". *J. Am. Chem. Soc.* **2020**, *142*, 15362– 15370, DOI: 10.1021/jacs.0c05950
52. Gorst, C. M.; Ragsdale, S. W. Characterization of the NiFeCO Complex of Carbon Monoxide Dehydrogenase as a Catalytically Competent Intermediate in the Pathway of Acetyl-Coenzyme A Synthesis. *J. Biol. Chem.* **1991**, *266*, 20687– 20693, DOI: 10.1016/S0021-9258(18)54763-3
53. Lindahl, P. A.; Münck, E.; Ragsdale, S. W. CO Dehydrogenase from Clostridium Thermoaceticum. EPR and Electrochemical Studies in CO2 and Argon Atmospheres. *J. Biol. Chem.* **1990**, *265*, 3873– 3879, DOI: 10.1016/S0021-9258(19)39675-9
54. Lu, W. P.; Ragsdale, S. W. Reductive Activation of the Coenzyme A/Acetyl-CoA Isotopic Exchange Reaction Catalyzed by Carbon Monoxide Dehydrogenase from Clostridium Thermoaceticum and Its Inhibition by Nitrous Oxide and Carbon Monoxide. *J. Biol. Chem.* **1991**, *266*, 3554– 3564, DOI: 10.1016/S0021-9258(19)67831-2
55. Bhaskar, B.; DeMoll, E.; Grahame, D. A. Redox-Dependent Acetyl Transfer Partial Reaction of the Acetyl-CoA Decarbonylase/Synthase Complex: Kinetics and Mechanism. *Biochemistry* **1998**, *37*, 14491– 14499, DOI: 10.1021/bi9812423
56. Lu, W. P.; Harder, S. R.; Ragsdale, S. W. Controlled Potential Enzymology of Methyl Transfer Reactions Involved in Acetyl-CoA Synthesis by CO Dehydrogenase and the Corrinoid/Iron-Sulfur Protein from Clostridium Thermoaceticum. *J. Biol. Chem.* **1990**, *265*, 3124– 3133, DOI: 10.1016/S0021-9258(19)39743-1
57. DFT Calculations on the oxidized Ni_p(III)–Me (4) species were performed both in the high- and low-spin configurations. The high-spin (quartet) tate was destabilized in energy by ∼7 kcal mol^{-1} relative to the low-spin (doublet) state.
58. Cohen, S. E.; Brignole, E. J.; Wittenborn, E. C.; Can, M.; Thompson, S.; Ragsdale, S. W.; Drennan, C. L. Negative-Stain Electron Microscopy Reveals Dramatic Structural Rearrangements in Ni-Fe-S-Dependent Carbon Monoxide Dehydrogenase/Acetyl-CoA Synthase. *Structure* **2021**, *29*, 43.e3– 49.e3, DOI: 10.1016/j.str.2020.08.011

59. Darnault, C.; Volbeda, A.; Kim, E. J.; Legrand, P.; Vernède, X.; Lindahl, P. A.; Fontecilla-Camps, J. C. Ni-Zn-[Fe4-S4] and Ni-Ni-[Fe4-S4] Clusters in Closed and Open α Subunits of Acetyl-CoA Synthase/Carbon Monoxide Dehydrogenase. *Nat. Struct. Mol. Biol.* **2003**, *10*, 271– 279, DOI: 10.1038/nsb912
60. Kisgeropoulos, E. C.; Manesis, A. C.; Shafaat, H. S. Ligand Field Inversion as a Mechanism to Gate Bioorganometallic Reactivity: Investigating a Biochemical Model of Acetyl CoA Synthase Using Spectroscopy and Computation. *J. Am. Chem. Soc.* **2021**, *143*, 849– 867, DOI: 10.1021/jacs.0c10135
61. Manesis, A. C.; O'Connor, M. J.; Schneider, C. R.; Shafaat, H. S. Multielectron Chemistry within a Model Nickel Metalloprotein: Mechanistic Implications for Acetyl-CoA Synthase. *J. Am. Chem. Soc.* **2017**, *139*, 10328– 10338, DOI: 10.1021/jacs.7b03892
62. Manesis, A. C.; Yerbulekova, A.; Shearer, J.; Shafaat, H. S. Thioester Synthesis by a Designed Nickel Enzyme Models Prebiotic Energy Conversion. *Proc. Natl. Acad. Sci. U. S. A.* **2022**, *119*, e2123022119 DOI: 10.1073/pnas.2123022119
63. Manesis, A. C.; Musselman, B. W.; Keegan, B. C.; Shearer, J.; Lehnert, N.; Shafaat, H. S. A Biochemical Nickel(I) State Supports Nucleophilic Alkyl Addition: A Roadmap for Methyl Reactivity in Acetyl Coenzyme A Synthase. *Inorg. Chem.* **2019**, *58*, 8969– 8982, DOI: 10.1021/acs.inorgchem.8b03546
64. Wongnate, T.; Sliwa, D.; Ginovska, B.; Smith, D.; Wolf, M. W.; Lehnert, N.; Raugei, S.; Ragsdale, S. W. The Radical Mechanism of Biological Methane Synthesis by Methyl-Coenzyme M Reductase. *Science* **2016**, *352*, 953– 958, DOI: 10.1126/science.aaf0616
65. Ravel, B.; Newville, M. ATHENA, ARTEMIS, HEPHAESTUS: Data Analysis for X-Ray Absorption Spectroscopy Using IFEFFIT. *J. Synchrotron Radiat.* **2005**, *12*, 537– 541, DOI: 10.1107/S0909049505012719
66. George, G. N.; Pickering, I. J. EXAFSPAK and EDG-FIT. *Stanf. Synchrotron Radiat. Lab. Stanf. Linear Accel. Cent. Stanf. CA.*
67. Neese, F.; Wennmohs, F.; Becker, U.; Riplinger, C. The ORCA Quantum Chemistry Program Package. *J. Chem. Phys.* **2020**, *152*, 224108, DOI: 10.1063/5.0004608
68. Weigend, F.; Ahlrichs, R. Balanced Basis Sets of Split Valence, Triple Zeta Valence and Quadruple Zeta Valence Quality for H to Rn: Design and Assessment of Accuracy. *Phys. Chem. Chem. Phys.* **2005**, *7*, 3297– 3305, DOI: 10.1039/B508541A

Chapter 4 Characterization of the Post-Thiolysis State of the A-cluster of Acetyl CoA Synthase

4.1 Abstract

Acetyl coenzyme A (ACS) together with carbon monoxide dehydrogenase (CODH) form the key enzyme complex in the reductive acetyl-CoA pathway also known as the Wood-Ljungdahl pathway (WLP). Together they catalyze the reversible reduction of CO_2 to acetyl-CoA which is an important metabolic intermediate. ACS is a nickel-containing iron-sulfur protein that combines CO, -CH_3, and coenzyme A to make acetyl-CoA and can reversibly form carbon-carbon and carbon-sulfur bonds. This flexibility and intriguing chemistry and its key role in metabolism for acetogens and methanogens has made understanding ACS of great interest to the bioinorganic and one-carbon metabolism communities. While much work has been published on this enzyme, the exact mechanism and redox state of its intermediates has been argued for decades. This work characterizes the reduced intermediate, A*, which forms after thiolysis of acetyl CoA, by XAS, EPR, Mössbauer, and methyl viologen redox equilibrium titrations identifying a new reduced intermediate of ACS.

4.2 Introduction

The Wood-Ljungdahl pathway (WLP) of carbon fixation is an ancient anaerobic metabolic pathway, utilized by methanogens, acetogens and other strict anaerobes to fix carbon dioxide and carbon monoxide into biomass. The key enzyme complex of carbon monoxide dehydrogenase (CODH) and acetyl coenzyme A synthase (ACS) together catalyze the reversible reduction of CO_2 to acetyl-CoA, an important metabolic intermediate. The active site of ACS, the A-cluster, is made up of a unique hexametal cluster, containing two nickels (proximal, Ni_p and distal, Ni_d) bridged by cysteines to a [4Fe4S] cluster. While much work has been done on this enzyme to determine its geometry[1,2] and structure[3–7], to characterize intermediates[8–13] and to understand its mechanism[11,12,14–16], the active reduced species of ACS remains contested.

The general mechanism of ACS involves random binding of a methyl group donated by the corrinoid iron sulfur protein (CFeSP) or CO to the proximal nickel, Ni_p. The methyl and CO condense to form a nickel-bound acetyl group and CoA does a nucleophilic attack to thiolyze the acetyl and form acetyl-CoA[14]. This series of nickel-bound carbon intermediates are an unusual feature of this enzyme. While all three carbon intermediates have been shown to bind directly to Ni_p, the redox states of the active intermediates is still debated between a paramagnetic and diamagnetic mechanism and more recently an electrochemical coupled mechanism has been proposed involving intermediates from both of these mechanisms in equilibrium[2,11]. The main difference between these mechanisms involves defining the active reduced state of the A-cluster that enters the catalytic cycle whether it is one electron reduced (paramagnetic) or two (diamagnetic) (Figures 1-5 and 1-6).

The paramagnetic mechanism proposes the activated state of ACS is a Ni_p^{1+}-$[4Fe4S]^{2+}$ cluster and this species has been observed by photolysis of CO bound ACS in IR and EPR[12]. Early characterization of the Ni_p^{1+}-CO by EPR was key discovery in this enzyme's history[8]. For the diamagnetic mechanism, the Ni_p^{2+}-methyl and Ni_p^{2+}-acetyl intermediates have also been directly chacterized[2]. The diamagnetic mechanism proposes the activated state of ACS is a 2 e^- reduced state with a putative nickel (0). While this state has been proposed to exist for many decades[11] , and many computational studies[15,17,18] have analyzed it, it had only been observed once by Mössbauer[19] and has never been repeated in literature.

In 2023, Gencic et. al. reported characterization of a two electron reduced state of the A-cluster, formed after thiolysis of acetyl-CoA[13]. This proposed state, they named A", was described as a $[Fe_4S_4]^{1+}Ni_p^{1+}$ A-cluster. They described careful redox titrations using cobalamin and methyl viologen to measure the midpoint potential of the A"/A_{ox} couple as well as diamagnetic EPR spectra and the kinetic competence of their species to bind methyl groups. However, this study lacks any direct structural or spectroscopic interrogation of the A-cluster, leading us to wonder, what is geometry and structure of the A-cluster after thiolysis of acetyl-CoA and can we also observe this putative nickel (0) state of the enzyme? We were intrigued by this previously uncharacterized state of the enzyme and have pursued further characterization of A" through XAS, Mössbauer, and EPR as well as our own methyl viologen titrations to shed further light on and increase our understanding of the mechanism of ACS. Because the results of our experiments substantially differ from Gencic, et. al. and do not support the formation of the

$[Fe_4S_4]^{1+}Ni_p^{1+}$ state that A" is described to be, we have designated the state of the A-cluster after thiolysis of acetyl-CoA to be A* in this work.

4.3 Materials and Methods

All chemicals and reagents were procured from Millipore Sigma (Darmstadt, Germany) and ThermoFisher Scientific (Waltham, MA) unless otherwise noted. 57Fe (95%) was purchased from Millipore Sigma. Ultrapure gases of N_2 and CO were sourced from Cryogenic Gases (Detroit, MI). Anaerobic expression was done in an Eppendorf 10 L double-jacket bioreactor fermenter using the New Brunswick™ BioFlo 110 system. The TEV-cleavable His6-tagged ACS expression plasmid is a kanamycin-resistant, lac-inducible pET29a vector containing the acsB gene from *Moorella thermoacetica*[20]. Iron-sulfur cluster assembly machinery co-expression plasmid is a tetracycline-resistant, lac-inducible pRKISC containing the isc operon from *E. coli*[21]. Ni-NTA resin used to purify ACS was from Qiagen (Valencia, CA). Bio-Gel P-2 resin from Bio-Rad Laboratories, Inc. (Hercules, CA) was used to purify methyl-cobinamide after synthesis. The red light used for all work involving methylcobinamide was an ABI LED Light, 660nm deep red, 24W bulb, sourced from Amazon (Seattle, WA). TEV protease was purified from an *E.* coli strain provided by Dr. Anindita Sarkar.

4.3.1 Use of anaerobic techniques in ACS characterization

All characterization techniques involving ACS including purification, kinetic assays, and preparation of spectroscopic samples were all completed under anoxic conditions (unless otherwise specified) in a Vacuum Atmospheres anaerobic chamber maintained at below 2.0 ppm O_2, measured with a calibrated Teledyne O_2 detector. All solutions and buffers with degassed by bubbling pure nitrogen gas through a septum sealed bottle. Any solutions where bubbling was not possible were degassed by exchanging the atmosphere of the sealed vial with nitrogen by alternating pulling vacuum and filling with nitrogen gas for at least 10 cycles. Solids that were reconstituted into solutions for assays and protein expressions were cycled in as dry powders and degassed overnight in the chamber before being dissolved in anaerobic water. All glassware and plastics that will interact with the protein are degassed in the chamber for a minimum of 24 hours before use.

4.3.2 Metal Free Work

Acetyl-CoA synthase is extremely sensitive to divalent metals, especially zinc and copper, occupying its nickel active site and rendering the enzyme inactive. To prevent this, all glassware used in purification, until the enzyme has been reconstituted with nickel, is acid washed for 2+ hours with 3M hydrochloric acid and then thoroughly rinsed with deionize water (milliQ). All buffers are made with milliQ water and treated with 2%w/v chelex 100 resin for at least one hour to remove trace metals.

4.3.3 Media and Antibiotics

The media for cultivation of *E. coli* was Terrific Broth with 0.5% glycerol added where noted. All media were autoclaved for 45 min on a liquid cycle. The antibiotics used in this work had the following concentrations: 50 µg/ml Kanamycin (kan), 7.5 µg/ml tetracyclin (tet).

4.3.4 10L expression of wild type acsB with pRKISC

The expression and purification of ACS from e coli is similar to previous reported methods[20] but the pDB1282[22,23] isc plasmid is replaced with pRKISC[21]. For expression of (WT) ACS, an overnight culture of 200mL TB was inoculated and grown at 37°C. The following morning, the 10L fermenter containing 9.8L of TB and 0.5% glycerol is preheated to 30°C. The 200mL overnight culture is added to the fermenter and the cells are bubbled with >7.5L/min of atmospheric air and stirred at 250rpm. When the culture reaches an OD_{600nm} of 0.8-1.0, the air is switched to high purity % N_2 gas and bubbled at >5L/min for 45 minutes to make the culture fully anaerobic. Then 3.6g of L-cysteine hydrochloride and 3.6g of sodium sulfide nonahydrate dissolved in anaerobic water are added to the culture. After 15 minutes, sterile anaerobic solutions of iron, nickel, and IPTG are added through a septum to final concentrations of 150uM iron ammonium sulfate, 200uM nickel chloride, and 200uM IPTG, and the nitrogen flow is reduced to ~0.5L/min to maintain anaerobicity overnight[20]. For the Mössbauer samples, instead of iron ammonium sulfate, 40uM iron-57 dissolved in 0.5M sulfuric acid was added at OD_{600nm} 0.3 and additional iron-57 in 0.5M sulfuric acid was added to a final concentration of 150uM with the nickel and IPTG. The cells were harvested anaerobically the following morning, typically 16-18hrs after induction with IPTG.

As previously described, the cells were lysed by sonication and purified over a Ni-NTA column, the tag was TEV cleaved, and the purified fractions flowed back over the Ni-NTA

column to remove the TEV and cleavage products. The purified protein was confirmed by SDS-PAGE and reconstituted with 5X nickel chloride and 5X iron ammonium sulfate for 72 hours before being buffer exchanged in to 50mM potassium phosphate, pH 7.6 with 2mM dithionite for storage[20]. For the Mössbauer samples with ^{57}Fe, the reconstitution used ^{57}Fe in 0.5M sulfuric acid instead of iron ammonium sulfate.

4.3.5 Methyl cobinamide synthesis

Methyl cobinamide (MeCbi) is a light sensitive reagent and will photolyze under normal light in a short period of time so all work with methyl cobinamide was done under red light. Under a nitrogen atmosphere, 10mg of dicyanocobinamide (Millipore Sigma #C3021), 200uL of 300mM titanium(III) citrate (6X)[24], 370uL of 40% anaerobic methyl iodide in methanol (240X) were combined in an amber septum sealed vial and allowed to react at room temperature (21°C) for between two and four hours. The orange-red product is purified to remove excess methyl iodide and titanium citrate by size exclusion on a 1 x 15 cm Biogel P2 column with 50mM potassium phosphate buffer pH 7.6. Fractions were collected in 0.5mL aliquots and purity and concentration are checked by UV-visible spectroscopy. For pure methyl-cob(III)inamide, ε_{390nm} is 8 $mM^{-1}cm^{-1}$ and ε_{470nm} is 10.8 $mM^{-1}cm^{-1}$. For pure cob(I)inamide ε_{390nm} = 25 $mM^{-1}cm^{-1}$ and ε_{470nm} = 3 $mM^{-1}cm^{-1}$. Pure, high concentration fractions were combined and stored at -20°C in amber vials. Method adapted from Wedemeyer et. al[25].

4.3.6 Methyl and Acetyl ACS

4.3.6.1 Methyl-ACS

In an amber vial, under red light, 3X methylcobinamide, 6X titanium citrate and 1X ACS are combined for 10 minutes. Methylation progress is confirmed by UV-visible spectroscopy. Excess methylcobinamide and titanium citrate are removed with a Biospin 6 size exclusion spin columns equilibrated with pH 7.6 50mM potassium phosphate.

4.3.6.2 Acetyl-ACS

In an amber vial, under red light, 3X methylcobinamide, 6X titanium citrate and 1X ACS are combined septum sealed and crimped, then the headspace is exchanged with CO for 15 minutes. Excess methylcobinamide, titanium citrate, and CO are removed with a Biospin 6 size exclusion spin column equilibrated with pH 7.6 50mM potassium phosphate.

4.3.7 Single turnover acetyl-CoA samples

An acetylated samples of ACS is made as described above. Then 6X coenzyme A (dissolved in anaerobic milliQ, fresh) is added, allowed to react for 30 seconds and the reaction quenched by precipitating the protein with 150mM potassium hydrogen phthalate, pH 4.0. The samples were frozen and stored at -20°C for further analysis. The concentration of the initial acetyl-ACS stock was determined by Rose-Bengal dye quantification[26].

4.3.8 Acetyl-CoA coupled colorimetric assay

This coupled UV-visible absorbance assay is not oxygen sensitive and was done at the bench. It is a coupled assay that used the eighth and first steps in the citric acid cycle to quantify acetyl-CoA. Malate dehydrogenase converted malate to oxaloacetate and reduced NAD+ to NADH. Citrate synthase then combined the oxaloacetate and acetyl-coenzyme A from the sample to be measured to make citrate and coenzyme A. The large excess of malate drives the coupled reactions to completion and couples the absorbance change at 340nm due to NADH production to the total acetyl-coenzyme A in solution[27,28]. Change in absorbance at 340nm was converted to nmol of acetyl-CoA relative to a standard curve determine with known concentrations of acetyl-CoA in the same matrix as the unknown samples.

The assay mixture is assembled in a 1.5mL quartz cuvette, containing 3mM malate, 0.1 mM NADH, 0.8 mM NAD+ in pH 8.1, 100mM Tris buffer with 0.9U of malate dehydrogenase (EC 1.1.1.37, Millipore Sigma M2634) and 0.45U of citrate synthase (EC 4.1.3.7, Millipore Sigma C3260). The baseline absorbance is measured, then 5-20uL of sample containing acetyl-CoA was added and the change in total absorbance at 340nm was calculated (corrected for dilution) and compared to the standard curve with an $R^2 > 0.994$ (see equation below) to determine the concentration of acetyl-CoA in a sample.

$$Absorbance_{340nm} = 0.004753 nmol^{-1} * [nmol\ of\ AcCoA]$$

4.3.9 Methyl viologen titrations

The methyl viologen (MV) titrations closely followed the methods outlined by Gencic et. al. with a few modifications[13]. Because ACS from *Moorella thermoacetica* precipitates in HEPES buffer, 50mM potassium phosphate, pH 8.0 buffer is used instead. 100uM total methylviologen (partially reduced with titanium citrate), 10uM acetyl-ACS, and 60uM coenzyme A (freshly dissolved in anaerobic milliQ) are combined in a small volume quartz cuvette and the

absorbance change at 600nm is recorded over time on an Ocean Optics USB4000 spectrophotometer with Mikropack DH-2000 deuterium hydrogen UV-vis-IR lamp. The protein concentration was corrected using the total acetyl-CoA produced in single turnover conditions as a measure of the active portion of the protein. Acetyl-ACS stocks were made fresh for each set of experiments and the single turnover acetyl-CoA was measured before and after the experiments and found not to measurably change within the time frame the acetyl-ACS stock was used. Absorbance measurements were corrected for dilution before calculations were complete.

4.3.10 XAS

XAS samples were prepared on two independent preparations of ACS as previously described[2,29]. The first set of samples had 90-100% active A-cluster measured by ICP-MS and by single-turnover acetyl-CoA formation. Samples from the first prep included A_{ox}, A_{ac}, A*, A* + CO. The second prep of ACS included 95% ^{57}Fe of the total iron had ~60% active A-cluster as measured by single-turnover acetyl-CoA formation. XAS samples made from this prep include A_{ox}, A_{ox} + CoA, A_{ac}, A*, A*+CO, A* + MeCbi, A* +CO + MeCbi. All samples were made in 50mM pH 7.6 potassium phosphate buffer with 20% glycerol at concentrations of greater than 1mM, except samples containing CO which were between 500 and 700µM. The A_{ox} samples were as isolated ACS. The A_{ac} samples were made as described above. The A* samples were made by adding 6X CoA to an A_{ac} stock to make A* which was then frozen in LN2 within five minutes. For A* + CO, A* was made and CO saturated buffer was added before freezing. For A* + MeCbi, A* was made and 1.1X methyl cobinamide was added before freezing. 1x methyl cobinamide has been previously shown to result in almost 100% methylation of ACS in XAS spectra[2]. For A* + CO + Me, A* was made and cleaned up with a BioSpin6 column to remove excess CoA and Acetyl-CoA, then 1.2X CO and 1.2X Me (relative to A*) was added to A* and frozen.

The XAS spectra were measured at the Stanford Synchrotron Radiation Lightsource on the focused 16-pole, 2 T wiggler side-station beam line 9-3 under standard ring conditions of 3 GeV and ~500 mA. Energy selection was accomplished with a Si(220) double crystal monochromator and higher harmonic were removed with an Rh-coated harmonic rejection mirror. During data collection, the samples were maintained at a constant temperature of ~10 K using an Oxford Instruments CF 1208 liquid helium cryostat. A 100-element

Ge monolith fluorescence detector from Canberra Industries was used for fluorescence data measurement.

Fe and Ni K-edge XAS data were measured on seven samples (A_{ox}, A_{me}, A_{ac}, A*, A* + CO, A* + MeCbi, A_{ox} + CoA) in the fluorescence mode by using soller-slits equipped with Mn-filter in front of the Ge detector and using an Fe-foil or Ni-foil for energy calibration. The first inflection point of the Fe-foil spectrum was fixed at 7111.2 eV and for Ni-foil was fixed at 8331.6eV. The samples were monitored for photoreduction and showed no signs of change during data collection. The EXAFS data for Fe K-edge were measured up to $k = 13$ Å^{-1} and for

4.3.11 Mössbauer

Mössbauer spectra were collected on a home-built system using a Janis Research SuperVaritemp dewar and LakeShore Model 331 A temperature controller and a 0.045 T permanent magnet. EPR and ENDOR (35 GHz) spectra were collected as continuous wave measurements with a 100 kHz field modulation[2]. ^{57}Fe Mössbauer spectra were collected for A*, A_{ox} and A_{Ac} at 4.2 K, under 0.1 T parallel to the γ-radiation. Spectra at low-temperature-high-field (LTLH) (4.2 K, 7 T) conditions of A_{ox} and A* were also measured. The samples A*, A_{ox} and A_{Ac} were made as described for the XAS samples and frozen bottom-up using an aluminum block pre-frozen in LN2.

4.3.12 EPR

Continuous-wave X-band EPR data were collected on a Bruker EMX equipped using a variable-temperature liquid nitrogen cavity with a MercuryiTC cryostat by Oxford Instruments. All spectra were collected using the WinEPR software package. EPR samples were made with the ^{57}Fe ACS used for Mössbauer and one set of XAS samples. The $A_{CO\ with\ DTH}$ sample was prepared as previously described[8] by mixing ACS in 50 mM potassium phosphate pH 7.6 with 2 mM sodium dithionite (DTH), transferred to an EPR tube capped with a rubber septum, and adding CO saturated buffer and flash freezing in liquid nitrogen. $A_{CO,\ no\ DTH}$ was made the same way but omitting the dithionite. The A_{ac} sample was made as described above. The A* and A* + CO were made as described for XAS and loaded into EPR tubes and flash frozen. Protein concentration was assessed by the Rose Bengal assay[26]. The EPR samples (two (A_{ac}, A*, $A_{CO,\ no\ DTH}$) or four ($A_{CO\ with\ DTH}$, A* + CO) scans) were run at 110K, 10 mW power, 0.4G modulation

amplitude, 9.189 GHz frequency. The NiFeC signal was quantified relative to a 1mM copper acetate standard.

4.4 Results

4.4.1 Acetyl-ACS stability

Stored anoxically at room temperature, acetylated ACS remains active for several days. The stability of acetylated ACS was measured over time by taking aliquots of acetyl-ACS from a stock solution and reacting them with an excess of CoA, then adding 150mM potassium hydrogen phthalate, pH 4.0 to quench the reaction. The samples were stored frozen at -20°C and then quantified using a coupled colorimetric assay (described in methods). The acetyl-ACS species is stable for 4-6 hours before degradation becomes significant and decays slowly according to a first order rate law (Figure 4-1).

$$\mu M\ A_{ac} = 91.55\ (\mu M) * e^{-0.12 * t\ (days)}$$

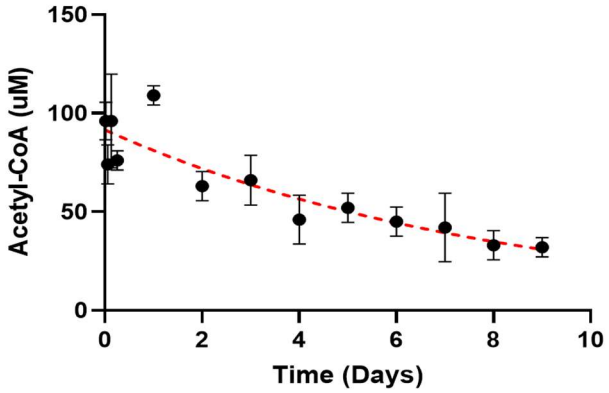

Figure 4-1 Stability of A_{ac} over time. Over the course of nine days, 24uL aliquots of acetyl-ACS were reacted with 6X CoA to forma acetyl-CoA. After 30 seconds, the reaction was quenched by precipitating the protein with 50mM potassium hydrogen phthalate and then freezing the samples for later analysis by a coupled colorimetric assay. Acetyl-ACS stocks are reasonably stable for 4-6 hours before degradation becomes measureable. Data was fit to a first order rate law.

4.4.2 Methyl viologen titrations

A key aspect of the Gencic, et. al characterization of A" was their redox titration experiments with redox active dyes (methyl viologen, cobalamin) to measure the midpoint potential of the $A_{ox} \rightleftharpoons A$" equilibrium and determine that there was a two electron difference between A_{ox} and A". In order to determine if the post-thiolysis state of the A-cluster is truly Ni^{1+}-$[Fe_4S_4]^{1+}$ (A") or something else, we needed to repeat these titrations in our hands with our

enzyme. The order of addition of acetyl-ACS (A_{ac}), methyl viologen (MV), and coenzyme A (CoA) was varied as well as the starting ratio reduced/oxidized methyl viologen.

These experiments were conducted on two independent purifications of ACS protein, one with ~90-100% A-cluster also used for a set of XAS samples (prep 1) and one with ~30% A-cluster (prep 2), determined by measurement of the total acetyl-CoA produced in a single turnover. The concentration of A* in each assay was corrected based on the percentage of total protein that produced acetyl-CoA in single turnover conditions. Reactions were set up with a varying amount of acetyl-ACS in the presence of different ratios of reduced to oxidized methyl viologen (MV_{red}/MV_{ox}, E_m = -450mV[30]). Then coenzyme A was added, methyl viologen was further reduced, and the absorbance at 600nm (after correction for dilution and protein concentration) was used to determine the final MV_{red} and MV_{ox} concentrations.

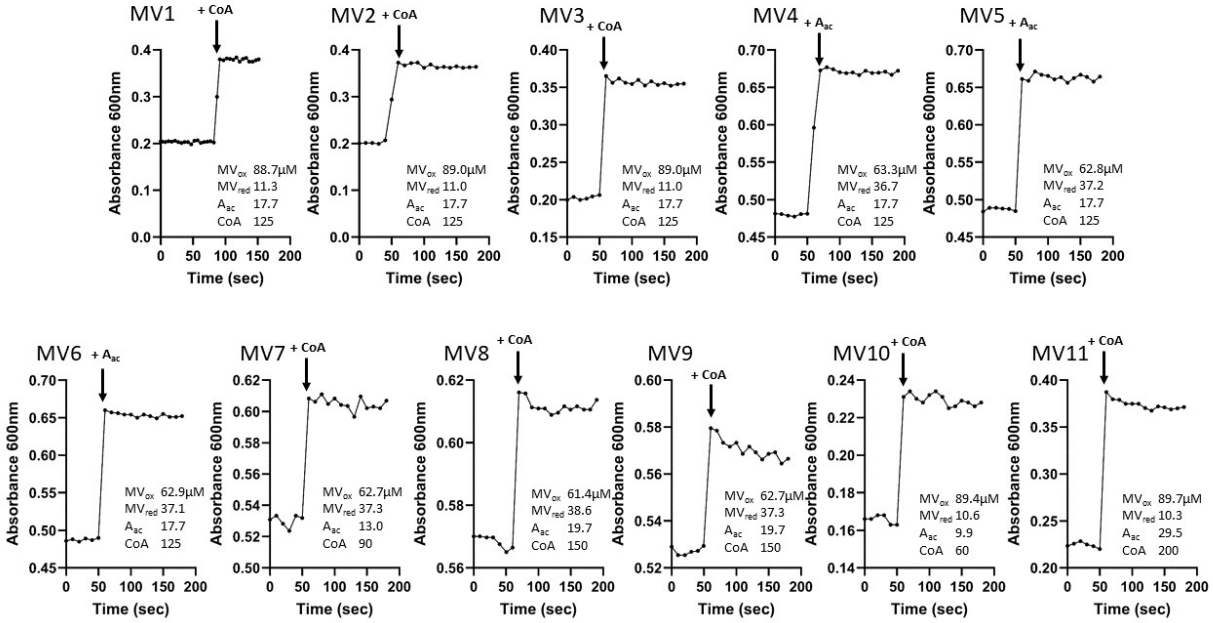

Figure 4-2 Methyl viologen titrations varying order of addition of A_{ac} and CoA, and starting MV red/ox ratios.

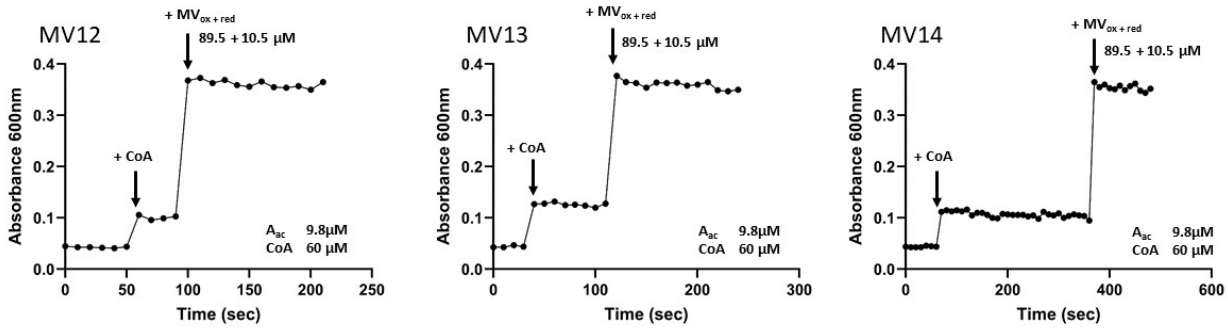

Figure 4-3 Methyl viologen titrations starting with A_{ac} and CoA and varying the waiting time, 30s (MV12), 1min 20sec (MV13), and 5 minutes (MV14), before adding methyl viologen to probe stability of A* state. A* can still reduce methyl viologen after 5 minutes so it is sufficiently stable to make spectroscopy samples.

While Gencic et. al. reported a consistent 1.6 -1.96 mols of MV reduced per mol of enzyme, our results (Figure 4-2, 4-3) were not so consistent with the mol of MV_{red}/mol of A-cluster (A) falling into a range of 0.2 up to 1.5 for a few experiments with the average for prep 1 (Table 4-1) being 0.64 ± 0.24 (95% CI) mol/mol MV/A. The average apparent midpoint potential ($E_{A*/Aox}$) of the titrations in Table 4-1 is -417 ± 8 mV (95% CI) and the apparent K_{eq} is 0.11 ± 0.05 (95% CI). Repetition of the MV titrations (n = 36) with the lower activity enzyme from prep 2 produced numbers in agreement with the values from prep 1 with an average apparent midpoint potential ($E_{A*/Aox}$) of -423 ± 11 mV (95% CI), 0.81 ± 0.17 (95% CI) mol/mol MV/A , and apparent K_{eq} of 1.9 ± 2.5 (95% CI).

		Reactants		Products				
		MV ox	A*	MV red	Aox	Keq	mol/mol MV/A	E (mV)
MV1	Initial	88.7	17.7	11.3	0.0	0.060	0.73	-414
	Final	75.7	11.2	24.3	6.5			
MV2	Initial	89.0	17.7	11.0	0.0	0.053	0.71	-413
	Final	76.4	11.4	23.6	6.3			
MV3	Initial	89.0	17.7	11.0	0.0	0.041	0.65	-409
	Final	77.5	11.9	22.5	5.8			
MV4	Initial	63.3	17.7	36.7	0.0	0.21	0.48	-430
	Final	54.9	13.5	45.1	4.2			
MV5	Initial	62.8	17.7	37.2	0.0	0.23	0.49	-431
	Final	54.2	13.4	45.8	4.3			
MV6	Initial	62.9	17.7	37.1	0.0	0.20	0.45	-429
	Final	54.9	13.7	45.1	4.0			
MV7	Initial	62.7	13.0	37.3	0.0	0.15	0.42	-426
	Final	57.3	10.3	42.7	2.7			
MV8	Initial	61.4	19.7	38.6	0.0	0.041	0.15	-409
	Final	58.4	18.2	41.6	1.5			
MV9	Initial	62.7	19.7	37.3	0.0	0.016	0.077	-398
	Final	61.2	18.9	38.8	0.8			
MV10	Initial	89.4	9.9	10.6	0.0	0.0102	0.48	-392
	Final	84.7	7.5	15.3	2.3			
MV11	Initial	89.7	29.5	10.3	0.0	0.016	0.36	-397
	Final	79.0	24.1	21.0	5.3			
MV12	Initial	89.5	9.8	10.5	0.0	0.21	1.36	-430
	Final	76.1	3.1	23.9	6.7			
MV13	Initial	89.5	9.8	10.5	0.0	0.21	1.36	-430
	Final	76.1	3.1	23.9	6.7			
MV14	Initial	89.5	9.8	10.5	0.0	0.17	1.30	-427
	Final	76.8	3.5	23.2	6.4			

Table 4-1 Summary of MV titrations from prep 1. The initial concentration of A* is calculated based on the amount of active protein (i.e. protein capable of single turnover Ac-CoA synthesis). Initial and final concentrations of MV_{red} were determined based on absorbance at 600nm (after correction for dilution and protein concentration). The initial and final MV_{ox} concentrations are determined from $MV_{red} + MV_{ox} = 100\mu M$. The final A* was calculated as A* initial minus half of the change in MV_{red}. K_{eq} was calculated from the ratio of final concentrations, $K_{eq} = (A_{ox}/A^*) \times (MV_{red}/MV_{ox})^2$. The apparent reduction potential $E_{A^*/Aox}$ was calculated by inserting the K_{eq} into the Nernst equation and using the standard reduction potential for MV of -450mV[30].

4.4.3 Ni XAS Results

Ni K-edge XAS were collected on seven samples (A_{ox}, A_{me}, A_{ac}, A*, A* + CO, A* + MeCbi, A_{ox} + CoA) to directly investigate whether A* is in the Ni^{1+}-$[Fe_4S_4]^{1+}$ state as proposed by Gencic et al[13] and if not, in what state is it? In Figure 4-4, comparison between the spectrum of A* and A_{ox}, shows small differences in A*, notably exhibiting two pre-edge features at 8330.5 eV and 8332.1 eV, whereas A_{ox} has a single peak at 8331.9 eV, consistent with prior work[2]. Subtle changes in the rising edge occur as well, with the prominent shoulder at 8335.5 eV in A_{ox} broadening and shifting to 8335.3 eV in A*. However, the rising edge itself does not experience any substantial redshift which would be indicate the formation of Ni^{1+}.

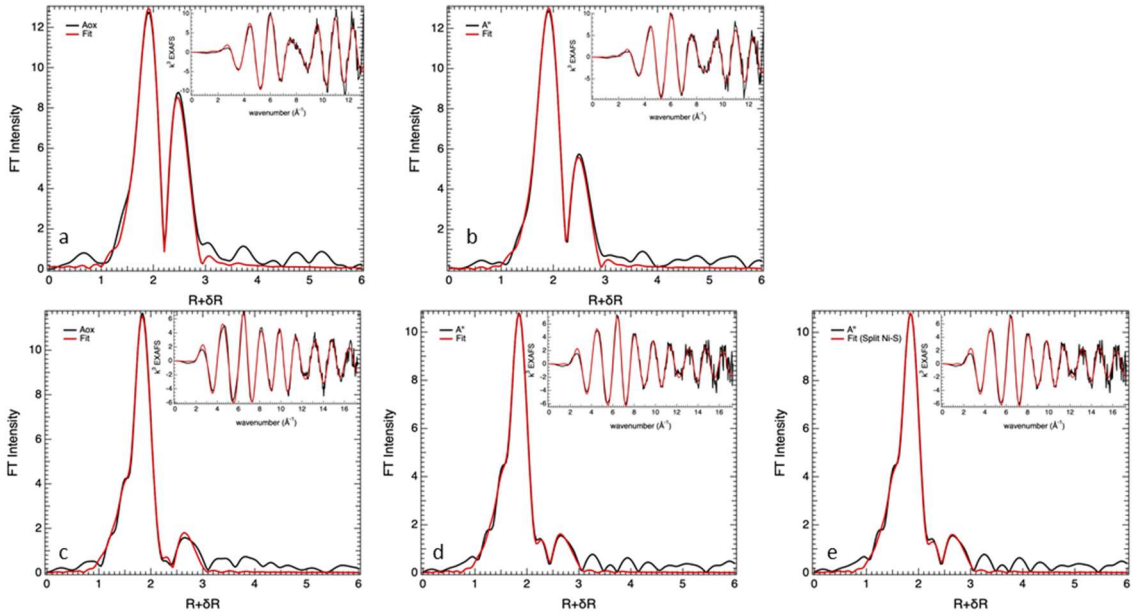

Figure 4-4 Feff-best fits to the Ni and Fe EXAFS. Best fits to the Fe EXAFS of Aox (a) and A" (b). Best fits to the Ni EXAFS of Aox (c) and A" (d), as well as A" with the Ni-S shell split (e). Fitting parameters are available in Table 4-2 and 4-3.

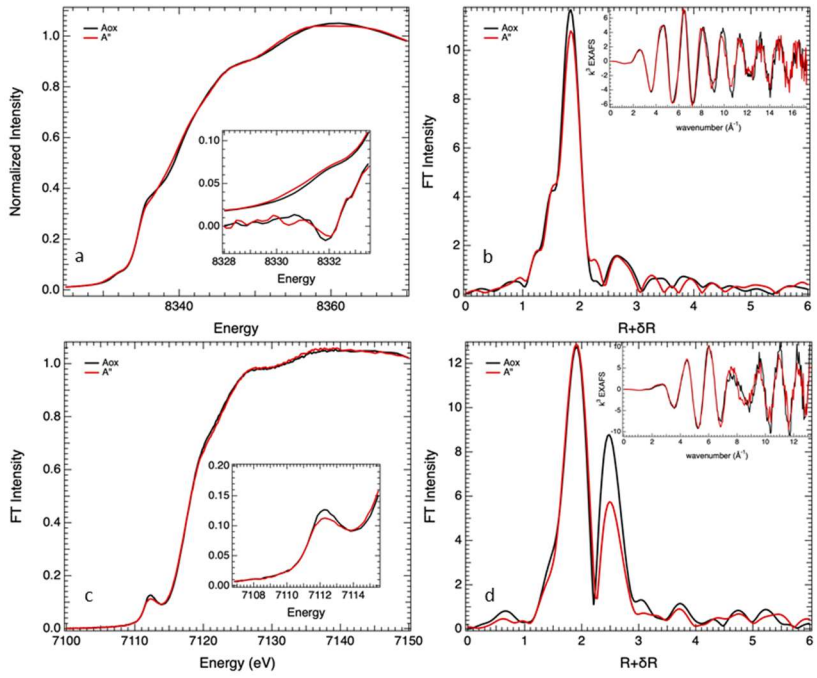

Figure 4-5 Ni and Fe K-edge XAS. a) Ni K-edge XAS of Aox and A" *inset*: magnification of the pre-edge region and its second derivative. b) Ni EXAFS showing changes in the first shell between Aox and A". c) Fe K-edge XAS of Aox and A" *inset*: magnification of the pre-edge region. d) Fe EXAFS of Aox and A" illustrating the substantial change in the Fe-Fe interaction.

The Ni EXAFS were also collected (Figure 4-5), exhibiting changes between 7 and 11 $Å^{-1}$ between the two species. Their Fourier transforms (Figure 4-5) show that these subtle changes manifest as a reduced intensity of the first shell feature in A* at 1.8 Å and the emergence of a feature at 2.3 Å in the non-phase corrected plot. Feff-based least squares fitting was conducted to investigate the origin of these features. A_{ox} was fit in a manner similar to prior work[2] (Table 4-2), and is consistent with 3 S bound to Ni_p, and two to Ni_d at a distance of 2.18 Å, 2 N bound to Ni_d at 1.88 Å and a water bound to Ni_p at 2.42 Å. A Ni_p-Ni_d contribution is observed at 2.94 Å, consistent with our prior findings[2], and an additional Ni_p-Fe contribution is observed at 2.77 Å. Two approaches were taken to model A*. In the first, the same fit used for A_{ox} was applied, and it was found that two waters were required at a distance of 2.46 Å, rather than the one required for A_{ox}, and the value of σ^2 for the Ni-S path increases by 18%, suggesting heterogeneity in the Ni-S interaction, whereas the σ^2 for the Ni_d-N was the same as that in A_{ox}. Together this indicates that the lowered first shell intensity in the Fourier transform in A* is due to increased heterogeneity in between Ni_p, Ni_d and their two bridging Cys, and the Cys which bridges Ni_p and the iron sulfur cluster. Additionally, the Ni_p-Fe contribution also elongates to 2.83 Å. Other than these changes, the remaining Ni-L distances and σ^2 are identical to that of A_{ox}. In the second approach, we attempted to investigate the heterogeneity in the Ni-S interaction further. To do this, the Ni-S path was split into two, one representing the cysteines which bridge Ni_p and Ni_d, and the other which bridges Ni_p and the iron-sulfur cluster. Under these conditions, the path which would correspond to the Cys bridging Ni_p and Fe elongates to 2.27Å, while still requiring two waters and with all other fitting parameters evaluating to be identical with those found in the first approach. Overall, the EXAFS analysis reveals similar Ni environments in A_{ox} and A*, with A* acquiring an additional water, likely at the apical position, and an elongated Ni_p-Fe distance, which is consistent with an elongated Ni_p-Cys bond.

	Coordination Number			Distance (Å)			σ^2		
Path	Aox	A"	A" (Split Ni-S)	Aox	A"	A" (Split Ni-S)	Aox	A"	A" (Split Ni-S)
Ni-S	2.5	2.5	2	2.18	2.20	2.19	0.00263	0.0031	0.00207
Ni-N	1	1	1	1.88	1.90	1.91	0.00313	0.00311	0.00288
Ni-O	0.5	1	1	2.42	2.46	2.46	0.00112	0.00133	0.00186
Ni-Ni	1	1	1	2.94	2.96	2.96	0.00571	0.00616	0.00626
Ni-Fe	0.5	0.5	0.5	2.77	2.83	2.83	0.0066	0.0064	0.00673
Ni-S(split)	-	-	0.5	-	-	2.27	-	-	0.0015

	Aox	A"	A" (split Ni-S)
R-factor	0.0037	0.0033	0.0031
reduced Chi-Sq	27.4	8.9	11.9
Nind	17.8	17.8	17.8
Nvar	11	11	13
R range	1.2-3.1	1.2-3.1	1.2-3.1
K range	2-17	2-17	2-17

Table 4-2 Ni EXAFS fitting parameters. The estimated standard deviations for the distances are in order of ± 0.02 Å.

4.4.4 Fe XAS Results

Fe XAS was also collected on both species (Figure 4-4). Fe K-edge XAS collected on A* and A_{ox} reveal identical spectra, differing only in the intensity of the pre-edge feature at 7111.9 eV (Figure 4-5). The similarity in the rising edge suggests that the iron sulfur cluster does not experience a major structural distortion on the formation of A*, relative to A_{ox}. To assess the magnitude of the change in the pre-edge, pseudo-Voigt peak deconvolution was carried out on both spectra (Figure 4-6). Both species were found to have identical centroid positions, (Table 4-3), while the amplitude of A* was lowered by 12%. Similar behavior has been observed in other biological iron-sulfur systems, such as ferredoxin (Fd)[31].

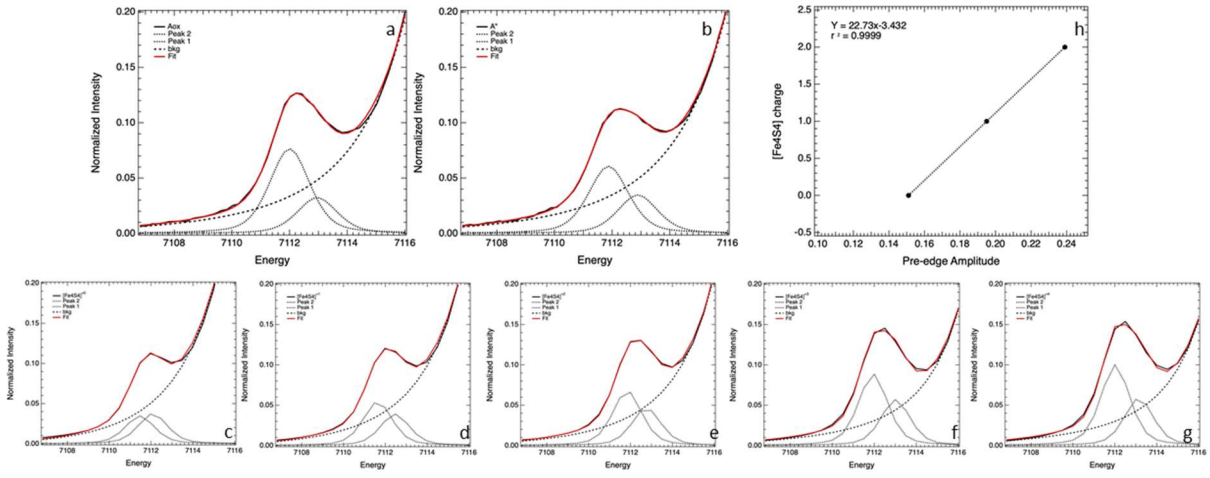

Figure 4-6 Pseudo-Voigt peak deconvolution of the pre-edge features of the Fe XAS of Aox and A" (a-b), as well as the biomimetic cubane redox series from Grunwald et al. 2024 (c-g). The [Fe4S4] Cubans in the +0 through +2 state

were used to make a calibration curve of pre-edge amplitude vs cluster charge to estimate the charge difference between Aox and A" (h).

	Coordination Number		Distance (Å)		σ^2	
Path	Aox	A"	Aox	A"	Aox	A"
Fe-S	4	4	2.30	2.30	0.00403	0.00428
Fe-Fe	2.25	2.25	2.74	2.72	0.00088	0.00224
Fe-Fe	1	1	2.58	2.56	0.00181	0.0009

	Aox	A"
R-factor	0.01	0.00
reduced Chi-Sq	13.8	6.3
Nind	11.0	11.0
Nvar	7	7
R range	1-2.8	
K range	3-12.8	3-12.8

Table 4-3 Fe EXAFS fitting parameters. The estimated standard deviations for the distances are in order of ± 0.02 Å.

Grunwald et al. recently published Fe K-edge data on a complete redox series of iron-sulfur cubanes[32], where they also observed decreases in pre-edge amplitude with successive reduction of the cubane, establishing a calibration curve which relate the two parameters. They have made their data available for use (10.3929/ethz-b-000742321), and we replicated their calibration curve using our fitting methodology, establishing a linear ($r^2 = 0.989$) relationship between pre-edge amplitude and the oxidation state of the cluster, comparable to that of the original study. Applying this to our data, we calculated a decrease in oxidation state of the A cluster [Fe_4S_4] cubane by ~0.6 in A*, relative to A_{ox}, and a 19% decrease in pre-edge amplitude between their $[Fe_4S_4]^{+2}$ and $[Fe_4S_4]^{+1}$ species (Table 4-4 and 4-5), nearly double that observed between A_{ox} and A*. We note that, whereas these standards exhibit a shift in the rising edge position upon reduction as well, such behavior is not always observed in biological [Fe_4S_4] clusters[1]. Since the pre-edge gains intensity not only from vacancies in the 3d-manifold, but from admixture with overlying 4p levels, it is also possible that this small decrease in PE intensity reflects a distortion of the cubane upon A* formation which results in less 4p character in the vacant Fe 3d orbitals. Or put another way, the partial reduction of the cluster may force a subtle distortion which lowers the 4p mixing, in addition to filling one of the available 3d vacancies, with both processes contributing to the lowered intensity.

Sample	Cluster Charge
Aox	1.7
A"	1.1

Table 4-4 Estimates of the iron-sulfur cluster charge obtained from peak deconvolution of the pre-edge feature, calibrated against the Grunwald et al. biomimetic cubane series[30].

	Aox		A*		[Fe4S4]+0		[Fe4S4]+1		[Fe4S4]+2		[Fe4S4]+3		[Fe4S4]+4	
pseud1_amplitude:	0.15913965	+/- 0.0131492	0.12642348	+/- 0.0055286	0.07256693	+/- 0.08377004	0.11347823	+/- 0.02918285	0.14185313	+/- 0.01319182	0.18529254	+/- 0.00840811	0.20874183	+/- 0.00719944
pseud1_center:	7111.99762	+/- 0.04717088	7111.87425	+/- 0.02903134	7111.46285	+/- 0.41551381	7111.63294	+/- 0.12942936	7111.83985	+/- 0.05457502	7111.94499	+/- 0.03234779	7112.0212	+/- 0.02629905
pseud1_fraction:	0.5	(fixed)	0.5	(fixed)	0.5	(fixed)	0.5	(fixed)	0.5	(fixed)	0.5	(fixed)	0.5	(fixed)
pseud1_sigma:	0.82069938	+/- 0.03700776	0.820699	(fixed)	0.820699	(fixed)	0.820699	(fixed)	0.820699	(fixed)	0.820699	(fixed)	0.820699	(fixed)
pseud1_fwhm:	1.64139876	+/- 0.07401552	1.641398	+/- 0	1.641398	+/- 0	1.641398	+/- 0	1.641398	+/- 0	1.641398	+/- 0	1.641398	+/- 0
pseud1_height:	0.07640227	+/- 0.00407494	0.0606954	+/- 0.00265426	0.03483909	+/- 0.04021766	0.05448044	+/- 0.01401057	0.06810311	+/- 0.00633334	0.0889582	+/- 0.0040367	0.10021611	+/- 0.00345642
pseud2_amplitude:	0.06737382	+/- 0.01024999	0.07233156	+/- 0.00546766	0.07809154	+/- 0.08393997	0.08151629	+/- 0.02904908	0.09703132	+/- 0.01313974	0.11892562	+/- 0.0083614	0.12221086	+/- 0.00716638
pseud2_center:	7112.95397	+/- 0.07742833	7112.88606	+/- 0.05204555	7112.08388	+/- 0.3808246	7112.45378	+/- 0.18337095	7112.75764	+/- 0.08094783	7113.01272	+/- 0.05142542	7113.14766	+/- 0.04559018
pseud2_fraction:	0.5	(fixed)	0.5	(fixed)	0.5	(fixed)	0.5	(fixed)	0.5	(fixed)	0.5	(fixed)	0.5	(fixed)
pseud2_sigma:	0.82069938	+/- 0.03700776	0.820699	+/- 0	0.820699	+/- 0	0.820699	+/- 0	0.820699	+/- 0	0.820699	+/- 0	0.820699	+/- 0
pseud2_fwhm:	1.64139876	+/- 0	1.641398	+/- 0	1.641398	+/- 0	1.641398	+/- 0	1.641398	+/- 0	1.641398	+/- 0	1.641398	+/- 0
pseud2_height:	0.03234588	+/- 0.00492098	0.03472809	+/- 0.002625	0.03749143	+/- 0.04029924	0.03913564	+/- 0.01394635	0.04658434	+/- 0.00630833	0.05709571	+/- 0.00401428	0.05867294	+/- 0.00344055
fit_centroid:	7112.28207	+/- 0.01401445	7112.24247	+/- 0.01341167	7111.78475	+/- 0.06018437	7111.97609	+/- 0.03640257	7112.21264	+/- 0.01958354	7112.38239	+/- 0.01533755	7112.43717	+/- 0.01425535
Fit.n_function_evals:	100		41		124		51		51		51		111	
Fit.n_data_points:	91		91		37		37		37		37		37	
Fit.n_variables:	10		9		9		9		9		9		9	
Fit.chi_square:	3.39E-04		2.36E-04		4.97E-04		2.59E-04		1.12E-04		1.01E-04		9.77E-05	
Fit.reduced_chi_square:	4.18E-06		2.88E-06		1.78E-05		9.26E-06		3.99E-06		3.59E-06		3.49E-06	
Fit.akaike_info_crit:	-1117.5799		-1152.3283		-397.05318		-421.14313		-452.250898		-456.19944		-457.25949	
Fit.bayesian_info_crit:	-1092.4713		-1129.7306		-382.55492		-406.64486		-437.752637		-441.70118		-442.76123	

Table 4-5 Pseudo-Voigt peak deconvolution parameters for the Fe K-pre-edge features.

The Fe EXAFS are supportive of this view. The EXAFS and their Fourier transform are presented in Figure 4-5, exhibiting a lower intensity in A* between 9 $Å^{-1}$ and 13 $Å^{-1}$, where the Fe-Fe scattering interaction dominates the signal. This is reflected in the Fourier transform, where the two species exhibit identical Fe-S shell intensities, but the second shell corresponding to Fe-Fe backscattering interactions is significantly attenuated in A*. Such behavior is well established for redox series in both biological[33,34] and inorganic[35] iron-sulfur cubane systems. Feff-based fitting of the Fe EXAFS (Table 4-3) support 4 S at 2.30 Å in both species, while A* has an intra-rhomb Fe-Fe distance contracted by 0.02 Å relative to A_{ox} at 2.56 Å, and a trans cubane rhomb-rhomb Fe-Fe distance of 2.72 Å, which is also contracted by 0.02 Å relative to the A_{ox} case. This shell includes the Fe-Ni contribution, which is slightly longer than the Fe-Fe distance (per the Ni EXAFS) but close enough that separating it out as its own path in the fit well exceeds the resolution of our data. To better understand the origin of the decreased second shell intensity in A*, a comparison of σ^2 was conducted. Whereas the intra-rhomb Fe-Fe σ^2 decreases between A* and A_{ox}, the trans cubane rhomb-rhomb interaction (which encompasses one Fe-Ni_p interaction) sees a σ^2 in A* that is approximately 2.5x that of A_{ox}, indicating that this interaction is the origin of the lower intensity, and that a distortion in the cubane occurs due to the additional electron density in A*.

4.4.5 Mössbauer of A, A_{ox} and A_{ac}*

^{57}Fe Mössbauer spectra were collected for A*, A_{ox} and A_{ac} at 4.2 K, under 0.1 T parallel to the γ-radiation (Figure 4-7). All three spectra exhibited asymmetric quadrupole doublets as the major features, indicating the majority show integer spin states, consistent with previous observations in literature[2]. Specifically, the A_{ac} and A_{ox} states are almost identical in the iron sulfur cluster. The major doublet can be reproduced with two iron sites with 7:3 ratio, the parameters of which are δ = 0.44 and 0.55 mm/s, ΔE_Q = +1.08 and +1.26 mm/s; η = 0.4 and 0.1.

The spectrum at low-temperature-high-field (LTLH) (4.2 K, 7 T) condition of A_{ox} further confirmed the diamagnetic ground state of this species, as well as the positive sign of quadrupole splitting for both Fe sites. An alternative simulation utilizing an asymmetric Lorentzian doublet yields δ = 0.46 mm/s, $|\Delta E_Q|$ = 1.10 mm/s, Γ_L = 0.316 mm/s, Γ_R = 0.373 mm/s. The values closely match our previous spectra for as-isolated ACS enzyme (δ = 0.46 mm/s, $|\Delta E_Q|$ = 1.11 mm/s, Γ_L = 0.299 mm/s, Γ_R = 0.392 mm/s)[2]. Therefore, our Mössbauer analysis suggests that A_{ox} and A_{ac} are almost identical. The major species are diamagnetic, showing an averaged isomer shift value consistent with mix-valence $Fe^{2.5+}/Fe^{2.5+}$ pair.

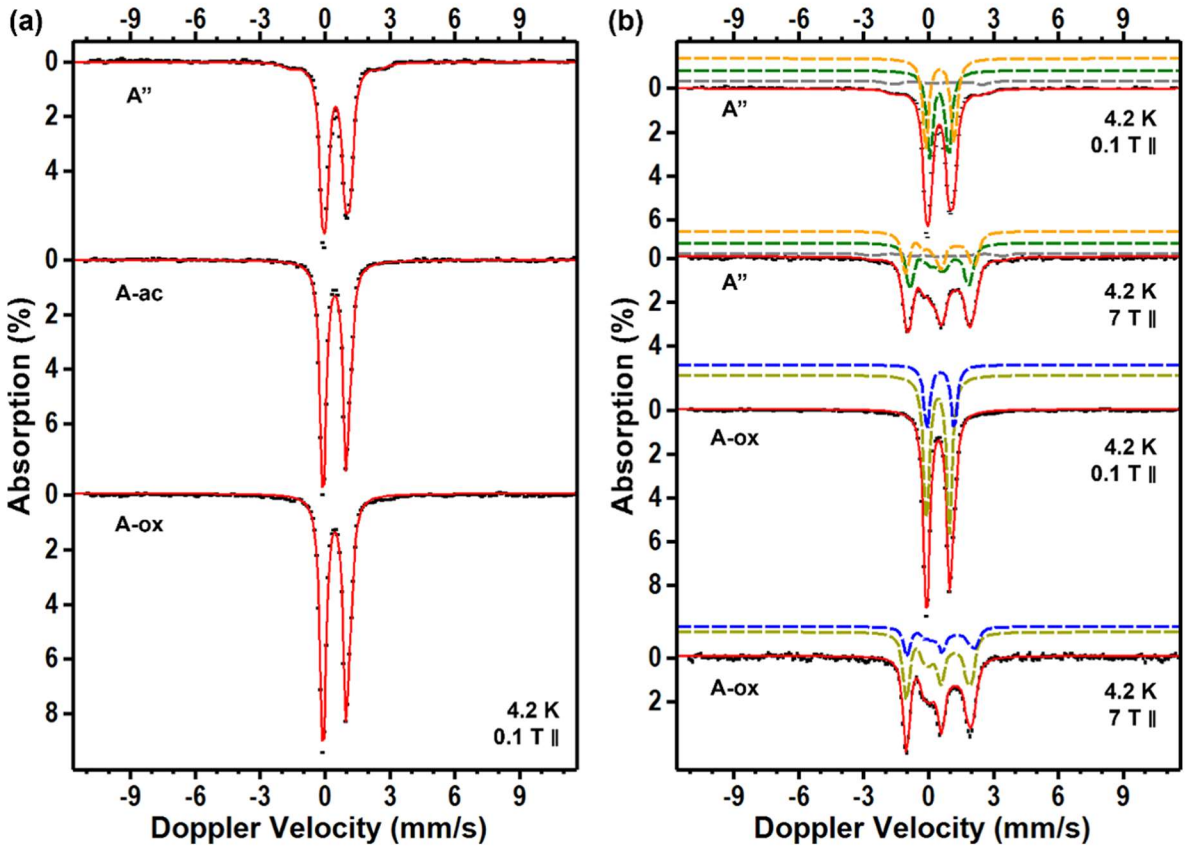

Figure 4-7 ^{57}Fe Mb spectra for A-ox, A-ac and A" under indicated conditions. Black bars represent experimental values (center positions) and associated uncertainties (bar lengths). Red lines represent overall simulations, colored dashed lines show individual components: Site I for A-ox in blue, Site II for A-ox in olive, Site I for A" in green, Site II for A" in orange, A_{red}-CO in grey.

For A*, the major spectral feature is also an asymmetric quadruple doublet, which is clearly shifted to positive δ values when compared to A-ox and A-acetyl. In addition, one minor paramagnetic species is present, which can be reproduced using the parameters reported for A_{red}-CO[36]. The asymmetric doublet in A* can be simulated with two Fe sites in a 1:1 ratio, having parameters δ = 0.50 and 0.51 mm/s, ΔE_Q = +0.84 and +1.32 mm/s; η = 0.7 and 0.5, respectively.

4.4.6 EPR

Figure 4-8 shows EPR spectra collected on five samples (A_{ox} + CO + DTH, A_{ox}+CO (no DTH), A_{ac}, A*, A* + CO) from the same purification of ^{57}Fe ACS used for Mössbauer and XAS samples. Of these five samples, the A_{ox} + CO without dithionite added produced a very small signal, less than 2% spin, A_{ox}+CO with dithionite (DTH) and A* + CO both produced an EPR signal quantifying to 22% spin and 23% spin, respectively. These spectra all match the expected NiFeC signal, a defining characteristic of this protein with g-values of 2.071, 2.029 for A_{ox}+CO and 2.066, 2.028 for A* + CO. While these g-values do match the WT g-values of 2.074 and 2.028[8] well, the A*+CO g-values are slightly shifted towards to the observed g-values for the F229A (2.062, 2.028) [29] or F195A (2.062, 2.027) [9] mutants of ACS and ACDS suggesting that A*+CO has slight conformational differences or a mixture of conformers as determined by ENDOR for the F229A mutant[37]. Until now, the NiFeC signal has only been observed when CO is added to ACS in the presence of a reductant, like dithionite[8,29] or titanium(III) citrate[9] thus confirming A* must be more reduced than A_{ox}. The CO was added to A* and frozen within five minutes and the complete recovery of spins to match the traditional CO-ACS sample (A_{ox} + CO + DTH) while the A_{ox} sample without reductant was unable to significantly bind CO demonstrates this reduced form of ACS, A*, is competent to bind a reactant, CO, and sufficiently stable for up to five minutes, a reasonable time scale for the assembly and freezing of spectroscopy samples. The A* state on its own lacked an EPR signal indicating it is diamagnetic, as is the A_{ac} state which is consistent with previous characterization of A_{ac}[2].

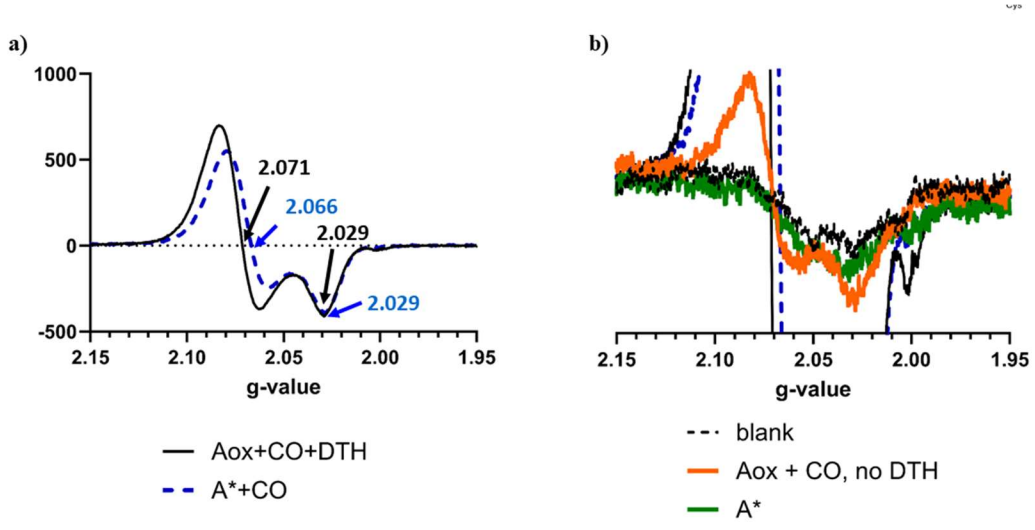

Figure 4-8 EPR of A_{ox}+ CO + dithionite, A* + CO, A_{ox} + CO, and A*. CW EPR collection parameters were 10mW, 110K, 0.4G modulation amplitude, gain 10, frequency 9.189 GHz. a) A_{ox} + CO + dithionite and A* + CO both

exhibit the characteristic NiFeC signal with 22%, and 23% spin respectively b) all spectra, zoom in of EPR spectra clearly show that A* exhibits no signal and A_{ox} + CO, no dithionite has a very small, <2% spin NiFeC signal due to slight contamination of reductant in the sample.

4.5 Discussion

Thus far, this characterization of A* generally supports the formation of a diamagnetic Ni_p^{2+}-$[4Fe4S]^{2+}$ state after thiolysis of acetyl-CoA. The midpoint potential of the transition from A_{ox} to A* as determined by the MV titrations is between -410 and -430 mV which aligns with the low end of the range of midpoint potentials for activation of the A-cluster reported between -430mV to -530mV (vs. SHE) measured on CODH/ACS[38–41].

The Fe EXAFS and Mössbauer are both consistent with a 0.5-1 electron reduction of the iron sulfur cluster in A* relative to A_{ox}. The EPR spectra, Mössbauer, and XAS show A* to be diamagnetic, and yet A* is able to transfer approximately 1 electron onto methyl viologen based on the redox titrations. Together these data raise two main questions. Where is the rest of the electron localized that is able to transfer to methyl viologen? And how can A* be diamagnetic and yet still be one electron reduced relative to A_{ox}?

One option is that remainder of the electron charge is located in the bridging cysteine sulfur that connects Ni_p to the 4Fe4S cluster. Such a species would not be readily detectable by EPR due to the highly anisotropic g values typically associated with sulfur radicals, which act to broaden their signal in the EPR to undetectable levels. Based on the XAS data, such a species would preferentially interact with the FeS cubane, as opposed to the Ni, as we see scant evidence of additional spin on the Ni and both A* Ni EXAFS fitting approaches indicate that something perturbs the homogeneity of the Ni-S sphere in A*, consistent with the elongation of one Ni-S bond, which we suspect to be the one that bridges to the FeS cubane.

Also, there is the matter of the Ni-Fe elongation observed in A*, which would follow from an elongation of the Ni_p away from the bridging cysteine provided the Ni-S-Fe angle also increases to swing the FeS cubane away from Ni_p, which would be expected with the filling of the cysteine lowest unoccupied molecular orbital (LUMO) by 1 electron. This hypothesis can be tested with DFT and calculations are ongoing to investigate if these movements are consistent with the EXAFS data. In the absence of another electron to spin-pair with this one to result in a diamagnetic state, this hypothesis requires that the current assessment of diamagnetism in both the XAS and Mossbauer is wrong, and that the species is one electron reduced.

In Mössbauer, isomer shift values serves as a powerful probe for changes in Fe valence, as they are highly sensitive to the Fe d-shell electron density[42,43]. In general, increased electron density in Fe d-shell leads to a positive shift in δ. To reduce ambiguity, we focused on the average isomer shift (δ_{AV}), weighted by the relative areas. From A_{ox} to A*, the δ_{AV} of the major diamagnetic species increases by +0.04 mm/s per Fe. This shift is significantly smaller than that observed for typical one-electron reduction of $[Fe_4S_4]$ clusters (+0.08 mm/s for *Chromatium* HiPIP[44], and +0.13 mm/s for B. *stearothermophilus* Ferredoxin[45]). Such a small shift falls within the expected range for "half-electron injection". In contrast, this subtle shift is reminiscent of the ligation change observed in ferredoxin:thioredoxin reductase (FDR) of *Methanosarcina* acetivorans[46,47]. In FDR enzyme, the resting $[Fe4S4]^{2+}$ cluster is ligated by four Cys residues together with a close S atom from a disulfide bond. In the two electron reduced state, the disulfide bond cleaves into a dithiol, creating a close contact thiol interaction with the $[Fe4S4]^{2+}$ cluster. This disulfide-to-dithiol change results in a positive δ_{AV} shift of +0.05 mm/s per Fe. Therefore, the small change in δ_{AV} between A_{ac} and A* is more likely due to a change in ligation rather than direct one-electron injection into the $[Fe_4S_4]$ cluster.

While these results still raise fundamental questions about the nature of the A-cluster, our assignment of this A-cluster state differs from the recent report of this post-thiolysis intermediate (named E") by Gencic et. al.[13], who described the formation of a Ni_p^{1+}-$[4Fe4S]^{1+}$ A-cluster as the direct product of acetyl-CoA thiolysis. While Gencic et. al. describes careful redox titrations with both cobalamin and methyl viologen and reports EPR spectra in agreement with the EPR spectra of A_{ac} and A* that we report here, their investigation lacks direct spectroscopic characterization of the iron-sulfur cluster to definitively demonstrate a reduced 1^+ cluster as well as direct interrogation of the nickel site to assess its redox state. Our spectroscopic results do not support the formation of a Ni_p^{1+}-$[4Fe4S]^{1+}$ after loss of the acetyl group. Their study was also conducted on the archaea protein from *Methanosarcina thermophila* (ACDS β subunit *CdhC**) which lacks the first domain of the protein when compared to *acsB* (ACS) from *Moorella thermoacetica*[13]. Since ACS undergoes many conformational changes during its catalytic cycle, missing an entire domain may cause deviations in the secondary sphere ligands surrounding the A-cluster and may contribute to some of the differences observed between the work reported here and their characterization of E".

4.6 Conclusion

Herein we report the characterization of a catalytically relevant intermediate of ACS that forms after the loss of acetyl-CoA that we have called A*. Both Mössbauer and XAS characterization of A* support its identity as a Ni_p^{2+}-$[4Fe4S]^{2+}$ with a small paramagnetic component and slightly reduced relative to the A_{ox} resting state. While we currently appear to be left with more questions than definitive answers about A* so far, this spectroscopic interrogation of the A-cluster furthers our knowledge of the complexities of the A-cluster and its chemistry.

Further analysis of the XAS data and DFT modeling of the proposed explanations for the 0.5eV change in the iron-sulfur cluster from A* to A_{ox} are ongoing and necessary to support or reject these hypotheses. Also low temperature EPR, <10K, of A*+CO and A* samples to look at the iron sulfur cluster and a potential thiyl radical is planned and may reveal more insight as to why this small paramagnetic feature is arising in the Mössbauer. Further redox titrations using cobalamin or another redox active dye may also provide more consistent results than the methyl viologen based titrations to further strengthen these conclusions. An intriguing future direction for work on this intermediate would be to pursue repetition of the CO photolysis experiment[12] originally measured by EPR that produced a reduced Ni(I) species with no ligand bound and determine how this species differs from A*. Reproduction of this Ni(I) state to be characterized by high resolution XAS would be informative for further characterizing the Ni(I) species, drawing comparisons with A*, and provide further evidence to support or reject the proposed mechanisms. While a bit more work is necessary to fully characterize this Ni_p^{2+}-$[4Fe4S]^{2+}$ (A*) intermediate, the spectroscopy and redox data presented here rejects the proposed putative nickel(0) Ni_p^{1+}-$[4Fe4S]^{1+}$ A-cluster as the direct product of acetyl-CoA synthesis by ACS.

4.7 Author Contributions

The contents of this chapter are part of a manuscript in preparation: Griffith, C. L., Abernathy, M. J., Xiong, J., Guo, Y. Sarangi, R. Ragsdale, S.W

4.8 References for Chapter 4

(1) Can, M.; Giles, L. J.; Ragsdale, S. W.; Sarangi, R. X-Ray Absorption Spectroscopy Reveals an Organometallic Ni–C Bond in the CO-Treated Form of Acetyl-CoA Synthase. *Biochemistry* **2017**, *56* (9), 1248–1260. https://doi.org/10.1021/acs.biochem.6b00983.

(2) Can, M.; Abernathy, M. J.; Wiley, S.; Griffith, C.; James, C. D.; Xiong, J.; Guo, Y.; Hoffman, B. M.; Ragsdale, S. W.; Sarangi, R. Characterization of Methyl- and Acetyl-Ni Intermediates in Acetyl CoA Synthase Formed during Anaerobic CO_2 and CO Fixation. *J. Am. Chem. Soc.* **2023**, *145* (25), 13696–13708. https://doi.org/10.1021/jacs.3c01772.

(3) Doukov, T. I.; Blasiak, L. C.; Seravalli, J.; Ragsdale, S. W.; Drennan, C. L. Xenon in and at the End of the Tunnel of Bifunctional Carbon Monoxide Dehydrogenase/Acetyl-CoA Synthase,. *Biochemistry* **2008**, *47* (11), 3474–3483. https://doi.org/10.1021/bi702386t.

(4) Darnault, C.; Volbeda, A.; Kim, E. J.; Legrand, P.; Vernède, X.; Lindahl, P. A.; Fontecilla-Camps, J. C. Ni-Zn-[Fe4-S4] and Ni-Ni-[Fe4-S4] Clusters in Closed and Open α Subunits of Acetyl-CoA Synthase/Carbon Monoxide Dehydrogenase. *Nat Struct Mol Biol* **2003**, *10* (4), 271–279. https://doi.org/10.1038/nsb912.

(5) Lemaire, O. N.; Wagner, T. Gas Channel Rerouting in a Primordial Enzyme: Structural Insights of the Carbon-Monoxide Dehydrogenase/Acetyl-CoA Synthase Complex from the Acetogen Clostridium Autoethanogenum. *Biochimica et Biophysica Acta (BBA) - Bioenergetics* **2021**, *1862* (1), 148330. https://doi.org/10.1016/j.bbabio.2020.148330.

(6) Ruickoldt, J.; Kreibich, J.; Bick, T.; Jeoung, J.-H.; Duffus, B. R.; Leimkühler, S.; Dobbek, H.; Wendler, P. Ligand Binding to a Ni–Fe Cluster Orchestrates Conformational Changes of the CO-Dehydrogenase–Acetyl-CoA Synthase Complex. *Nat Catal* **2025**, *8* (7), 657–667. https://doi.org/10.1038/s41929-025-01365-y.

(7) Biester, A.; Grahame, D. A.; Drennan, C. L. Capturing a Methanogenic Carbon Monoxide Dehydrogenase/Acetyl-CoA Synthase Complex via Cryogenic Electron Microscopy. *Proceedings of the National Academy of Sciences* **2024**, *121* (41), e2410995121. https://doi.org/10.1073/pnas.2410995121.

(8) Ragsdale, S. W.; Wood, H. G.; Antholine, W. E. Evidence That an Iron-Nickel-Carbon Complex Is Formed by Reaction of CO with the CO Dehydrogenase from Clostridium Thermoaceticum. *Proceedings of the National Academy of Sciences* **1985**, *82* (20), 6811–6814. https://doi.org/10.1073/pnas.82.20.6811.

(9) Gencic, S.; Kelly, K.; Ghebreamlak, S.; Duin, E. C.; Grahame, D. A. Different Modes of Carbon Monoxide Binding to Acetyl-CoA Synthase and the Role of a Conserved Phenylalanine in the Coordination Environment of Nickel. *Biochemistry* **2013**, *52* (10), 1705–1716. https://doi.org/10.1021/bi3016718.

(10) Ragsdale, S. W.; Ljungdahl, L. G.; DerVartanian, D. V. EPR Evidence for Nickel-Substrate Interaction in Carbon Monoxide Dehydrogenase from Clostridium Thermoaceticum. *Biochemical and Biophysical Research Communications* **1982**, *108* (2), 658–663. https://doi.org/10.1016/0006-291X(82)90880-4.

(11) Ragsdale, S. W. 8.24 - Biological Carbon Fixation by an Organometallic Pathway: Evidence Supporting the Paramagnetic Mechanism of the Nickel-Iron-Sulfur Acetyl-CoA Synthase. In *Comprehensive Coordination Chemistry III*; Constable, E. C., Parkin, G., Que Jr, L., Eds.; Elsevier: Oxford, 2021; pp 611–633. https://doi.org/10.1016/B978-0-08-102688-5.00082-9.

(12) Bender, G.; Stich, T. A.; Yan, L.; Britt, R. D.; Cramer, S. P.; Ragsdale, S. W. Infrared and EPR Spectroscopic Characterization of a Ni(I) Species Formed by Photolysis of a Catalytically Competent Ni(I)-CO Intermediate in the Acetyl-CoA Synthase Reaction. *Biochemistry* **2010**, *49* (35), 7516–7523. https://doi.org/10.1021/bi1010128.

(13) Gencic, S.; Duin, E. C.; Grahame, D. A. The Two-Electron Reduced A Cluster in Acetyl-CoA Synthase: Preparation, Characteristics and Mechanistic Implications. *Journal of Inorganic Biochemistry* **2023**, *240*, 112098. https://doi.org/10.1016/j.jinorgbio.2022.112098.

(14) Seravalli, J.; Ragsdale, S. W. Pulse-Chase Studies of the Synthesis of Acetyl-CoA by Carbon Monoxide Dehydrogenase/Acetyl-CoA Synthase: EVIDENCE FOR A RANDOM MECHANISM OF METHYL AND CARBONYL ADDITION*. *Journal of Biological Chemistry* **2008**, *283* (13), 8384–8394. https://doi.org/10.1074/jbc.M709470200.

(15) Chmielowska, A.; Lodowski, P.; Jaworska, M. Redox Potentials and Protonation of the A-Cluster from Acetyl-CoA Synthase. A Density Functional Theory Study. *J. Phys. Chem. A* **2013**, *117* (47), 12484–12496. https://doi.org/10.1021/jp402616e.

(16) Manesis, A. C.; Shafaat, H. S. Electrochemical, Spectroscopic, and Density Functional Theory Characterization of Redox Activity in Nickel-Substituted Azurin: A Model for

Acetyl-CoA Synthase. *Inorg. Chem.* **2015**, *54* (16), 7959–7967. https://doi.org/10.1021/acs.inorgchem.5b01103.

(17) Maria Jaworska; Piotr Lodowski. Theoretical Studies of Acetyl-CoA Synthase Catalytic Mechanism. *Catalysts* **2022**, *12* (195), 1–21.

(18) Elghobashi-Meinhardt, N.; Tombolelli, D.; Mroginski, M.-A. QM/MM Computations Reveal Details of the Acetyl-CoA Synthase Catalytic Center. *Biochim Biophys Acta Gen Subj* **2020**, *1864* (7), 129579. https://doi.org/10.1016/j.bbagen.2020.129579.

(19) Tan, X.; Martinho, M.; Stubna, A.; Lindahl, P. A.; Münck, E. Mössbauer Evidence for an Exchange-Coupled {[Fe4S4]1+ Nip1+} A-Cluster in Isolated α Subunits of Acetyl-Coenzyme A Synthase/Carbon Monoxide Dehydrogenase. *J. Am. Chem. Soc.* **2008**, *130* (21), 6712–6713. https://doi.org/10.1021/ja801981h.

(20) Burton, R.; Can, M.; Esckilsen, D.; Wiley, S.; Ragsdale, S. W. Chapter Twelve - Production and Properties of Enzymes That Activate and Produce Carbon Monoxide. In *Methods in Enzymology*; Armstrong, F., Ed.; Enzymes of Energy Technology; Academic Press, 2018; Vol. 613, pp 297–324. https://doi.org/10.1016/bs.mie.2018.10.005.

(21) Nakamura, M.; Saeki, K.; Takahashi, Y. Hyperproduction of Recombinant Ferredoxins in Escherichia Coli by Coexpression of the ORF1-ORF2-iscS-iscU-iscA-hscB-hscA-Fdx-ORF3 Gene Cluster1. *The Journal of Biochemistry* **1999**, *126* (1), 10–18. https://doi.org/10.1093/oxfordjournals.jbchem.a022409.

(22) Deborah C. Johnson; Mihaela-Carmen Unciuleac; Dennis R. Dean. Controlled Expression and Functional Analysis of Iron-Sulfur Cluster Biosynthetic Components within Azotobacter Vinelandii. *Journal of Bacteriology* **2006**, *188* (21), 7551–7561. https://doi-org/10.1128/jb.00596-06o.

(23) Deborah Cumaraswamy Johnson. Controlled Expression of the Iron Sulfur Cluster Biosynthetic Machinery in Azotobacter Vinlendii, Virginia Tech, 2008. https://vtechworks.lib.vt.edu/server/api/core/bitstreams/6f465ac6-3f62-4fa2-b952-15050d29b14d/content (accessed 2025-08-28).

(24) Seefeldt, L. C.; Ensign, S. A. A Continuous, Spectrophotometric Activity Assay for Nitrogenase Using the Reductant Titanium(III) Citrate. *Analytical Biochemistry* **1994**, *221* (2), 379–386. https://doi.org/10.1006/abio.1994.1429.

(25) Christina Wedemeye-Exl, Tamis Darbre, Reinhart Keese. Preparation of Dicyano- and Methylcobiniamide from Vitamin B12a. *Synthesis* **2008**, *21*, 3229–3432. https://doi.org/10.1055/s-0028-1083187.

(26) Elliott, J. I.; Brewer, J. M. The Inactivation of Yeast Enolase by 2,3-Butanedione. *Archives of Biochemistry and Biophysics* **1978**, *190* (1), 351–357. https://doi.org/10.1016/0003-9861(78)90285-0.

(27) Karl Decker. Acetyl-Coenzyme A UV-Spectrophotometric Assay. In *Methods of Enzymatic Analysis*; Hans Ulrich Bergmeyer, Patricia Lund, Eds.; Dermot H. Williamson, Translator; Verlag Chemie Weinheim Academic Press, Inc.: New York, US and London, UK, 1974; Vol. 4, pp 1988–1993.

(28) Mulder, I. Determination of Acetyl Coenzyme A. Interference by a Contaminant in Malate Dehydrogenase. *Journal of Lipid Research* **1972**, *13* (4), 552–554. https://doi.org/10.1016/S0022-2275(20)39389-5.

(29) Wiley, S.; Griffith, C.; Eckert, P.; Mueller, A. P.; Nogle, R.; Simpson, S. D.; Köpke, M.; Can, M.; Sarangi, R.; Kubarych, K.; Ragsdale, S. W. An Alcove at the Acetyl-CoA Synthase Nickel Active Site Is Required for Productive Substrate CO Binding and Anaerobic Carbon Fixation. *Journal of Biological Chemistry* **2024**, *300* (8), 107503. https://doi.org/10.1016/j.jbc.2024.107503.

(30) Silva, P. J.; van den Ban, E. C. D.; Wassink, H.; Haaker, H.; de Castro, B.; Robb, F. T.; Hagen, W. R. Enzymes of Hydrogen Metabolism in Pyrococcus Furiosus. *European Journal of Biochemistry* **2000**, *267* (22), 6541–6551. https://doi.org/10.1046/j.1432-1327.2000.01745.x.

(31) Mitra, D.; George, S. J.; Guo, Y.; Kamali, S.; Keable, S.; Peters, J. W.; Pelmenschikov, V.; Case, D. A.; Cramer, S. P. Characterization of [4Fe-4S] Cluster Vibrations and Structure in Nitrogenase Fe Protein at Three Oxidation Levels via Combined NRVS, EXAFS, and DFT Analyses. *J. Am. Chem. Soc.* **2013**, *135* (7), 2530–2543. https://doi.org/10.1021/ja307027n.

(32) Grunwald, L.; Abbott, D. F.; Mougel, V. Gauging Iron–Sulfur Cubane Reactivity from Covalency: Trends with Oxidation State. *JACS Au* **2024**, *4* (4), 1315–1322. https://doi.org/10.1021/jacsau.4c00213.

(33) Silver, S. C.; Gardenghi, D. J.; Naik, S. G.; Shepard, E. M.; Huynh, B. H.; Szilagyi, R. K.; Broderick, J. B. Combined Mössbauer, Multi-Edge X-Ray Absorption Spectroscopic, and

Density Functional Theoretical Study of the Radical SAM Enzyme Spore Photoproduct Lyase. *J Biol Inorg Chem* **2014**, *19* (3), 465–483. https://doi.org/10.1007/s00775-014-1104-y.

(34) Scott, R. A.; Kazmi, S. A.; Beinert, H.; Emptage, M. H.; Hahn, J. E.; Hodgson, K. O.; Stout, C. D.; Thompson, A. J. X-Ray Absorption Spectroscopy of 3-Fe Clusters in Fe□S Proteins. *Inorganica Chimica Acta* **1983**, *79*, 142. https://doi.org/10.1016/S0020-1693(00)95178-8.

(35) Peggy A. O'day; Nelson Rivera Jr.; Robert Root; Susan A. Carroll. X-Ray Absorption Spectroscopic Study of Fe Reference Compounds for the Analysis of Natural Sediments. *American Mineralogist* **2004**, *89*, 572–585. https://doi.org/10.2138/am-2004-0412.

(36) Jinqiang Xia; Zhengguo Hu; Codrina V. Popescu; Paul A. Lindahl; Eckard Münck. Mössbauer and EPR Study of the Ni-Activated α-Subunit of Carbon Monoxide Dehydrogenase from Clostridium Thermoaceticum. *ACS Publications* **1997**, *119*, 8301–8312. https://doi.org/10.1021/ja971025+.

(37) James, C. D.; Wiley, S.; Ragsdale, S. W.; Hoffrnan, B. M. 13C Electron Nuclear Double Resonance Spectroscopy Shows Acetyl-CoA Synthase Binds Two Substrate CO in Multiple Binding Modes and Reveals the Importance of a CO-Binding "Alcove." *J Am Chem Soc* **2020**, *142* (36), 15362–15370. https://doi.org/10.1021/jacs.0c05950.

(38) Gorst, C. M.; Ragsdale, S. W. Characterization of the NiFeCO Complex of Carbon Monoxide Dehydrogenase as a Catalytically Competent Intermediate in the Pathway of Acetyl-Coenzyme A Synthesis. *Journal of Biological Chemistry* **1991**, *266* (31), 20687–20693. https://doi.org/10.1016/S0021-9258(18)54763-3.

(39) Lindahl, P. A.; Münck, E.; Ragsdale, S. W. CO Dehydrogenase from Clostridium Thermoaceticum. EPR and Electrochemical Studies in CO2 and Argon Atmospheres. *Journal of Biological Chemistry* **1990**, *265* (7), 3873–3879. https://doi.org/10.1016/S0021-9258(19)39675-9.

(40) Lu, W. P.; Harder, S. R.; Ragsdale, S. W. Controlled Potential Enzymology of Methyl Transfer Reactions Involved in Acetyl-CoA Synthesis by CO Dehydrogenase and the Corrinoid/Iron-Sulfur Protein from Clostridium Thermoaceticum. *Journal of Biological Chemistry* **1990**, *265* (6), 3124–3133. https://doi.org/10.1016/S0021-9258(19)39743-1.

(41) Bhaskar, B.; DeMoll, E.; Grahame, D. A. Redox-Dependent Acetyl Transfer Partial Reaction of the Acetyl-CoA Decarbonylase/Synthase Complex: Kinetics and Mechanism. *Biochemistry* **1998**, *37* (41), 14491–14499. https://doi.org/10.1021/bi9812423.

(42) Desmarais, J. K.; Bi, W.; Zhao, J.; Hu, M. Y.; Alp, E.; Tse, J. S. 57Fe Mössbauer Isomer Shift of Pure Iron and Iron Oxides at High Pressure—An Experimental and Theoretical Study. *J. Chem. Phys.* **2021**, *154* (21), 214104. https://doi.org/10.1063/5.0048141.

(43) Herber, R. H.; King, R. B.; Wertheim, G. K. Systematics of Mössbauer Isomer Shifts of Iron-Organic Compounds. *Inorg. Chem.* **1964**, *3* (1), 101–107. https://doi.org/10.1021/ic50011a021.

(44) Mullinger, R. N.; Cammack, R.; Rao, K. K. Physicochemical Characterization of the Four-Iron-Four-Sulphide Ferredoxin from Bacillus Stearothermophilus. **1975**, *151*.

(45) Middleton, P.; Dickson, D. P. E.; Johnson, C. E.; Rush, J. D. Interpretation of the Mössbauer Spectra of the Four-Iron Ferredoxin from Bacillus Stearothermophilus. *European Journal of Biochemistry* **1978**, *88* (1), 135–141. https://doi.org/10.1111/j.1432-1033.1978.tb12430.x.

(46) Prakash, D.; Xiong, J.; Chauhan, S. S.; Walters, K. A.; Kruse, H.; Yennawar, N.; Golbeck, J. H.; Guo, Y.; Ferry, J. G. The Catalytic Activity of the Archetype from Group 4 of the FTR-like Ferredoxin:Thioredoxin Reductase Family Is Regulated by Unique S=7/2 and S=1/2 [4Fe-4S] Clusters. *Biochemistry* **2024**, *63* (12), 1588–1598. https://doi.org/10.1021/acs.biochem.3c00651.

(47) Prakash, D.; Walters, K. A.; Martinie, R. J.; McCarver, A. C.; Kumar, A. K.; Lessner, D. J.; Krebs, C.; Golbeck, J. H.; Ferry, J. G. Toward a Mechanistic and Physiological Understanding of a Ferredoxin:Disulfide Reductase from the Domains Archaea and Bacteria. *J Biol Chem* **2018**, *293* (24), 9198–9209. https://doi.org/10.1074/jbc.RA118.002473.

Chapter 5 Conclusions

Small mutations to secondary sphere residues can have a huge impact on enzyme function. In acetyl-CoA synthase, mutation of phenylalanine-229, one of five hydrophobic residues forming an alcove around the catalytically active nickel site, imparts a huge degree of tunability to the enzyme's affinity for CO. Mutation to tryptophan (F229W) increased the binding affinity by about 80 fold; but this same residue mutated to alanine (F229A) caused a 30 fold decrease in binding affinity[1]. The CO binding step is not only rate limiting for the enzyme but for the Wood-Ljungdahl Pathway as a whole[2]. This single residue imparts a significant level of tunability for enzyme activity and therefore the entire pathway, raising questions about how the other alcove residues tune substrate binding and catalysis. The two phenylalanine residues (229, 512) are highly conserved in bacterial species but there is variability in the isoleucine-145 and valine 149. There are also residues in the CO tunnel that appear to gate CO movements before it reaches the alcove[3,4]. Mutation studies on tunnel residues has great potential to improve our understanding of the tunnel's role in CO regulation and how conformational changes can regulate enzymes.

X-ray absorbance spectroscopy continues to be a powerful technique for characterizing the nickel intermediates of ACS providing key information about oxidation state, geometry, and bond distances in a variety of states. After 30 years, XAS was the key to proving the hypothesis that all of the intermediates are nickel-bound making ACS a highly unusual protein in the world of biochemistry. In our studies, both methyl- and acetyl-A-cluster formed highly delocalized square planar nickel(II) complexes pulling positive charge away from the Ni_p and poising the methyl intermediate for carbonyl insertion. The results of this study bridge the gap between a strictly paramagnetic or diamagnetic mechanism, suggesting instead the EC mechanism which includes intermediates from both mechanisms. Further studies should reveal how the fine tuning of structure and dynamics of ACS and its active site promote the ACS mechanism.

Our further studies on the post-thiolysis A* intermediate find that it is not a nickel(0), Ni^{1+}-$[Fe_4S_4]^{1+}$ intermediate as described in the methanogenic system[5]. Our results determined

that it was one electron reduced relative to the A_{ox} resting state and yet it is also Ni^{2+}-$[Fe_4S_4]^{2+}$ and capable of binding CO or methyl. This presents a conundrum of how the enzyme can be one electron reduced while we know that the A_{ox} state must be reductively activated to bind substrates. There were small geometric and structural differences between A* and A_{ox} which further investigation of is needed and will likely resolve this question.

New advances in cryoEM and other structural techniques have led towards many new structures in recent years increasing our knowledge of the interplay between structure and function and improving our understanding of the conformation changes that are critical to the catalytic cycle of ACS. But our current structural knowledge still lacks enough variety and resolution in CODH/ACS structures to fully understand the variability and details of the open states. ACS can adopt and which of these are catalytically relevant as well as structural differences between bacterial systems let alone methanogenic ones. When the *Clostridium autoethanogenum* structure was published in 2021, it was the first time ACS had been observed to bind to a single face of one CODH monomer rather than the CODH dimer interface long known for the *Moorella thermoacetica* structure[6–8]. Another more recent structure of the same complex also captured the binding pocked for CoA and shows the CoA thiol in close proximity to the Ni_p, an exciting new discovery but invites more questions about CoA interaction with ACS. Does the CoA thiol directly interact with the nickel during thiolysis? Is CoA inhibition caused by CoA occupying a site on the proximal nickel preventing CO or Methyl from binding? Dobbeck's recent *Carboxydothermus hydrogenoformans* structures mark only the third bacterial species of a full CODH/ACS complex to be solved. They matched the canonical *Moorella* structures well but proposed a never-before-characterized tetrahedral bound acetyl intermediate, rather than the square planar geometry clearly observed previously by XAS [4,9,10]. Whether this intermediate is unique to the C*arboxydothermus* complex or catalytically relevant is an intriguing direction for future work. More work is needed to bring us closer to a unified model of the ACS mechanism. A combination of high resolution crystallography and high resolution spectroscopy techniques like XAS have massively improved our understanding of this unusual protein in the last decade and new advances in technology and analysis methods will continue to contribute to our collective knowledge.

Despite 30+ years of literature on CODH/ACS and the Wood-Ljungdahl pathway, there are still many unanswered questions. What is the catalytically relevant reductively activated

species for ACS? Our XAS studies on A* suggest that it is one electron reduced compared to A_{ox} and is capable of binding methyl and CO and reforming A-acetyl but more work is needed to define A*. Are there nickel(III) species in the mechanism? The EC mechanism bridges the gap between the diamagnetic and paramagnetic hypotheses but does still require the transient formation of methyl- and acetyl-nickel(III) intermediates. How do the other alcove residues tune substrate binding and catalysis? What drives the conformational changes in ACS? Are these triggered by substrate binding? Protein-protein interactions?

CODH/ACS and the Wood-Ljungdahl pathway provide a highly energy efficient method for carbon capture and the acetogens containing them are already in use in industry to produce ethanol from carbon emissions[11]. Understanding how these enzymes function to fix carbon dioxide in an energy-efficient manner can inform the development of new industrial catalysts to accomplish this difficult chemistry. It also improves our knowledge of the methods bioinorganic proteins use for promotion of difficult chemistry through conformational control and effectual control of electron localization.

5.1 References

(1) Wiley, S.; Griffith, C.; Eckert, P.; Mueller, A. P.; Nogle, R.; Simpson, S. D.; Köpke, M.; Can, M.; Sarangi, R.; Kubarych, K.; Ragsdale, S. W. An Alcove at the Acetyl-CoA Synthase Nickel Active Site Is Required for Productive Substrate CO Binding and Anaerobic Carbon Fixation. *J. Biol. Chem.* **2024**, *300* (8), 107503. https://doi.org/10.1016/j.jbc.2024.107503.

(2) Seravalli, J.; Kumar, M.; Ragsdale, S. W. Rapid Kinetic Studies of Acetyl-CoA Synthesis: Evidence Supporting the Catalytic Intermediacy of a Paramagnetic NiFeC Species in the Autotrophic Wood−Ljungdahl Pathway. *Biochemistry* **2002**, *41* (6), 1807–1819. https://doi.org/10.1021/bi011687i.

(3) Biester, A.; Grahame, D. A.; Drennan, C. L. Capturing a Methanogenic Carbon Monoxide Dehydrogenase/Acetyl-CoA Synthase Complex via Cryogenic Electron Microscopy. *Proc. Natl. Acad. Sci.* **2024**, *121* (41), e2410995121. https://doi.org/10.1073/pnas.2410995121.

(4) Ruickoldt, J.; Kreibich, J.; Bick, T.; Jeoung, J.-H.; Duffus, B. R.; Leimkühler, S.; Dobbek, H.; Wendler, P. Ligand Binding to a Ni–Fe Cluster Orchestrates Conformational Changes of the CO-Dehydrogenase–Acetyl-CoA Synthase Complex. *Nat. Catal.* **2025**, *8* (7), 657–667. https://doi.org/10.1038/s41929-025-01365-y.

(5) Gencic, S.; Duin, E. C.; Grahame, D. A. The Two-Electron Reduced A Cluster in Acetyl-CoA Synthase: Preparation, Characteristics and Mechanistic Implications. *J. Inorg. Biochem.* **2023**, *240*, 112098. https://doi.org/10.1016/j.jinorgbio.2022.112098.

(6) Lemaire, O. N.; Wagner, T. Gas Channel Rerouting in a Primordial Enzyme: Structural Insights of the Carbon-Monoxide Dehydrogenase/Acetyl-CoA Synthase Complex from the Acetogen Clostridium Autoethanogenum. *Biochim. Biophys. Acta BBA - Bioenerg.* **2021**, *1862* (1), 148330. https://doi.org/10.1016/j.bbabio.2020.148330.

(7) Cohen, S. E.; Brignole, E. J.; Wittenborn, E. C.; Can, M.; Thompson, S.; Ragsdale, S. W.; Drennan, C. L. Negative-Stain Electron Microscopy Reveals Dramatic Structural Rearrangements in Ni-Fe-S-Dependent Carbon Monoxide Dehydrogenase/Acetyl-CoA Synthase. *Struct. Lond. Engl. 1993* **2021**, *29* (1), 43-49.e3. https://doi.org/10.1016/j.str.2020.08.011.

(8) Darnault, C.; Volbeda, A.; Kim, E. J.; Legrand, P.; Vernède, X.; Lindahl, P. A.; Fontecilla-Camps, J. C. Ni-Zn-[Fe4-S4] and Ni-Ni-[Fe4-S4] Clusters in Closed and Open α Subunits of Acetyl-CoA Synthase/Carbon Monoxide Dehydrogenase. *Nat. Struct. Mol. Biol.* **2003**, *10* (4), 271–279. https://doi.org/10.1038/nsb912.

(9) Can, M.; Abernathy, M. J.; Wiley, S.; Griffith, C.; James, C. D.; Xiong, J.; Guo, Y.; Hoffman, B. M.; Ragsdale, S. W.; Sarangi, R. Characterization of Methyl- and Acetyl-Ni Intermediates in Acetyl CoA Synthase Formed during Anaerobic CO_2 and CO Fixation. *J. Am. Chem. Soc.* **2023**, *145* (25), 13696–13708. https://doi.org/10.1021/jacs.3c01772.

(10) Ruickoldt, J.; Basak, Y.; Domnik, L.; Jeoung, J.-H.; Dobbek, H. On the Kinetics of CO_2 Reduction by Ni, Fe-CO Dehydrogenases. *ACS Catal.* **2022**, *12* (20), 13131–13142. https://doi.org/10.1021/acscatal.2c02221.

(11) Pettinato, E.; Hocq, R.; Pflügl, S. Utilization of the Liquid One Carbon Feedstocks Methanol and Formate for Acetogenic Bioproduction of Chemicals and Fuels. *Bioresour. Technol.* **2025**, *432*, 132643. https://doi.org/10.1016/j.biortech.2025.132643.